

ELECTROMAGNETICS LABORATORY
TECHNICAL REPORT 94-4

October 1993

INTEGRATED REFLECTOR ANTENNA DESIGN AND ANALYSIS

FINAL REPORT

M. L. Zimmerman, S. W. Lee, S. Ni, M. Christensen and Y. M. Wang

University of Illinois, Urbana-Champaign



Supported by

NASA Lewis Research Center
Cleveland, Ohio

NCC3-156

Electromagnetics Laboratory
Department of Electrical and Computer Engineering
University of Illinois at Urbana-Champaign
Urbana, Illinois 61801

N94-24678

Unclass

G3/32 0206784

(NASA-CR-195164) INTEGRATED
REFLECTOR ANTENNA DESIGN AND
ANALYSIS Final Report (Illinois
Univ.) 188 p

INTEGRATED REFLECTOR ANTENNA DESIGN AND ANALYSIS

M. L. Zimmerman, S. W. Lee, S. Ni, M. Christensen and Y. M. Wang

University of Illinois, Urbana-Champaign

Final Report

NASA NCC3-156

October 1993

Electromagnetics Laboratory
Department of Electrical and Computer Engineering
University of Illinois at Urbana-Champaign
Urbana, IL 61801

ABSTRACT

Reflector antenna design is a mature field and most aspects have been studied. However, of that most previous work is distinguished by the fact that it is narrow in scope, analyzing only a particular problem under certain conditions. Methods of analysis of this type are not useful for working on real-life problems since they can not handle the many and various types of perturbations of basic antenna design. In this thesis, the idea of an integrated design and analysis is proposed. By broadening the scope of the analysis, it becomes possible to deal with the intricacies attendant with modern reflector antenna design problems.

In this thesis, the concept of integrated reflector antenna design is put forward. A number of electromagnetic problems related to reflector antenna design are investigated. Some of these show how tools for reflector antenna design are created. In particular, a method for estimating spillover loss for open-ended waveguide feeds is examined. The problem of calculating and optimizing beam efficiency (an important figure of merit in radiometry applications) is also solved. Other chapters in this thesis deal with applications of this general analysis. The wide-angle scan abilities of reflector antennas is examined and a design is proposed for the ATDRSS triband reflector antenna. The following chapter discusses the development of a general phased-array pattern computation program and shows how the concept of integrated design can be extended to other types of antennas. The conclusions are contained in the final chapter.

ACKNOWLEDGEMENTS

Thanks go to R. Acosta, G. Fujikawa, R. Q. Lee, and R. Sharp of the NASA Lewis Research Center, Cleveland, Ohio. This work was supported under NASA 3-419 and NASA NCC3-156 for the period from June, 1988 to August, 1991.

TABLE OF CONTENTS

	Page
1. INTRODUCTION	1
2. RELECTOR SPILLOVER LOSS OF AN OPEN-ENDED RECTANGULAR AND CIRCULAR WAVEGUIDE FEED	3
3. REFLECTOR ANTENNA ANALYSIS	14
3.1. Description of Problem	14
3.2. The Reflector Surface	15
3.2.1. Parabolic reflector	15
3.2.2. Spherical reflector	16
3.2.3. Hyperbolic reflector	16
3.2.4. Conic section	16
3.2.5. Boundary	16
3.3. The Source	17
3.3.1. Feed source	17
3.3.2. Power radiated	20
3.3.3. Incident field on reflector	20
3.4. Geometrical Optics Field	21
3.4.1. Reflection point	21
3.4.2. Formula for reflected field	22
3.4.3. Curvatures of reflected wavefront	23
3.5. The Edge-Diffracted Field	26
3.5.1. Diffraction points	26
3.5.2. Formula for diffracted field	27
3.5.3. Divergence factor	27
3.5.4. Diffraction coefficients	28
3.5.5. Spherical components of incident field	30
3.5.6. Rectangular components of diffracted field	30
3.5.7. Detour parameter	31
3.5.8. Uniform asymptotic theory	31
3.6. Secondary Pattern Computation	32
3.6.1. Fast Fourier transform	33
3.6.2. Polarization of secondary pattern	33
3.6.3. Directivity	34
3.7. Concluding Remarks	35
4. WIDE-ANGLE SCANNING FOR REFLECTOR ANTENNAS	43
4.1. Single Reflector Antennas	44
4.1.1. P1: symmetric parabolic reflector with $f/D=2$	44
4.1.2. P2: symmetric parabolic reflector with $f/D=1$	46
4.1.3. P3: offset parabolic reflector	49
4.2. Dual Reflector Antennas	50
4.2.1. C1: cassegrainian reflector with tilted main reflector	50
4.2.2. C2: cassegrainian reflector with tilted subreflector	51
4.2.3. C3: cassegrainian reflector with both reflectors tilted	51

4.3.	Conclusions	52
5.	COMPUTATION AND OPTIMIZATION OF BEAM EFFICIENCY	67
5.1.	Three Definitions	67
5.2.	The Problem with Direct Computation	69
5.3.	Indirect Computation of Beam Efficiency	71
5.4.	Optimization of Beam Efficiency for Cluster Feeds	73
5.4.1.	Use of cluster feeds	73
5.4.2.	Matrix formulation	74
5.4.3.	Optimization of beam efficiency	75
5.5.	Results and Discussion	77
5.5.1.	Power as a function of sidelobes	77
5.5.2.	Efficiency of reflector antennas	77
5.5.3.	Dependence of beam efficiency on feed size	77
5.5.4.	Scanned beam	78
5.5.5.	Cluster feed	79
6.	USE OF FREQUENCY SELECTIVE SURFACES IN REFLECTOR ANTENNA DESIGN	99
6.1.	The ATDRSS Project	99
6.2.	Design	100
6.2.1.	FSS design	101
6.2.2.	Offset reflector	102
6.2.3.	Symmetric reflector	103
6.2.4.	Comparison of reflector size	103
6.3.	Results	104
6.4.	Physical Layout	107
7.	CONCLUSIONS	119
	REFERENCES	120
	APPENDIX	123

1. INTRODUCTION

The subject of this thesis is based on the analysis and design of reflector antennas using an integrated approach. The concept is to obtain a method of analysis that can be applied to a wide variety of problems, rather than one that is narrow in scope and may be applied to only a few specific problem types. Reflector antenna design is a mature field. Reflector antennas have been in common use since World War II. They are still popular today due to their simplicity, ease of construction, low cost, and light weight. Most aspects of reflector antenna design have been studied in the past. Figures of merit such as directivity, beam efficiency, and sidelobe level have been looked at closely. The effect of feeds, compensation for reflector distortion, shaping of the reflector dish, etc. have also been studied. What most of these earlier studies lacked, however, was a broad scope. A particular aspect of reflector antenna design was studied. A method of analysis was derived and results were obtained. Then another problem would be tackled, with its own solution. However the method of analysis could rarely be used for anything other than generating research papers on that particular topic.

The intention of this thesis is to make the jump from methods of analysis that generate research papers to methods of analysis that can be used to tackle a broad range of real life design problems. This means that the analysis must be able to handle a broad range of reflector antenna intricacies. The method of analysis must be very general in nature and yet be simple enough so that it may be used by someone other than the originator of the method of analysis.

In each chapter a separate topic of reflector antennas is discussed. The chapters are related by the fact that they represent some of the problems encountered with reflector design. The second chapter discusses an important parameter for reflector antenna design, the spillover loss. In the third chapter, the aperture integration method, which is used in our reflector antenna analyses, is explained in detail. The fifth chapter examines the analysis of beam efficiency, the most important figure of merit for antennas used in

radiometry applications. The fourth and sixth chapters look at problems posed for reflector antennas. In the fourth chapter, a study is undertaken to find the limits to which a reflector antenna system might be used for scanning. In the sixth chapter the challenge of constructing a triband reflector antenna is examined. In this chapter, in particular, all the capabilities of the method of analysis must be brought to bear on the problem, since there are many constraints upon the design. It is this type of reflector antenna problem, involving a space-borne antenna, that will be the focus of much of the future research in reflector antennas. Conclusions are presented in the final chapter.

2. REFLECTOR SPILLOVER LOSS OF AN OPEN-ENDED RECTANGULAR AND CIRCULAR WAVEGUIDE FEED

Open-ended rectangular and circular waveguides are a most commonly used feed for reflector antennas¹. Their radiation pattern was first calculated by Chu in 1940 by using a form of Kirchhoff's approximation [1,2]. Important pattern characteristics such as 3 dB beamwidth, zeros, and sidelobes are well documented in the literature [3,4]. In reflector applications, there is another important parameter, namely, the spillover loss, which is defined as the fraction of power received by the symmetrical reflector within the half-cone angle θ (Figure 2.1). (All figures will appear at the end of their respective chapters.) In this note, we shall present a set of curves giving spillover loss for several practical cases. For one feed case, we will also present a simple analytic expression which gives a good approximation to the spillover loss and is obtained by curve fitting.

In spillover or directivity calculations, one must first determine the power radiated by the feed from the Poynting integral over a closed surface S , i.e.,

$$P = \iint_S (\mathbf{E} \times \mathbf{H}^*) \cdot d\mathbf{s} \quad (2.1)$$

If (\mathbf{E}, \mathbf{H}) were known exactly, the result of P would be unique no matter which surface S is used. In the Chu-Kirchhoff formulation [2, Eq. 11], the aperture field at the waveguide opening S_1 is approximated by the incident mode (e.g., TE_{11}). The higher-order modes and reflected field are ignored. This is justified in the literature for circular waveguides with $a > 1 \lambda$ [2] and for rectangular waveguides [5]. Because of this approximation, the two power computations

$P_1 = P$ calculated from (2.1) by using surface S_1 , and

$P_\infty = P$ calculated from (2.1) by using the infinite radiation surface S_∞

are generally different. In fact

¹ Some of these results have been published in IEEE Transactions on Antennas and Propagation, June, 1990 [24].

$$P_1 > P_{\infty} \quad (2.2)$$

because P_1 contains both P_{∞} and the reflected power. In the limit $a/\lambda \rightarrow \infty$, P_1 reduces to P_{∞} as expected. In Figure 2.2, we plot P_{∞}/P_1 as a function of a/λ for different waveguide feeds. In spillover calculations, we use P_{∞} instead of P_1 as the input power so that the spillover loss goes to zero as $\theta \rightarrow \pi$.³

It should be noted that for field patterns the theoretical and experimental results diverge as the size of the aperture decreases. Agreement is good for waveguides as large as those for which results are shown in Figures 2.3 to 2.7 [2], [5]. However, the results should not be extended to cover waveguides smaller than those for which results are shown.

Spillover results are presented in Figures 2.3 to 2.7 in the following manner.

Table 2.1. Modes used in waveguides

Fig.	waveguide	mode
2.3	circular	TE ₁₁
2.4	circular	TE ₂₁
2.5	2:1 rectangular	sum
2.6	square	sum
2.7	4 square	difference

As an example, consider a circular waveguide for a monopulse feed, using the TE₁₁ mode and TE₂₁ mode for sum and difference patterns. Let the reflector be of the symmetric parabolic type with $f/D=0.4$. The extended half-cone angle of the reflector is 64°. In order

³ Reflector directivity calculations were sometimes carried out by using P_1 (not P_{∞}) as the feed input power. Strictly speaking this practice underestimates the directivity of the reflector antenna. For example, for a circular guide feed with $a=0.7\lambda$ and excited by TE₂₁, P_{∞}/P_1 read from Fig. 1 is 0.91, corresponding to a directivity underestimate of 0.4 dB.

to keep the spillover loss less than 1 dB, the diameter of the circular guide should be at least 0.90λ . This size waveguide feed would have less than 1 dB spillover loss for both the TE_{11} and TE_{21} modes.

For the case of a circular waveguide excited by the TE_{11} mode, an analytic expression has been derived by curve fitting. This expression is fairly accurate over the range where $20^\circ < \theta < 70^\circ$ and spillover loss is less than 4 dB. It reads

$$\text{spillover loss (in dB)} = -\alpha\theta^{-\beta}$$

$$\text{where} \quad \log_{10}\alpha = 3.78(a/\lambda)^{-0.629} \quad (2.3)$$

$$\beta = 2.50(a/\lambda)^{-0.324} .$$

Here θ is the half-cone angle in degrees and a is the parameter defining the feed size. A comparison of the results obtained from the computer code and from the formula in (2.3) is shown in Figure 2.8 for several sizes of waveguides.

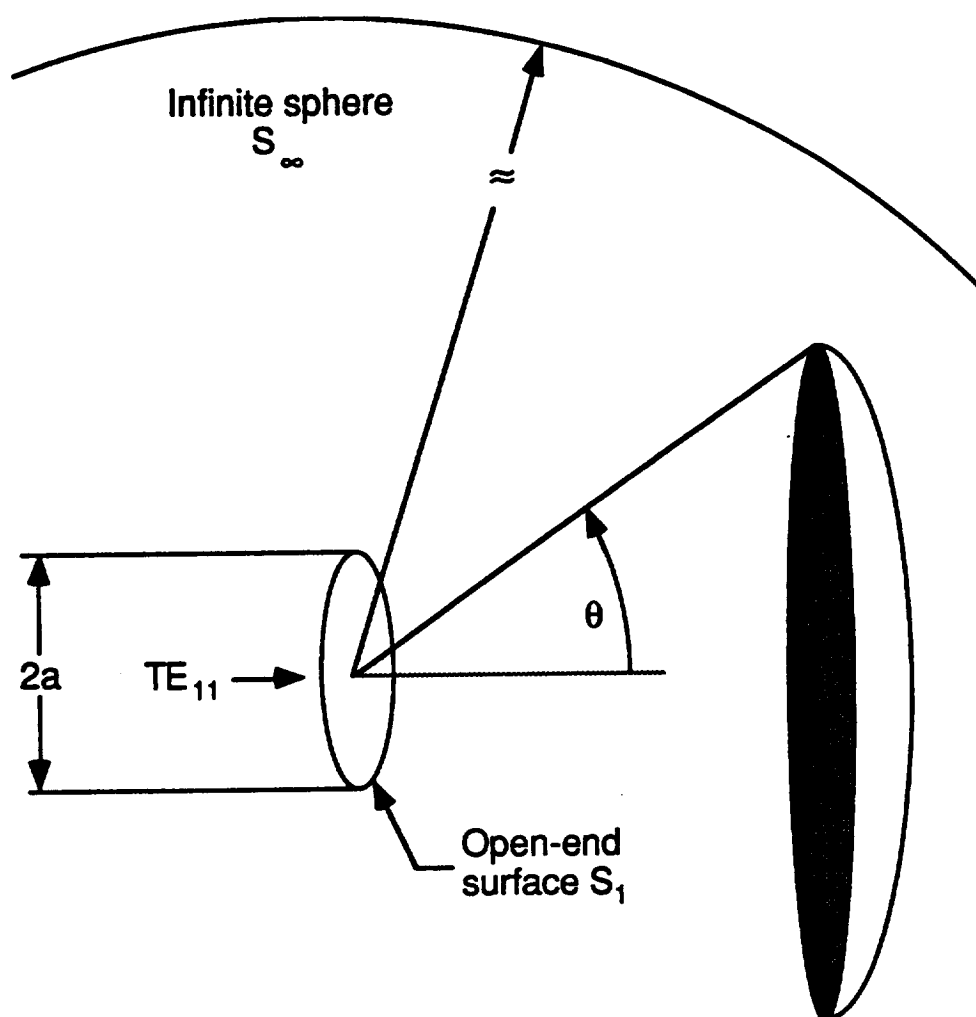


Figure 2.1. The total input power radiated from the feed may be determined by an integration over surface S_∞ or over surface S_1 .

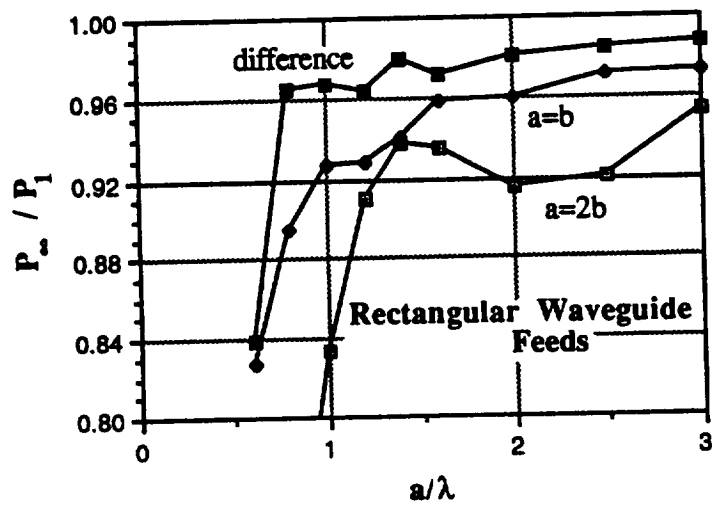
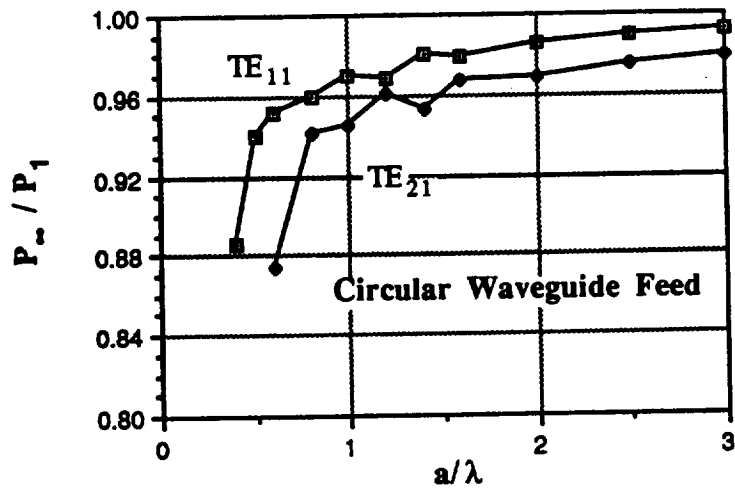


Figure 2.2. Relationship between the power at infinity P_{∞} and the power radiated through the end of the waveguide P_1 for excitations of a circular feed and rectangular feeds.

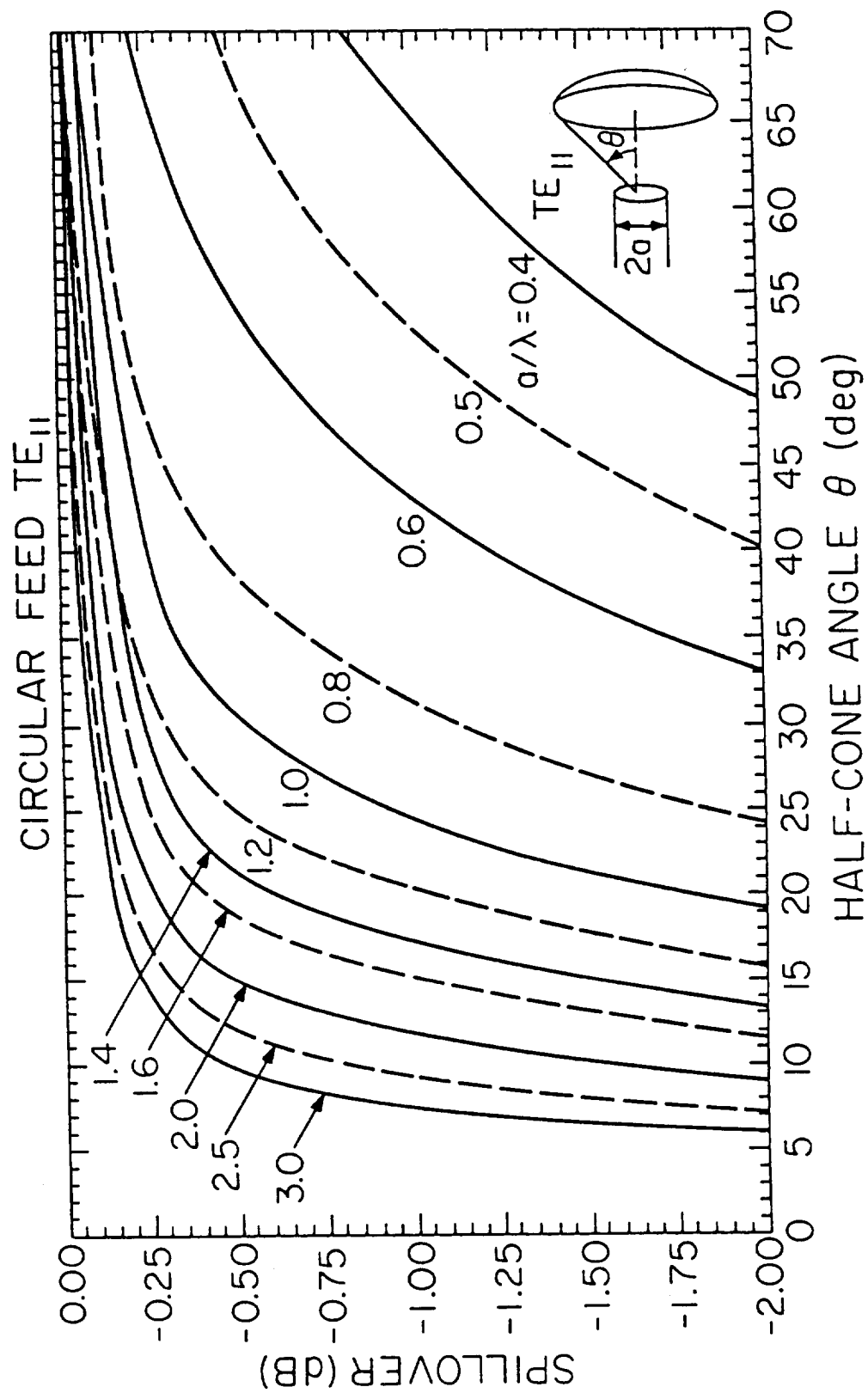


Figure 2.3. Spillover loss for a circular waveguide excited by the TE_{11} mode.

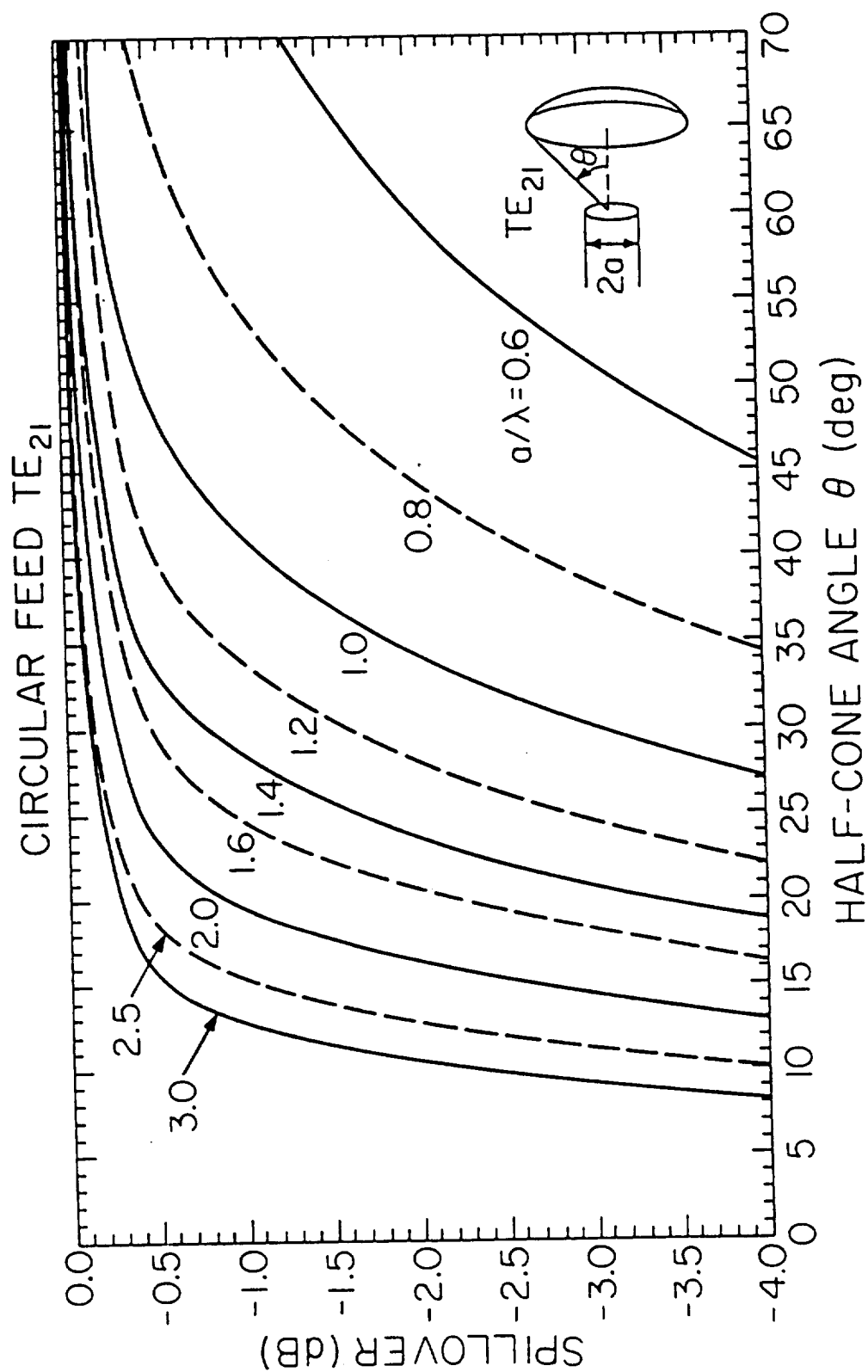


Figure 2.4. Spillover loss for a circular waveguide excited by the TE₂₁ mode.

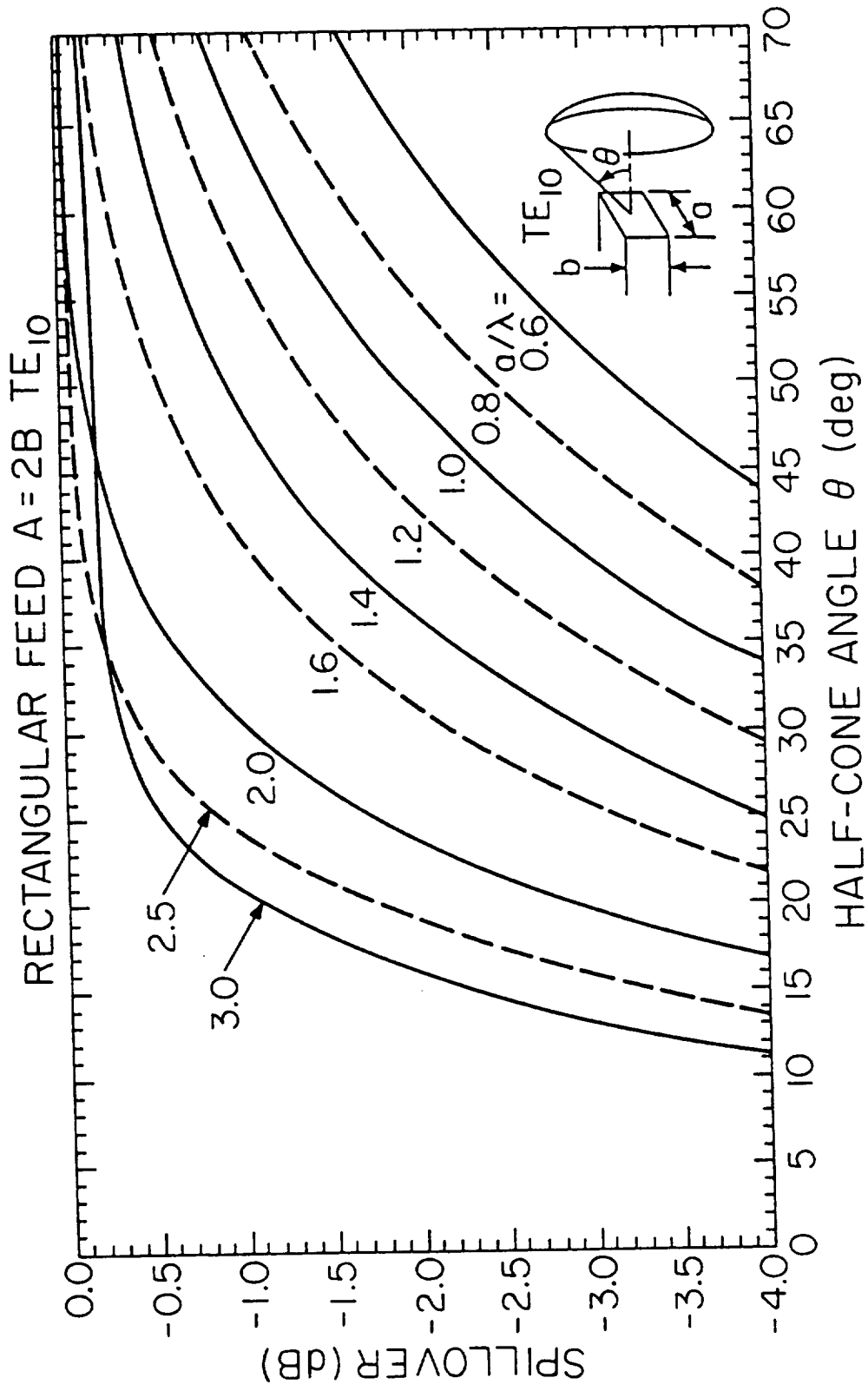


Figure 2.5. Spillover loss for a rectangular waveguide excited by the TE_{10} mode.

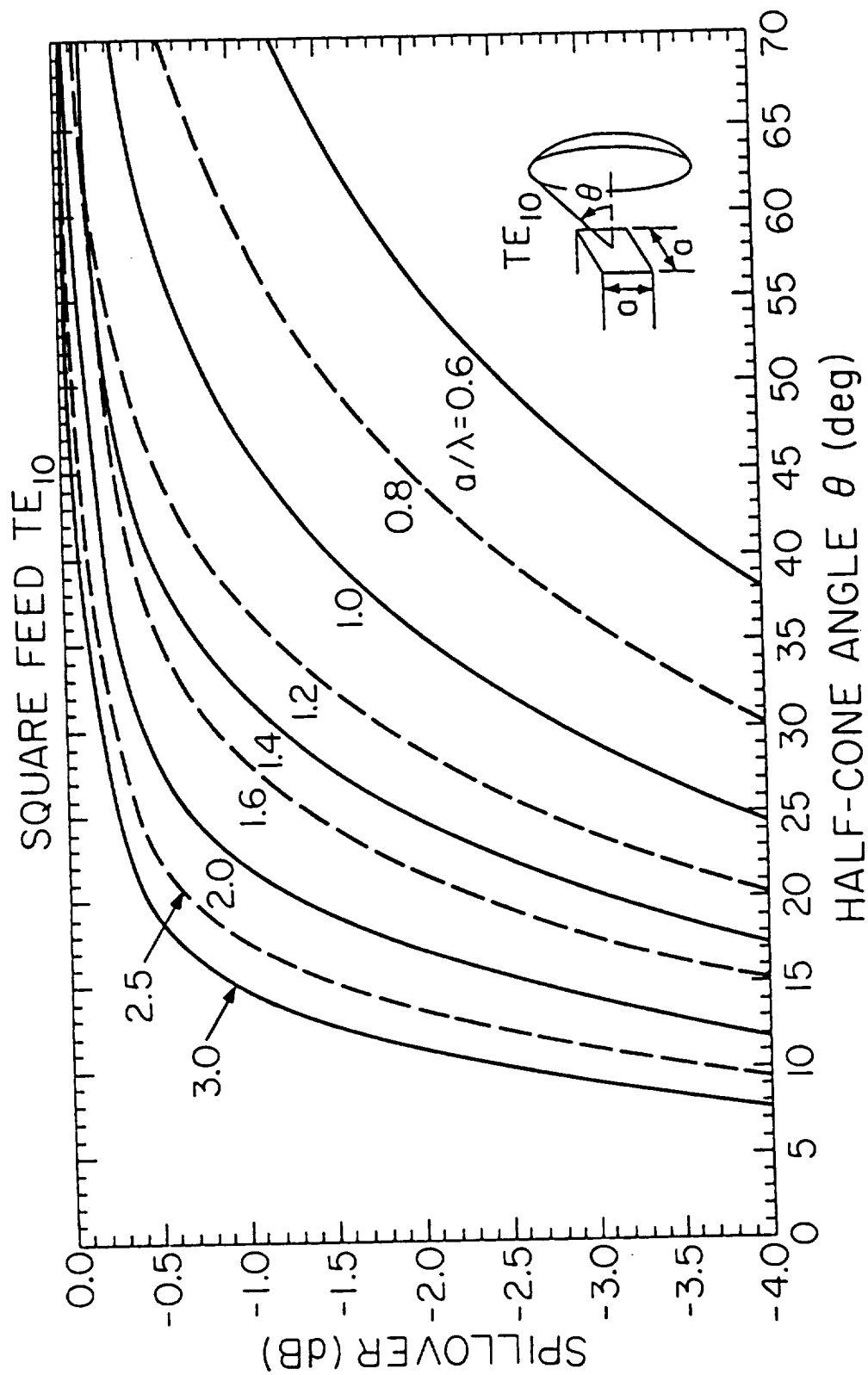


Figure 2.6. Spillover loss for a square waveguide excited by the TE_{10} mode.

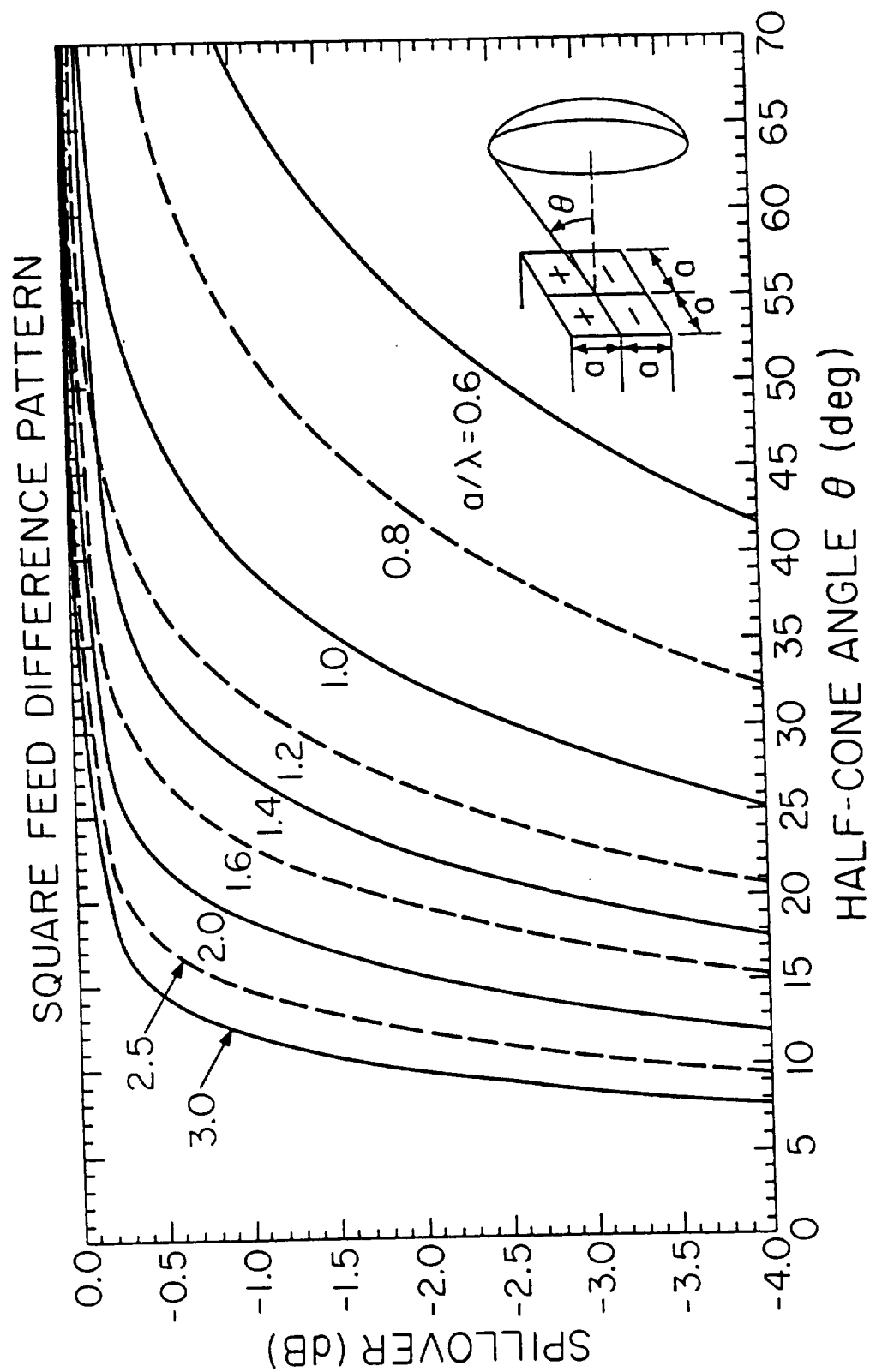


Figure 2.7. Spillover loss for a square difference waveguide.

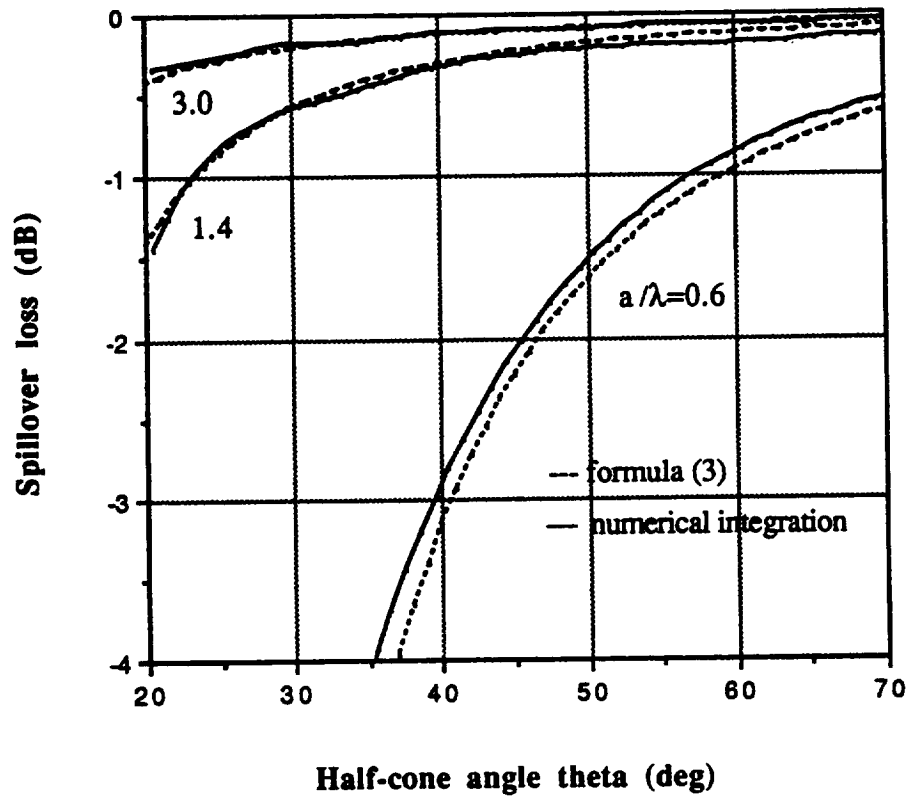


Figure 2.8. Comparison of spillover calculated by numerical integration and that by the simple formula in (2.3) for the circular waveguide excited by the TE_{11} mode.

3. REFLECTOR ANTENNA ANALYSIS

In this chapter the method of solution for reflector antenna problems will be discussed. After describing the problem and the various elements involved, the individual elements will be discussed one-by-one. This derivation is not original, having appeared in other sources [6], but it is useful for understanding the methods used in our reflector antenna calculations.

3.1. Description of Problem

The geometry of the problem under consideration is shown in Figure 3.1. A reflector S is illuminated by the incident field from an array feed. The method of solution used is Aperture Integration (AI), which provides the same degree of accuracy as Physical Optics (PO) and avoids the caustics (infinite field in the main beam direction) that occur in the Geometric Theory of Diffraction (GTD). In PO, the induced surface currents on the reflector S are approximated by

$$\mathbf{J}_s = 2\mathbf{n} \times \mathbf{H}^i. \quad (3.1)$$

These currents are then integrated to find the far field $\mathbf{E}^s(\mathbf{r})$. In AI the reflected-field and diffracted-field contributions at a point P_2 on the planar aperture surface S_a are computed. This is done for points forming a grid over the aperture surface. A Fast Fourier Transform (FFT) is then used to obtain the far-field $\mathbf{E}^s(\mathbf{r})$ [6-9]. AI has several advantages over PO. First of all, the use of an FFT (allowed by integration over the planar surface S_a) is numerically efficient. The present formulation also allows for the use of multiple reflectors. In addition, AI can be used to obtain near-field information. Many of today's experimental measurements for reflector antennas are conducted in near-field ranges so this method can be used as an analytical check. Other advantages of the formulation of AI presented here are

- (i) The surface of the reflector may be arbitrary.

- (ii) The edge of the reflector can be an arbitrary curve lying on an elliptical cone or cylinder.
- (iii) The divergence factor of the Geometric Optics (GO) field is correctly computed. This allows the feed to be placed away from the reflector dish where the divergence factor is not unity.
- (iv) The edge diffracted field is included here. Two uniform theories are used to keep the aperture field continuous from the lit to the shadow region.

In Sections 3.2 to 3.6 the elements of the reflector problem will be examined. In the next section the source will be studied. This leads to the incident field H^i on the reflector. In Section 3.3 the method of describing the reflector(s) is put forth. This is necessary for obtaining the field at some point on the aperture surface. Finally an FFT is used to obtain the far field.

3.2. The Reflector Surface

The reflector surface is described by an analytical equation. This equation may take a variety of forms, depending on whether the surface is a type of conic or not. In general, the surface is described by the equation

$$z = d_0 + d_1x + d_2y + d_3xy + d_4x^2 + d_5y^2 + d_2[P(x,y)]^{d_7}, \quad (3.2a)$$

$$P(x,y) = s_1 + s_2x + s_3y + s_4xy + s_5x^2 + s_6y^2 + s_7x^2y + s_8xy^2 + s_9x^3 + s_{10}y^3 + s_{11}x^2y^2 + s_{12}x^3y + s_{13}xy^3 + s_{14}x^4 + s_{15}y^4. \quad (3.2b)$$

Some examples follow.

3.2.1. Parabolic reflector

In this case the reflector equation is given by

$$z = C_a + \frac{x^2 + y^2}{4f_L} \quad (3.3)$$

where C_a is a constant and f_L is the focal length of the parabola.

3.2.2. Spherical reflector

A spherical reflector may be described by

$$z = C_b - \sqrt{R^2 - x^2 - y^2} \quad (3.4)$$

where C_b is a constant and R is the radius of the sphere.

3.2.3. Hyperbolic reflector

This shape is commonly used for subreflectors. The reflector equation is

$$z = w_0 + w_1 \sqrt{1 + \frac{x^2 + y^2}{w_2^2}} \quad (3.5)$$

3.2.4. Conic section

For a reflector cut from a conic section, the reflector surface is given by

$$\left(z - \frac{ef}{1-e}\right)^2 + \frac{x^2 + y^2}{1-e^2} = \frac{f^2}{(1-e)^2} \quad (3.6)$$

where e is the eccentricity and f is the focal length.

3.2.5. Boundary

Two types of boundaries are frequently used and receive special attention. In the first case, the boundary Γ is the intersection of surface S and an elliptical cylinder (Fig.

3.2a). The parameters of the cylinder are

(x_c, y_c) = center of the ellipse

(K_1, K_2) = semiaxis along (x, y) direction.

In the second case, the boundary Γ is the intersection of S and an elliptical cone (Fig.

3.2b). The cone axis lies along the $(y - y_c) - z$ plane and has the additional parameters

$(x = 0, y = 0, z = -p)$ = tip of cone

θ_3 = inclination angle of cone axis measured from z -axis

(θ_1, θ_2) = half-cone angles in the $(x - x_c) - z$ and $(y - y_c) - z$ planes.

The boundary must be adequately defined in order to calculate the diffracted field (see Section 3.5).

3.3. The Source

The source is assumed to have a well-defined phase center at point P_1 that is the radiating point for a spherical wave (H^i, E^i). When an array feed is used, each radiating element must be considered separately. The scattered fields from each feed element are superimposed to obtain the total field at point P_2 in the aperture plane. It is desired to know the value of the wave (H^i, E^i) where it is incident on the reflector S .

3.3.1. Feed source

The surface current at the radiating aperture of the m th element of the feed array may be expressed as

$$\mathbf{J}_m(x,y) = I_m(\mathbf{e}_x a e^{j\psi} + \mathbf{e}_y b) \quad (3.7)$$

where (a,b,ψ) are real and

$$a^2 + b^2 = 1. \quad (3.8)$$

The parameters (a,b,ψ) are chosen to establish the feed polarization. Table 3.1 shows the values of (a,b,ψ) that correspond to commonly used polarizations.

Table 3.1. Various feed polarizations

	a	b	ψ
linear x	1	0	0
linear y	0	1	0
RHCP	$1/\sqrt{2}$	$1/\sqrt{2}$	90°
LHCP	$1/\sqrt{2}$	$1/\sqrt{2}$	-90°

The radiated electric field due to \mathbf{J}_m given by (3.7) is

$$\mathbf{E}_m = \frac{e^{-jk_r}}{r} \mathbf{f}_m(\theta, \phi) \quad (3.9)$$

where $\mathbf{f}_m(\theta, \phi)$ is the active element pattern of the m th element. The function \mathbf{f}_m may be approximately expressed by

$$\mathbf{f}_m(\theta, \phi) = \mathbf{e}_\theta U_{Em}(\theta) (a e^{j\psi} \cos\phi + b \sin\phi) + \mathbf{e}_\phi U_{Hm}(\theta) (b \cos\phi - a e^{j\psi} \sin\phi) \quad (3.10)$$

where

$U_{Em}(\theta)$ = E-plane active pattern of the m th element

$U_{Hm}(\theta)$ = H-plane active pattern of the m th element.

There are two particular cases of U_{Em} and U_{Hm} that are of interest. The first case is the q -feed [10], where the functions are approximated by

$$U_{Em}(\theta) = (\cos\theta)^{q_{Em}} \text{ volt} \quad (3.11a)$$

$$U_{Hm}(\theta) = (\cos\theta)^{q_{Hm}} \text{ volt} . \quad (3.11b)$$

The second case is the numerical feed. Sometimes it is possible to measure the far-field pattern of an element. In this case, if the pattern can be well approximated by its E-plane and H-plane patterns, it may be easier and/or more accurate to use measured data for U_{Em} and U_{Hm} . In this case, the values for U_{Em} and U_{Hm} are read from a table. The radiated far field of the feed array is the product of the element field (3.9) and the array factor,

$$\mathbf{E}_a = \sum_{m=1}^M \mathbf{E}_m(r) \cdot I_m e^{jk_{eu} \cdot \rho_m} , \quad (3.12)$$

where \mathbf{E}_m is given by (3.9), I_m is the complex excitation coefficient, and

$$\mathbf{e}_u = \sin\theta \cos\phi \mathbf{e}_x + \sin\theta \sin\phi \mathbf{e}_y + \cos\theta \mathbf{e}_z \quad (3.13)$$

$$\rho_m = x_m \mathbf{e}_x + y_m \mathbf{e}_y + z_m \mathbf{e}_z. \quad (3.14)$$

Another feed type that is commonly used is the open-ended waveguide. This feed is evaluated using PO. In this case, the incident fields in the waveguide are assumed to be

the dominant mode in the waveguide (e.g., TE₁₁). The total field in the aperture is the incident field plus the reflected field. The far field is

$$E_R = 0 , \quad (3.15a)$$

$$E_\theta = \frac{jke^{-jkr}}{4\pi r} \left[1 + t \left(\frac{1-\Gamma}{1+\Gamma} \right) \left(\frac{\mu}{\epsilon} \right)^{1/2} \cos\theta \right] (N_x \cos\phi + N_y \sin\phi) , \quad (3.15b)$$

$$E_\phi = \frac{-jke^{-jkr}}{4\pi r} \left[\cos\theta + t \left(\frac{1-\Gamma}{1+\Gamma} \right) \left(\frac{\mu}{\epsilon} \right)^{1/2} \right] (N_x \sin\phi - N_y \cos\phi) . \quad (3.15c)$$

\mathbf{N} is the vector

$$\mathbf{N} = (1 + \Gamma) \int_A \mathbf{E}_t^i e^{jk(x \sin\theta \cos\phi + y \sin\theta \sin\phi)} dS \quad (3.16)$$

and t is defined by

$$t = \frac{\beta_{mn}}{\omega\mu} \text{ for TE-modes} \quad \text{and} \quad t = \frac{\omega\epsilon}{\beta_{mn}} \text{ for TM-modes.}$$

The phase constant is defined by

$$\beta_{mn} = (k^2 - \kappa_{mn}^2)^{1/2} . \quad (3.17)$$

In this report the most-commonly used open-ended waveguide is a circular guide excited by a TE mode (Fig. 3.3). In this case the rectangular components of \mathbf{E}_t^i are [7]

$$E_x = \frac{j\omega\mu\kappa_{mn}}{2} [J_{m-1}(\kappa_{mn}\rho) \sin(m-1)\psi + J_{m+1}(\kappa_{mn}\rho) \sin(m+1)\psi] , \quad (3.18a)$$

$$E_y = \frac{j\omega\mu\kappa_{mn}}{2} [J_{m-1}(\kappa_{mn}\rho) \cos(m-1)\psi - J_{m+1}(\kappa_{mn}\rho) \cos(m+1)\psi] \quad (3.18b)$$

where $J_m(x)$ is the m th-order Bessel function and $J'(\kappa_{mn}a) = 0$, where a is the radius of the waveguide. This leads the far-field expressions

$$E_\theta = j^{m+1} \frac{m\omega\mu}{2r} e^{-jkr} \left[1 + \frac{\beta_{mn}}{k} \cos\theta + \Gamma \left(1 - \frac{\beta_{mn}}{k} \cos\theta \right) \right] J_m(\kappa_{mn}a) \frac{J_m(ka \sin\theta)}{\sin\theta} \sin m\phi , \quad (3.19a)$$

$$E_\phi = j^{m+1} \frac{k a \cos \mu}{2r} e^{-jkr} \left[\frac{\beta_{mn}}{k} + \cos \theta - \Gamma \left(\frac{\beta_{mn}}{k} - \cos \theta \right) \right] \frac{J_m(\kappa_{mn} a) J'_m(ka \sin \theta)}{1 - \left(\frac{k \sin \theta}{\kappa_{mn}} \right)^2} \cos m\phi . \quad (3.19b)$$

3.3.2. Power radiated

We will assume for now a planar feed array. The total radiated time-averaged power of the array, assuming forward radiation only, is given by

$$P_{\text{rad}} = \frac{1}{Z_0} \int_0^{\frac{\pi}{2}} d\theta \int_0^{2\pi} \mathbf{E}_a(r) \cdot \mathbf{E}_a^*(r) r^2 \sin \theta d\phi \quad (3.20)$$

with

$$Z_0 = \sqrt{\frac{\mu_0}{\epsilon_0}} = 120\pi \text{ ohms} . \quad (3.21)$$

Substituting (3.8) into (3.16) gives

$$P_{\text{rad}} = \sum_{m=1}^M \sum_{n=1}^M I_m I_n^* \left[\frac{1}{Z_0} \int_0^{\frac{\pi}{2}} d\theta \int_0^{2\pi} \mathbf{E}_m(r) \cdot \mathbf{E}_n^*(r) e^{jk \mathbf{e}_a \cdot (\rho_m - \rho_n)} r^2 \sin \theta d\phi \right] . \quad (3.22)$$

Defining the power radiated as follows,

$$P_{\text{rad}} = \sum_{m=1}^M \sum_{n=1}^M I_m I_n^* A_{mn} , \quad (3.23)$$

a new term, the power matrix A_{mn} , appears.

3.3.3. Incident field on reflector

Up until now, all positions have been determined in the feed coordinate system. However the reflector surface S is defined in the main coordinate system. The feed coordinate system can be related to the main coordinate system by an orthonormal transformation matrix $\bar{\bar{A}}$

$$[\mathbf{e}_x^F \ \mathbf{e}_y^F \ \mathbf{e}_z^F]^T = \bar{\bar{A}} [\mathbf{e}_x \ \mathbf{e}_y \ \mathbf{e}_z]^T \quad (3.24)$$

Therefore a point $P = (x, y, z)$ on reflector surface S can be expressed in the feed coordinate system by

$$[x^F \ y^F \ z^F]^T = \bar{A}[(x-x_1) \ (y-y_1) \ (z-z_1)]^T \quad (3.25)$$

where $P_1 = (x_1 \ y_1 \ z_1)$ is the location of the first feed element in the main coordinate system.

Using (3.18), E^i can be found at P . The H-field can then be found by the relation

$$H^i = \frac{1}{Z_0} [H_{\theta_F} \ H_{\phi_F} \ H_{r_F}]^T = \frac{r \times E^i}{Z_0} \quad (3.26)$$

The incident field is then converted from spherical coordinates to Cartesian coordinates.

Finally, the H-field is converted to the main coordinate system by using

$$[H_x \ H_y \ H_z]^T = \bar{A}^T [H_{x_F} \ H_{y_F} \ H_{z_F}]^T \quad (3.27)$$

This is repeated for each element in the feed array.

3.4. Geometrical Optics Field

The GO field consists of two parts: the incident field H^i and the reflected field H^r .

The incident field at the observation point P_2 on the aperture grid is taken to be zero, since it does not contribute to the far-field pattern. The first step for determining the reflected field is to locate the reflection point on the reflector surface S .

3.4.1. Reflection point

Given a starting point at the feed $P_1 = (x_1 \ y_1 \ z_1)$ and an ending point P_2 on the aperture grid, a reflection point $O^r = (x \ y \ z=f(x, y))$ on S may exist. The vectors

$$\begin{aligned} d_1 &= e_x(x - x_1) + e_y(y - y_1) + e_z(z - z_1) \\ d_2 &= e_x(x_2 - x) + e_y(y_2 - y) + e_z(z_2 - f(x, y)) \end{aligned} \quad (3.28)$$

are the connecting vectors from P_1 to O^r , and O^r to P_2 , respectively. The condition on the reflection point is that the distance $(d_1 + d_2)$ be a minimum, i.e.,

$$\frac{\partial}{\partial x}(d_1 + d_2) = 0, \quad \frac{\partial}{\partial y}(d_1 + d_2) = 0 \quad (3.29)$$

which can be written explicitly as

$$\begin{aligned} \frac{1}{d_1} \left\{ (x - x_1) + [f(x, y) - z_1] \frac{\partial f}{\partial x} \right\} + \frac{1}{d_2} \left\{ (x - x_2) + [f(x, y) - z_2] \frac{\partial f}{\partial x} \right\} &= 0 \\ \frac{1}{d_1} \left\{ (y - y_1) + [f(x, y) - z_1] \frac{\partial f}{\partial y} \right\} + \frac{1}{d_2} \left\{ (y - y_2) + [f(x, y) - z_2] \frac{\partial f}{\partial y} \right\} &= 0. \end{aligned} \quad (3.30)$$

The root of the two nonlinear equations in (3.30) gives the location of the reflection point. For a given P_1 and P_2 , there may be 0, 1, or more than 1 reflection point. The system of equations in (3.30) could also be solved if the three points are collinear. An additional condition avoids this.

$$\left(\frac{x - x_1}{d_1} + \frac{x - x_2}{d_2} \right)^2 + \left(\frac{y - y_1}{d_1} + \frac{y - y_2}{d_2} \right)^2 + \left(\frac{z - z_1}{d_1} + \frac{z - z_2}{d_2} \right)^2 > \delta \quad (3.31)$$

where δ is a small positive number.

A root may exist but be outside Γ . If

$$l_1 \leq 1 \quad (3.32)$$

then the root is inside the boundary Γ and is in fact a reflection point on the reflector.

Otherwise the point is discarded. The parameter l_1 is given by

$$l_1 = \left[\left(\frac{(x - x_c)}{K_1} \right)^2 + \left(\frac{(y - y_c)}{K_2} \right)^2 \right]^{\frac{1}{2}} \quad (3.33)$$

if Γ lies on an elliptical cylinder and by

$$l_1 = |z|^{-1} \{ [(x - x_c) \cot \theta_1]^2 + [(y - y_c) \cot \theta_2]^2 \}^{\frac{1}{2}} \quad (3.34)$$

if Γ lies on an elliptical cone. The parameters x_c , y_c , K_1 , K_2 , θ_1 , and θ_2 describe the boundary.

3.4.2. Formula for reflected field

The reflected magnetic field at P_2 is given by

$$\mathbf{H}^r(\mathbf{P}_2) = (DF)e^{-jk d_2} \{ \mathbf{H}^i(\mathbf{O}^r) - 2[\mathbf{H}^i(\mathbf{O}^r) \cdot \mathbf{e}_N] \mathbf{e}_N \} \quad (3.35)$$

where DF is the divergence factor and \mathbf{e}_N is the surface normal of the reflector at \mathbf{O}^r . The normal is chosen to be pointing towards the source so that $(\mathbf{e}_N \cdot \mathbf{z})$ is always greater than zero. Explicitly, \mathbf{e}_N is given by

$$\mathbf{e}_N = \Delta(-f_x \mathbf{e}_x - f_y \mathbf{e}_y + \mathbf{z}) \quad (3.36)$$

where

$$\Delta = + (f_x^2 + f_y^2 + 1)^{-\frac{1}{2}} \quad (3.37)$$

and the subscript x of f_x , for example, means partial derivative with respect to x . The divergence factor in (3.35) describes the spreading out of the wavefront and is expressed as

$$DF = \frac{1}{\sqrt{1 + (d_2/R_1^r)}} \cdot \frac{1}{\sqrt{1 + (d_2/R_2^r)}} \quad (3.38)$$

where the square roots take positive real, negative imaginary, or zero values (so that DF is positive real, positive imaginary, or infinite). (R_1^r, R_2^r) are the principal radii of curvature of the reflected wavefront passing through \mathbf{O}^r . Their computation is covered in Section 3.4.3.

3.4.3. Curvatures of reflected wavefront

The formulas from [11] are used in calculating (R_1^r, R_2^r) . The three orthonormal base vectors of the incident pencil are chosen to be (Figure 3.4)

$$\mathbf{e}_1^i = \frac{\mathbf{e}_y \times \mathbf{e}_3^i}{|\mathbf{e}_y \times \mathbf{e}_3^i|} = \frac{\mathbf{e}_x(z - z_1) - \mathbf{e}_z(x - x_1)}{[(z - z_1)^2 + (x - x_1)^2]^{1/2}} \quad (3.39a)$$

$$\mathbf{e}_2^i = \frac{\mathbf{e}_3^i \times \mathbf{e}_1^i}{|\mathbf{e}_3^i \times \mathbf{e}_1^i|} \quad (3.39b)$$

$$\mathbf{e}_3^i = \frac{\mathbf{e}_x(x - x_1) + \mathbf{e}_y(y - y_1) + \mathbf{e}_z(z - z_1)}{[(x - x_1)^2 + (y - y_1)^2 + (z - z_1)^2]^{1/2}} \quad (3.39c)$$

where (x, y, z) are the coordinates of the reflection point O^r . Those of the reflected pencil are chosen to be

$$\mathbf{e}_1^r = \mathbf{e}_1^i - 2(\mathbf{e}_1^i \cdot \mathbf{e}_N) \mathbf{e}_N \quad (3.40a)$$

$$\mathbf{e}_2^r = \mathbf{e}_2^i - 2(\mathbf{e}_2^i \cdot \mathbf{e}_N) \mathbf{e}_N \quad (3.40b)$$

$$\mathbf{e}_3^r = \frac{\mathbf{e}_x(x_2 - x) + \mathbf{e}_y(y_2 - y) + \mathbf{e}_z(z_2 - z)}{[(x_2 - x)^2 + (y_2 - y)^2 + (z_2 - z)^2]^{1/2}} \quad (3.40c)$$

Note that (3.40) establishes a left-hand system, i.e.,

$$\mathbf{e}_1^r \times \mathbf{e}_2^r = -\mathbf{e}_3^r \quad .$$

This does not affect the final solution of (R_1^r, R_2^r) . The three orthonormal basis vectors of reflector S at O^r are chosen to be

$$\mathbf{e}_1^s = \frac{\mathbf{e}_x \times \mathbf{e}_x f_x}{(1 + f_x^2)^{1/2}} \quad (3.41a)$$

$$\mathbf{e}_2^s = \frac{\mathbf{e}_3^s \times \mathbf{e}_1^s}{|\mathbf{e}_3^s \times \mathbf{e}_1^s|} \quad (3.41b)$$

$$\mathbf{e}_3^s = \mathbf{e}_N \quad (3.41c)$$

From (3.39) and (3.41), the elements

$$p_{mn}^i = \mathbf{e}_m^i \cdot \mathbf{e}_n^s, \quad m, n = 1, 2, 3 \quad (3.42)$$

can be calculated with the results

$$p_{11}^i = \frac{(z - z_1) - f_x(x - x_1)}{(1 + f_x^2)^{1/2} [(x - x_1)^2 + (z - z_1)^2]^{1/2}} \quad (3.43a)$$

$$p_{12}^i = \frac{-f_y[(x - x_1) + f_x(z - z_1)]}{\Delta(1 + f_x^2)^{1/2} [(x - x_1)^2 + (z - z_1)^2]^{1/2}} \quad (3.43b)$$

$$p_{21}^i = \frac{-(x - x_1)(y - y_1) - f_x(y - y_1)(z - z_1)}{(1 + f_x^2)^{1/2} \{ (x - x_1)^2(y - y_1)^2 + [(z - z_1)^2 + (x - x_1)^2]^2 + (y - y_1)^2(z - z_1)^2 \}^{1/2}} \quad (3.43c)$$

$$p_{22}^i = \frac{f_x f_y (x - x_1)(y - y_1) + (1 + f_x)[(z - z_1)^2 + (x - x_1)^2] - f_y(y - y_1)(z - z_1)}{\Delta(1 + f_x^2)^{1/2} \{ (x - x_1)^2(y - y_1)^2 + [(z - z_1)^2 + (x - x_1)^2]^2 + (y - y_1)^2(z - z_1)^2 \}^{1/2}} \quad (3.43d)$$

$$p_{33}^i = \frac{1}{d_1} \Delta[f_x(x - x_1) + f_y(y - y_1) - (z - z_1)] \quad (3.43e)$$

The first four elements ((3.43a) - (3.43d)) form the 2×2 matrix \bar{P}^i . Because of the particular choice in (3.40), we have $\bar{P}^r = \bar{P}^i$. The curvature matrix of the incident pencil is

$$\bar{Q}^i = \begin{bmatrix} d_1^{-1} & 0 \\ 0 & d_1^{-1} \end{bmatrix} \quad (3.44)$$

and the curvature matrix of reflector S at O^r is

$$\bar{Q}^s = \begin{bmatrix} e\Delta^2(G - F^2/E) & \Delta(eF - fE)/E \\ \Delta(eF - fE)/E & \Delta^2(gE - 2fF + eF^2/E) \end{bmatrix} \quad (3.45)$$

where

$$E = 1 + f_x^2, \quad F = f_x f_y, \quad G = 1 + f_y^2 \\ e = -\Delta f_{xx}, \quad f = -\Delta f_{xy}, \quad g = \Delta f_{yy}$$

The desired curvature matrix \bar{Q}^r may be calculated from the following matrix equation

$$\bar{Q} = \bar{Q}^i + 2p_{33}^i [(\bar{P}^i)^T]^{-1} \bar{Q}^s (\bar{P}^i)^{-1} \quad (3.46)$$

The four elements of \bar{Q}^r may be denoted by

$$\bar{Q} = \begin{bmatrix} Q_{11} & Q_{12} \\ Q_{21} & Q_{22} \end{bmatrix} \quad (3.47)$$

Then the desired radii of curvature of the reflected wavefront at O^r are given by

$$\frac{1}{R_1^r}, \frac{1}{R_2^r} = \frac{1}{2} \left\{ (Q_{11} + Q_{22}) \pm \sqrt{(Q_{11} + Q_{22})^2 - 4(Q_{11}Q_{22} - Q_{12}Q_{21})} \right\} \quad (3.48)$$

Both R_1^r and R_2^r are real. If the radius is positive, then the corresponding normal section of the reflected wavefront is divergent. If the radius is negative, then the corresponding normal section of the reflected wavefront is convergent.

If there is more than one reflection point, then the total reflected field is the superposition of the reflected fields for each reflection point. If no reflection point exists, then the reflected field is zero. If the reflected point is near the boundary, then the reflected field is calculated as normal, but the diffracted field is adjusted later by using UAT so that the total field is correct.

3.5. The Edge-Diffracted Field

In addition to a reflected field at P_2 , there is also an edge-diffracted field. The first step for finding the diffracted field is to find the diffraction points on the boundary Γ .

3.5.1. Diffraction points

Consider a source point P_1 at (x_1, y_1, z_1) and an observation point P_2 at (x_2, y_2, z_2) with coordinates given in the prime coordinate system (Fig. 3.5). A diffraction point O^d with coordinates (x', y', z') can be determined from Fermat's principle, much as the reflection point was

$$\frac{d}{d\phi'}(d_3 + d_4) = 0 \quad (3.49)$$

where d_3 and d_4 are distances from P_1 to O^d and O^d to P_2 , respectively. This may be rewritten as

$$\left(\frac{g_1 - x_1}{d_3} + \frac{g_1 - x_2}{d_4} \right) \frac{\partial g_1}{\partial \phi'} + \left(\frac{g_2 - y_1}{d_3} + \frac{g_2 - y_2}{d_4} \right) \frac{\partial g_2}{\partial \phi'} + \left(\frac{g_3 - z_1}{d_3} + \frac{g_3 - z_2}{d_4} \right) \frac{\partial g_3}{\partial \phi'} = 0 \quad (3.50)$$

where (g_1, g_2, g_3) are parametric functions describing x' , y' , and z' in terms of ϕ' . A root of this equation is a diffraction point. Depending on the geometry, as many as four diffraction points can exist.

3.5.2. Formula for diffracted field

Each diffraction point has associated with it a contribution to the diffracted field H^d .

The formula is

$$H^d(P_2) = g(kd_4) \frac{1}{\sqrt{1 + (d_4/R_1)}} \frac{1}{\sin\beta} [e_\beta D^h H_\beta^i + e_\alpha D^* H_\alpha^i] \quad (3.51)$$

where g is a cylindrical wave factor

$$g(x) = \frac{1}{2\sqrt{2\pi x}} \exp\left[-j\left(x + \frac{\pi}{4}\right)\right] \quad (3.52)$$

The other factors are explained in more detail in the following sections.

3.5.3. Divergence factor

The square root in (3.51) can be positive real, negative imaginary or zero. R_1 is a radius of curvature of the diffracted wavefront passing through O^d and is found from the equation [11]

$$\frac{1}{R_1} = \frac{1}{d_3} + \frac{\kappa}{\sin^2\beta} [e_{d_3} - e_{d_4}] \cdot e_n \quad (3.53)$$

where β is the angle between tangent t and d_4 . The term κ is the curvature of curve Γ and e_n is the normal of this curve at O^d . This leads to a final expression for the divergence factor of the diffracted field

$$DFD = \frac{1}{\sqrt{1 + (d_4/R_1)}} = \frac{1}{\sqrt{1 + G}} \quad (3.54)$$

where

$$\begin{aligned}
 G = & \frac{d_4}{d_3} + \frac{d_4}{P^4(\sin\beta)^2} \left\{ \left(\frac{x' - x_1}{d_3} + \frac{x' - x_2}{d_4} \right) [g_3(\dot{g}_3\ddot{g}_1 - \dot{g}_1\ddot{g}_3) - g_2(\dot{g}_1\ddot{g}_2 - \dot{g}_2\ddot{g}_1)] \right. \\
 & + \left(\frac{y' - y_1}{d_3} + \frac{y' - y_2}{d_4} \right) [g_1(\dot{g}_1\ddot{g}_2 - \dot{g}_2\ddot{g}_1) - g_3(\dot{g}_2\ddot{g}_3 - \dot{g}_3\ddot{g}_2)] \\
 & \left. + \left(\frac{z' - z_1}{d_3} + \frac{z' - z_2}{d_4} \right) [g_2(\dot{g}_2\ddot{g}_3 - \dot{g}_3\ddot{g}_2) - g_1(\dot{g}_3\ddot{g}_1 - \dot{g}_1\ddot{g}_3)] \right\}
 \end{aligned} \quad (3.55)$$

where a g -prime (g') represents a derivative of g with respect to ϕ' ,

$$\sin\beta = \left| \left(1 - \left\{ \frac{1}{Pd_3} [(\dot{x}' - \dot{x}_1)\dot{g}_1 + (\dot{y}' - \dot{y}_1)\dot{g}_2 + (\dot{z}' - \dot{z}_1)\dot{g}_3] \right\}^2 \right)^{1/2} \right| \quad (3.56)$$

$$P = \sqrt{(\dot{g}_1)^2 + (\dot{g}_2)^2 + (\dot{g}_3)^2} \quad (3.57)$$

3.5.4. Diffraction coefficients

The hard and soft Keller's diffraction coefficients D^h and D^s are defined in Eq. (5.22) of [11] as

$$D^{s,h} = \chi^i + \chi^r = -\sec \frac{1}{2}(\phi - \phi^i) \pm \sec \frac{1}{2}(\phi + \phi^i) \quad (3.58)$$

The angles ϕ and ϕ^i are shown in Figure 3.6. They are calculated from the relations

$$\cos\phi^i = (-1) \frac{(\text{Proj } d_3) \cdot (e_t \times e_n)}{|\text{Proj } d_3|} \quad (3.59)$$

$$\cos\phi = \frac{(\text{Proj } d_4) \cdot (e_t \times e_n)}{|\text{Proj } d_4|} \quad (3.60)$$

Here $\text{Proj } d_3$ is the projection of d_3 on the plane perpendicular to e_t . This can be rewritten as

$$\cos\phi^i = [S_{31}M_1 + S_{32}M_2 + S_{33}M_3][S_{31}^2 + S_{32}^2 + S_{33}^2]^{-1/2} \quad (3.61)$$

$$\cos\phi = [S_{41}M_1 + S_{42}M_2 + S_{43}M_3][S_{41}^2 + S_{42}^2 + S_{43}^2]^{-1/2} \quad (3.62)$$

where

$$S_{31} = (x' - x_1') - \frac{d_3 Q}{P} g_1'$$

$$S_{32} = (y' - y_1') - \frac{d_3 Q}{P} g_2'$$

$$S_{33} = (z' - z_1') - \frac{d_3 Q}{P} g_3'$$

$$S_{41} = (x_2' - x') - \frac{d_4 Q}{P} g_1'$$

$$S_{42} = (y_2' - y') - \frac{d_4 Q}{P} g_2'$$

$$S_{43} = (z_2' - z') - \frac{d_4 Q}{P} g_3'$$

$$M_1 = \frac{1}{P}[N_2 g_3' - N_3 g_2']$$

$$M_2 = \frac{1}{P}[N_3 g_1' - N_1 g_3']$$

$$M_3 = \frac{1}{P}[N_1 g_2' - N_2 g_1']$$

and N_1 , N_2 , and N_3 are the components of \mathbf{e}_N , the normal to surface S , in the (x', y', z') coordinate system.

The solutions of ϕ and ϕ^i are subject to the following tests:

- (i) $0 < \phi^i < \pi$ if $T_3 \geq 0$, and $\pi < \phi^i < 2\pi$ if $T_3 < 0$, where

$$T_3 = (-\text{Proj } \mathbf{d}_3) \cdot \mathbf{e}_N = -S_{31}N_1 - S_{32}N_2 - S_{33}N_3 \quad (3.63)$$

- (ii) $0 < \phi < \pi$ if $T_4 \geq 0$, and $\pi < \phi < 2\pi$ if $T_4 < 0$, where

$$T_4 = (-\text{Proj } \mathbf{d}_4) \cdot \mathbf{e}_N = S_{41}N_1 + S_{42}N_2 + S_{43}N_3 \quad (3.64)$$

- (iii) If the observation point P_2 is exactly on the incident shadow boundary, then

$$\phi - \phi^i - \pi = 0 \quad (3.65)$$

- (iv) If the observation point P_2 is exactly on the reflected shadow boundary, then

$$\phi + \phi^i - \pi = 0 \quad (3.66)$$

When P_2 is on the incident shadow boundary (case iii), the factor χ^i becomes infinite. The resulting computational problem is avoided by moving P_2 slightly whenever this occurs. Similarly, χ^r becomes infinite in case iv, and the same procedure eliminates the problem here also. UAT will be used later to modify the diffracted field H^d to H^D .

3.5.5. Spherical components of incident field

Fields H_β^i and H_α^i from (3.51) are the two spherical components of the incident magnetic field H^i evaluated at O^d in the directions β^i and α^i . The base vectors are shown in Figure 3.7 and may be calculated from

$$e_\beta^i = (e_\alpha^i \times d_3)/d_3 \quad (3.67a)$$

$$e_\alpha^i = (e_i \times d_3)/(d_3 \sin \beta) \quad (3.67b)$$

Then it can be shown that

$$H_\beta^i = \frac{-1}{P \sin \beta} [H_1 g_1' + H_2 g_2' + H_3 g_3'] \quad (3.68a)$$

$$H_\alpha^i = \frac{1}{P d_3 \sin \beta} \{ H_1 [g_2'(z' - z_1') - g_3'(y' - y_1')] + H_2 [g_3'(x' - x_1') - g_1'(z' - z_1')] \\ + H_3 [g_1'(y' - y_1') - g_2'(x' - x_1')] \} \quad (3.68b)$$

where (H_1, H_2, H_3) are the components of H^i in the primed coordinate system.

3.5.6. Rectangular components of diffracted field

The only part that needs to be determined now are the spherical base vectors for the diffracted field, e_β and e_α . They are defined by equations similar to (3.67), namely,

$$e_\beta = (e_\alpha \times d_4)/d_4 \quad (3.69a)$$

$$e_\alpha = (e_i \times d_4)/(d_4 \sin \beta) \quad (3.69b)$$

Once these vectors are determined, they must be expressed in terms of the rectangular components (e_x, e_y, e_z) so that the diffracted field may be superimposed upon the reflected field. The corresponding diffracted E-field is then

$$E^d(P_2) = \frac{120\pi}{d_4} [H^d(P_4) \times d_4] \quad (3.70)$$

3.5.7. Detour parameter

As mentioned in Section 3.5.4, when the observation point is near the reflected shadow boundary, the diffracted field H^d is not valid. The "detour parameter" is used to determine if this happens. From Section VI of [11],

$$\xi = \varepsilon[k(d_3 + d_4 - d_1 - d_2)]^{1/2} . \quad (3.71)$$

Here ε is the shadow indicator of the reflected field and is +1 or -1 if the point is in the shadow or lit region of the reflected field, respectively. It may be shown that

$$\varepsilon = \text{Sgn} \left[-\cos \frac{1}{2}(\phi + \phi^i) \right] \quad (3.72)$$

When the caustic of the reflected field falls on the reflected field shadow boundary, ξ is imaginary; otherwise, it is real. Following the numerical study in [12],

$$|\xi| = 2 \quad (3.73)$$

is the dividing line. This means that if $|\xi| > 2$, then the field H^d is valid. If not then H^d must be replaced by H^D . When ξ is small, $(d_1 + d_2)$ and $(d_3 + d_4)$ from (3.71) are nearly equal and an alternate formula for ξ is used, namely,

$$\xi \approx -\cos \frac{1}{2}(\phi + \phi^i) \sin \beta \sqrt{2k} \frac{\sqrt{d_4[1 + (d_4/R_1)]}}{\sqrt{1 + (d_2/R_1^i)} \sqrt{1 + (d_2/R_2^i)}} \quad \xi \rightarrow 0, \quad (3.74)$$

where the square root in the numerator is the divergence factor of the diffracted field and the square root in the denominator is the divergence factor of the reflected field.

3.5.8. Uniform asymptotic theory

We shall calculate by the UAT developed in [13-15], namely,

$$H^D(P_2) = H^d(P_2) + \left[F(\xi) - \hat{F}(\xi) - \frac{1}{2}(1 - \varepsilon) \right] H^r(P_2) , \quad (3.75)$$

where F is Fresnel integral defined by

$$F(z) = \pi^{-1/2} e^{j\pi/4} \int_z^\infty e^{-jt^2} dt \quad \text{and} \quad (3.76)$$

$$\hat{F}(z) = \frac{1}{2z\sqrt{\pi}} \exp\left[-j\left(z^2 + \frac{\pi}{4}\right)\right] . \quad (3.77)$$

The factor $(1 - \epsilon)/2$ in (3.75) is one if P_2 is in the lit region and zero if it is in the shadow. The multiplier for H^r goes to zero as ξ goes to infinity, so that H^D becomes equal to H^d . Near the boundary, H^D is finite and compensates to make the total field continuous.

3.6. Secondary Pattern Computation

From field equivalence principles, solutions for the far field may be obtained if the tangential fields E_a and H_a on the aperture plane are known. This can be done directly. The following vector quantities may be defined

$$f(u, v) = \iint_{S_a} E_a(x, y) e^{jk(ux + vy)} dx dy \quad (3.78)$$

$$g(u, v) = \iint_{S_a} H_a(x, y) e^{jk(ux + vy)} dx dy \quad (3.79)$$

where

$$u = \sin\theta \cos\phi$$

$$v = \sin\theta \sin\phi$$

$$k = 2\pi/\lambda$$

θ, ϕ = sperical coordinates of the far-field point.

Since the aperture fields are tangential and the far field is assumed to be in the z-direction, f and g will have only x- and y-components. There are three equivalence principles and each leads to a different pair of equations for the the far-field E-field components E_θ and E_ϕ .

(1) Using E_a and H_a

$$E_\theta = \frac{jke^{-jkr}}{4\pi r} [f_x \cos\phi + f_y \sin\phi + Z_0 \cos\theta (g_y \cos\phi - g_x \sin\phi)] \quad (3.80a)$$

$$E_\phi = \frac{jke^{-jkr}}{4\pi r} [\cos\theta (f_y \cos\phi - f_x \sin\phi) - Z_0 (g_y \sin\phi + g_x \cos\phi)] \quad (3.80b)$$

(2) Using H_a

$$E_\theta = \frac{jke^{-jkr}}{4\pi r} Z_0 \cos\theta (g_y \cos\phi - g_x \sin\phi) \quad (3.81a)$$

$$E_{\phi} = -\frac{jke^{-jkr}}{4\pi r} Z_0 (g_y \sin\phi + g_x \cos\phi) \quad (3.81b)$$

(3) Using E_a

$$E_{\theta} = \frac{jke^{-jkr}}{4\pi r} (f_x \cos\phi + f_y \sin\phi) \quad (3.82a)$$

$$E_{\phi} = \frac{jke^{-jkr}}{4\pi r} \cos\theta (f_y \cos\phi - f_x \sin\phi) . \quad (3.82b)$$

This method is exact if the aperture fields are known everywhere. In practice the aperture plane must be truncated in order to employ the FFT.

3.6.1 Fast Fourier transform

Some manipulation of the integrals in (3.78) and (3.79) must be done in order to use the FFT. When the components of the aperture field have been correctly scaled, the fields can be approximated by a double summation over the grid points in the aperture plane. The grid is two-dimensional and covers a portion of the aperture plane that is slightly larger than the reflector, i.e., the grid extends past the projection of the boundary Γ on the aperture plane. Each term includes a scalar constant factor, the Fourier coefficient C_{mn} . After some more manipulation and evaluation of the integrals, the expression for f_x is

$$f_x(u,v) = K \sum_{n=N_1}^{N_2} \sum_{m=M_1}^{M_2} C_{mn} e^{j\pi(m+n)} \frac{\sin\left[\frac{\pi}{\lambda}(m\lambda + u(x_2 - x_1))\right] \sin\left[\frac{\pi}{\lambda}(n\lambda + v(y_2 - y_1))\right]}{\frac{\pi(m\lambda + u(x_2 - x_1))}{\lambda} \frac{\pi(n\lambda + v(y_2 - y_1))}{\lambda}} \quad (3.83)$$

where

$$K = (x_2 - x)(y_2 - y_1) e^{j\frac{\pi}{\lambda}[u(x_1 + x_2) + v(y_1 + y_2)]} . \quad (3.84)$$

Similar results can be obtained for the other far-field components.

3.6.2. Polarization of secondary pattern

The polarization of the secondary pattern is described by the elements (a^P, b^P, ψ^P) . In the planar aperture of the main reflector at $z = 0$, the tangential electrical field polarization can be written

$$\mathbf{E}_{ap}(z=0) = (\mathbf{e}_x a^P e^{j\psi^P} + \mathbf{e}_y b^P) g(x,y) , \quad (3.85)$$

where $g(x,y)$ is the aperture field distribution in the xy plane. From [16] we can define the orthonormal reference and cross-polarization vectors of the secondary pattern by

$$\mathbf{e}_R = \mathbf{e}_\theta (a^P e^{j\psi^P} \cos\phi' + b^P \sin\phi') + \mathbf{e}_\phi (-a^P e^{j\psi^P} \sin\phi' + b^P \cos\phi') \quad (3.86)$$

$$\mathbf{e}_C = \mathbf{e}_\theta (a^P e^{-j\psi^P} \sin\phi' - b^P \cos\phi') + \mathbf{e}_\phi (a^P e^{-j\psi^P} \cos\phi' + b^P \sin\phi') . \quad (3.87)$$

The polarization parameters (a^P, b^P, ψ^P) of the secondary pattern are related to the parameters (a, b, ψ) of the feed by the relationship

$$a^P = a, \quad b^P = b, \quad \psi^P = \psi + \pi . \quad (3.88)$$

For example, this means that an RHCP feed produces an LHCP secondary pattern. This relationship is true only when a single reflector is involved. For the multireflector case this may change. It is important to keep track of the number of reflections in the system in order for the secondary pattern polarization to be correct.

3.6.3. Directivity

Once the ref-pol of the secondary pattern for a single element has been found, the process can be repeated for all of the elements. The total ref-pol of the secondary pattern is

$$\mathbf{E}_R^T = \sum_{m=1}^M \mathbf{E}_{Rm} I_m \quad (3.89)$$

where \mathbf{E}_{Rm} is the ref-pol field for the m th element assuming excitation $I_m = 1$, and I_m is the actual feed excitation.

The directivity of the reference polarization is defined by

$$D_R(\theta, \phi) = \frac{4\pi(\mathbf{E}_R^T)^2}{Z_0 P_{rad}} \quad (3.90)$$

where P_{rad} is the power radiated by the feed. It can be calculated by a brute-force integration over either half-space or all space. The cross-pol directivity may be calculated by a similar method.

3.7. Concluding Remarks

The main usefulness of the AI method is that it is very general in nature. Until recently, when the currents on a reflector were found, steps would be taken to reduce the resulting integral so that its computation would be possible. These steps were usually based upon some aspect of the reflector geometry. With the advent of the supercomputer, this is no longer necessary. A brute-force FFT can be used to evaluate the fields in the aperture without any geometry-based simplifications being made. Since the FFT is not dependent upon the reflector shape, this method may be applied to arbitrary reflectors. In addition, the method may be repeated in order to include additional reflectors.

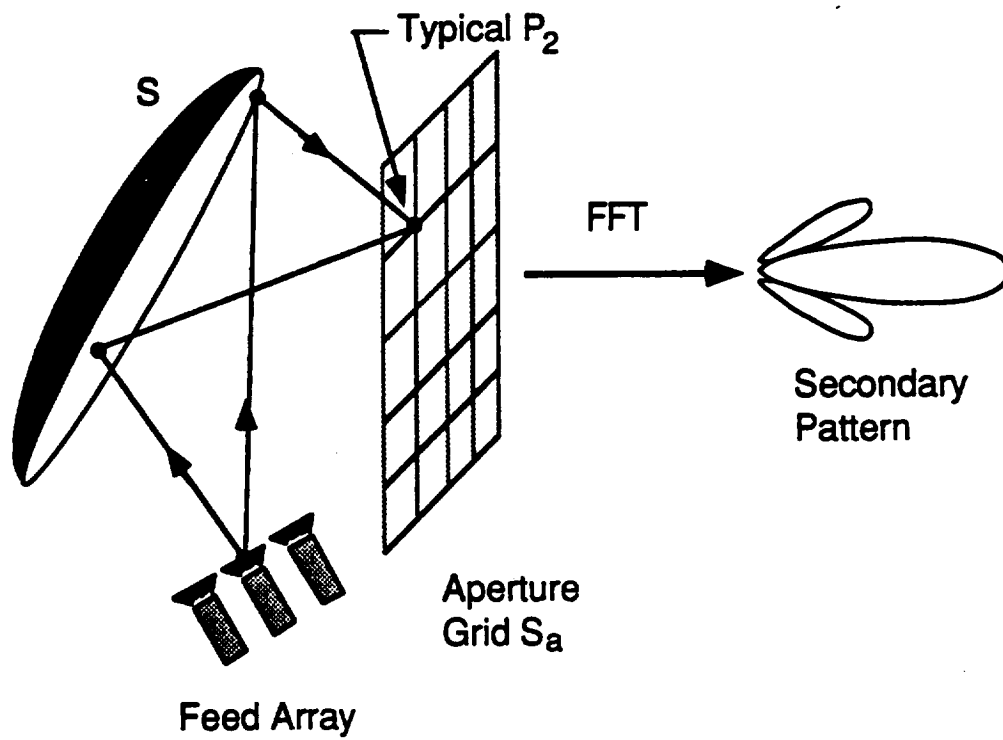
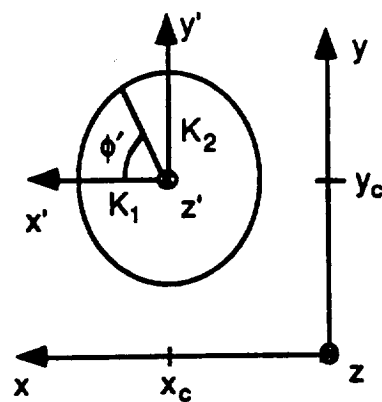
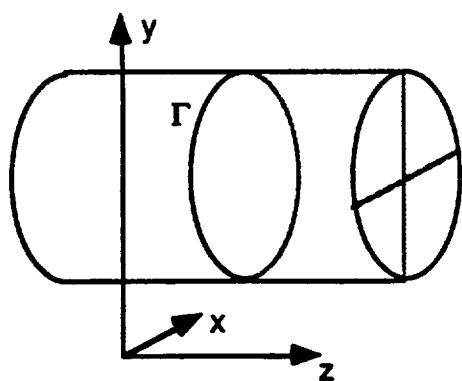
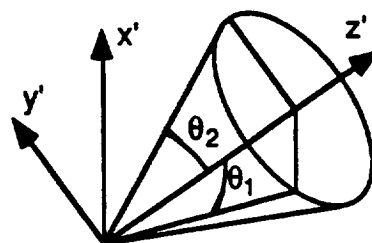
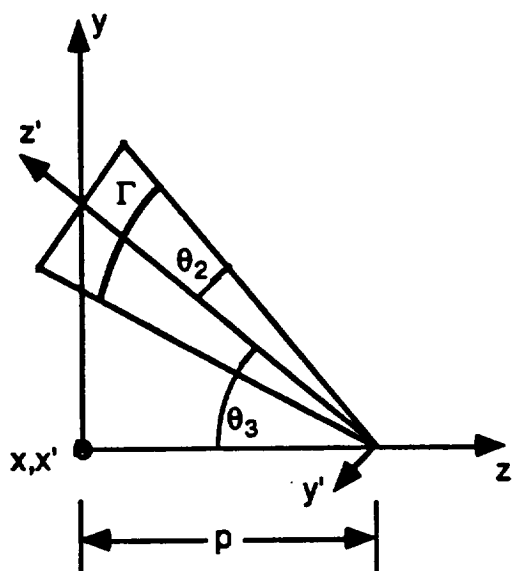


Figure 3.1. Secondary pattern of a reflector antenna using Aperture Integration.



a. Γ on elliptical cylinder



b. Γ on elliptical cone.

Figure 3.2. Two examples of boundary Γ of the reflector.

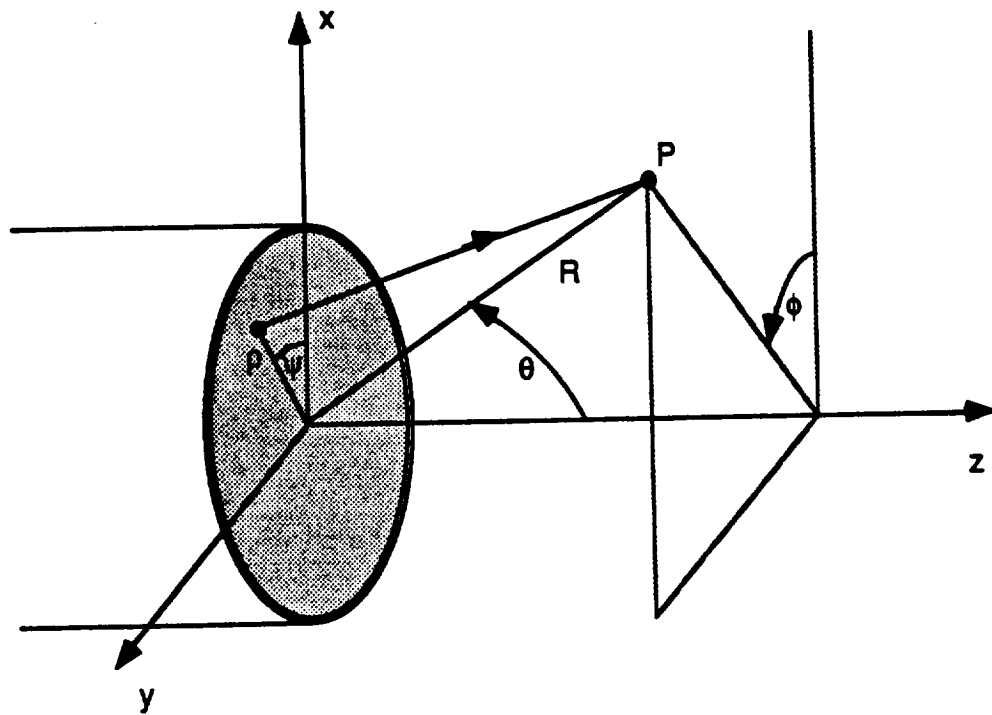


Figure 3.3. Coordinate system used for open-ended circular waveguide.

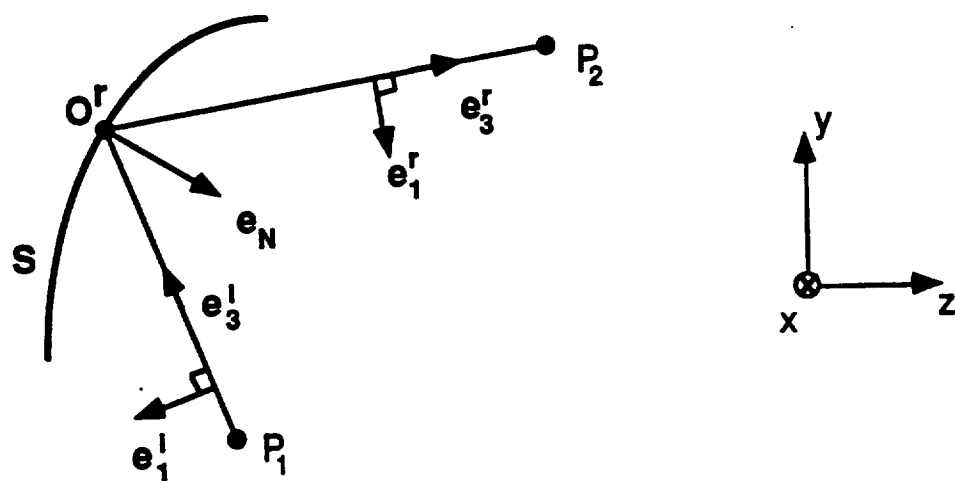


Figure 3.4. Reflection from the reflector S .

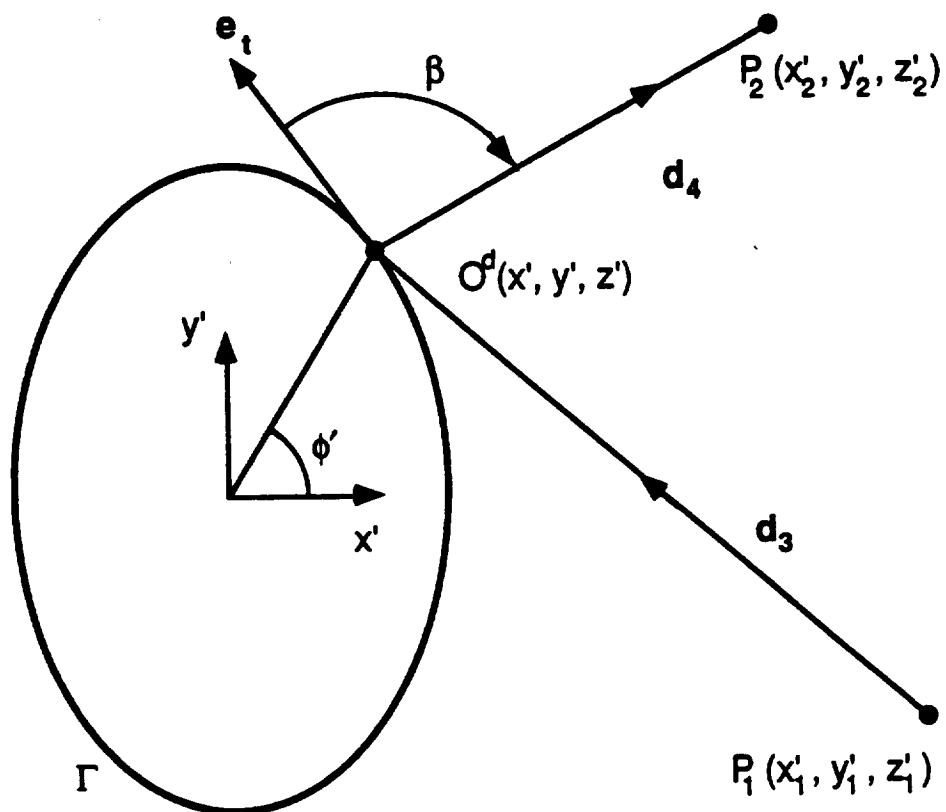


Figure 3.5. Diffraction from boundary Γ of the reflector.

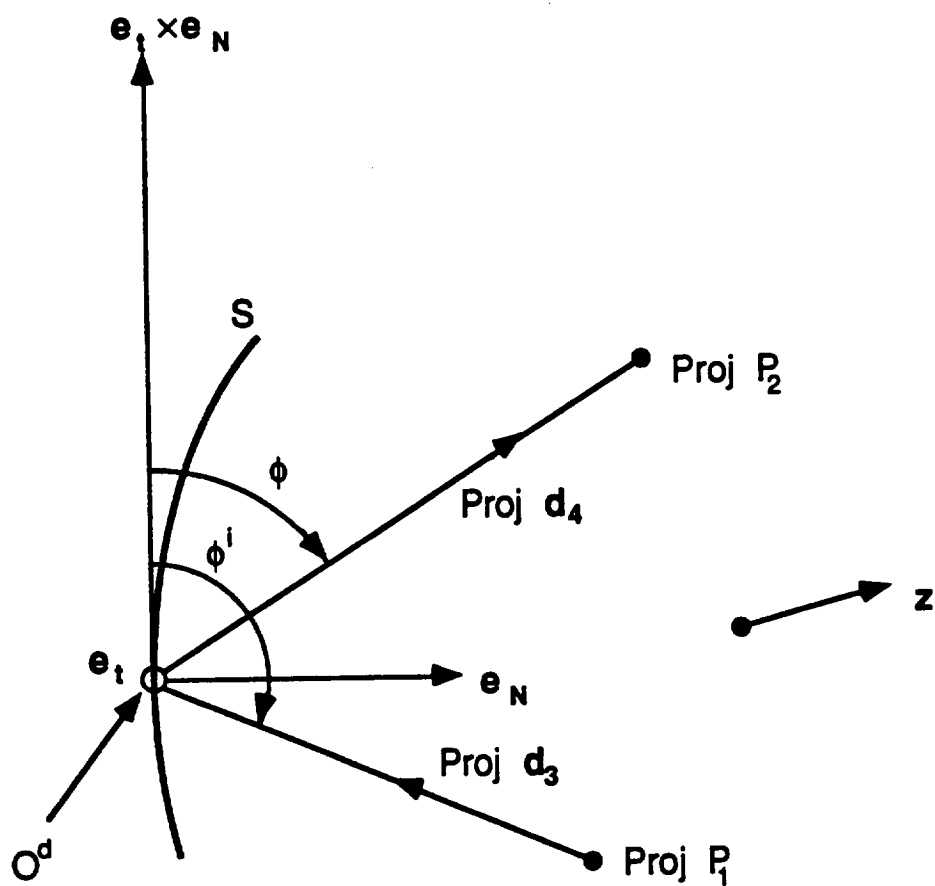


Figure 3.6. Projection of Figure 3.5 on a plane perpendicular to tangent \mathbf{e}_t .

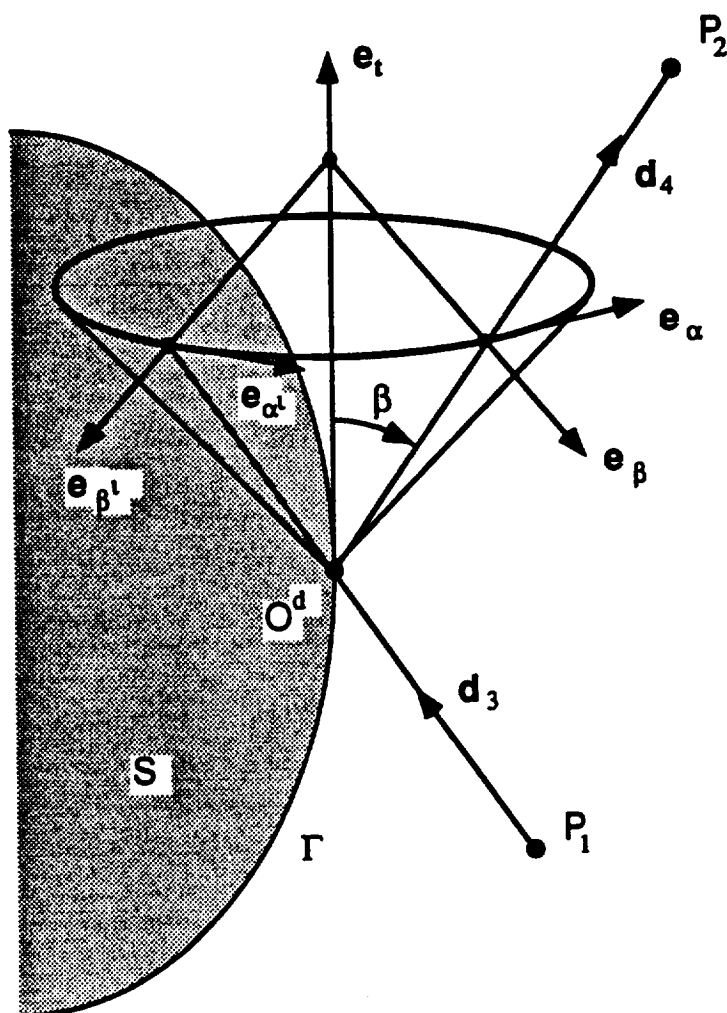


Figure 3.7. Spherical base vectors.

4. WIDE-ANGLE SCANNING FOR REFLECTOR ANTENNAS

Traditionally, reflector antennas are designed for limited scan⁴. A symmetrical parabolic reflector with $f/D=0.4$ can only scan ± 5 beamwidths (BW) with less than 2 dB loss [4]. If the reflector diameter is $1,000 \lambda$, the ± 5 BW scan corresponds to only $\pm 0.5^\circ$, which is a very narrow field of view.

In some future applications, the antenna requirements will be quite different from what they presently are. One example is the NASA Earth Science Geostationary Platform Project. The preliminary antenna specifications are as follows:

Frequency range	20 GHz - 200 GHz
Antenna diameter	15 m ($1,000 \lambda$ - $10,000 \lambda$)
Scan range 1	$\pm 2^\circ$ (± 33 BW - ± 330 BW)
Scan range 2	$\pm 8^\circ$ (± 133 BW - $\pm 1,333$ BW)

Note that the scan requirement has been significantly increased from the traditional value of ± 5 BW. Usually a phased array design is used to satisfy specifications such as these.

A phased array antenna design is an order of magnitude more complicated than a reflector design. This is due to the large number of array elements and the beam-forming network contained in the design. Reflector antennas have the additional advantage of being less expensive and lighter in weight than phased arrays. Therefore, it is desirable to use a reflector antenna design if at all possible. The question then is "Can a reflector antenna be designed that is capable of meeting these specifications?"

This paper examines and compares six different reflector designs. We intend to show how far the reflector performance can be stretched. The object is to achieve a wide-angle scan that will satisfy requirements such as those listed above. The first three designs, P1, P2, and P3, are parabolic single reflector designs. These three designs are considered

⁴ Some of these results have been published in Microwave and Optical Technology Letters in July 1990 [36].

in Section 4.1. The first design is a center-fed, single-element feed design with $f/D=2$ (Fig. 4.1a). Scanning is accomplished by mechanically tilting the reflector. The second design has $f/D=1$ and uses a 19-element cluster feed but, otherwise, is similar to the first design (Fig. 4.1b). The third design is an off-set reflector with $f/D=2$ and an electronically scanned cluster feed (Fig. 4.1c).

The last three designs, C1, C2, and C3, are dual reflector cassegrainian designs. They are considered in Section 3.2. The three designs all use the same reflector geometry. The first design scans by mechanically tilting the main reflector (Fig. 4.2a). The second design scans by mechanically tilting the subreflector (Fig. 4.2b). The last design scans by tilting both the main reflector and the subreflector (Fig. 4.2c).

Data on extremely wide-angle scans of reflector antennas are scarce in the literature. Hung and Mittra [17] in 1986 did analyze a center-fed symmetrical parabolic reflector with a cluster feed and calculate patterns up to a hundred-beamwidth scan. We have verified our single reflector computer code by comparing our results with theirs.

4.1. Single Reflector Antennas

4.1.1. P1: symmetric parabolic reflector with $f/D=2$

Two contributing factors to poor scanning ability are (i) short focal length and (ii) high offset. For these reasons, the first design considered is a symmetrical parabolic reflector with an unusually long focal length. Design P1 has a diameter $D=1,000 \lambda$ and a focal length $f=2,000 \lambda$, thus giving $f/D=2$. The feed is a long circular open-ended waveguide with radius $a=3 \lambda$. A study was done of the directivities and beam efficiencies corresponding to various feed radii. The results are shown in Figure 4.3, with directivities converted to antenna efficiency. Antenna efficiency is defined as the fraction of the nominal directivity that the given directivity is, namely,

$$\eta_{ant} = (\text{Directivity})/(\pi D/\lambda)^2 \quad (4.1)$$

In this case, the nominal directivity $(\pi D/\lambda)^2$ is 69.9 dB. The radius value chosen was that which maximized beam efficiency. The antenna has a half-power beamwidth HPBW=0.07°. Beam efficiency is calculated as the fraction of power hitting the reflector that is contained in the beam defined as being 2.5 times as large as the HPBW [18]. In this case, the beam has a half angle of approximately 0.09°. Note that this definition of beam efficiency does not take into account spillover loss. The chosen radius value of 3λ produces the highest beam efficiency, $\eta=0.91$. Scanning is accomplished by tilting the main reflector. Tilting the main reflector by α degrees results in a scan angle $\theta=2\alpha$. The main advantage of tilting the reflector instead of moving the feed element is that the scan angle is twice the angle of the tilt. If the feed were moved, then the angle of scan would be equal to the angle that the feed was moved through. This is referred to as the mirror effect. Since for any reflector design, the scan loss increases as the feed moves away from the reflector's focal point, a significant reduction in scan loss is gained by tilting the reflector instead of shifting the feed.

Features of reflector P1 are

1. Virtually no feed blockage due to the small size of the single element feed.
2. Depending on the exact arrangement, there is a lossy transmission distance between the feed and the receiver/transmitter. To avoid excessive transmission loss at high frequency applications (60 GHz or more), it may be necessary to connect the feed and the receiver/transmitter via a beam waveguide.
3. Because of the mirror effect, the scan range is twice as far as for the conventional shifted feed design.

The radiation pattern for the on-axis beam is shown in Figure 4.5. The radiation pattern is calculated by a standard physical optics reflector code [19]. The directivity is 66.7 dB which includes the following losses:

Nominal directivity $(\pi D/\lambda)^2$	69.9 dB
Feed spillover loss	- 0.6 dB
Amplitude taper over reflector surface	<u>- 2.6 dB</u>
Directivity	66.7 dB

The above directivity, as usual, does not include the loss due to the feed transmission line. The 3λ radius feed produces a pattern that has a null before the edge of the reflector (Fig. 4.4). This pattern results in a sidelobe level of -31 dB. It is a commonly used rule-of-thumb that to maximize beam efficiency, the first feed pattern null should lie on the reflector edge, which is at $\theta_{\max}=14.25^\circ$. The first null lay on the reflector edge for feed radius $a=2.3\lambda$. This value produces close to a maximum in beam efficiency (see Fig. 4.3).

This reflector has extremely good scan characteristics because of the long f/D and the mirror effect. The scan loss is only 0.6 dB at $\theta_0=8^\circ$ (Fig. 4.6), corresponding to a 114 beamwidth scan. The sidelobe level does increase from -31 dB to -13 dB as expected. At a larger scan angle $\theta_0=20^\circ$ (286 beamwidth scan), the scan loss is 5.1 dB and the pattern is badly distorted with a high shoulder (Fig. 4.7).

4.1.2. P2: symmetric parabolic reflector with $f/D=1$

A drawback of P1 is its excessively long focal length ($2,000\lambda$). Now let us reduce it by one half, giving a $f/D=1$. Then wide-angle scan is possible only if a cluster feed is used. A brief explanation of the cluster feed concept is in order at this point. The feed cluster consists of N identical elements with complex excitations

$$\mathbf{I}=[I_1, I_2, \dots, I_N] \quad (4.2)$$

We wish to determine \mathbf{I} so that, when the beam position is at θ_0 , a prescribed antenna parameter such as directivity, beam efficiency, or sidelobe level is optimized. To this end, let us introduce an element secondary pattern vector \mathbf{E} such that

$$\mathbf{E}(\theta_0)=[E_1(\theta_0), E_2(\theta_0), \dots, E_N(\theta_0)] \quad (4.3)$$

where $E_2(\theta_0)$, for example, is the co-polarization secondary pattern in direction θ_0 when element 2 is excited with

$$\begin{cases} I_2 = 1 \\ I_m = 0, \text{ for all } m \neq 2. \end{cases} \quad (4.4)$$

There exist three methods for determining I in the literature.

- (i) Conjugate Field Matching [20-27]. The cluster excitation is simply set equal to the complex conjugate of $E(\theta_0)$, i.e.,

$$I = [E(\theta_0)]^* \quad (4.5)$$

Strictly speaking, such a choice of cluster excitation does not optimize any particular antenna parameter. For practical purposes, however, it does lead to nearly optimum directivity in most cases.

- (ii) Optimum Directivity [28]. For a feed cluster with prescribed primary patterns and element locations, the directivity in direction θ_0 is optimized by choosing

$$I = \bar{A}^{-1} [\vec{E}(\theta_0)]^* \quad (4.6)$$

where \bar{A} is a $N \times N$ square matrix with elements

$$A_{mn} = \frac{1}{C} \int_0^{4\pi} (E_m E_n) d\Omega \quad (4.7)$$

where C is a normalization constant, and the integration is over 4π - radiation sphere. When the element spacing of the cluster is large (a few wavelengths), matrix \bar{A} is nearly an identity matrix. Then the solution in (4.6) reduces to that in (4.5).

- (iii) Sidelobe Control [29,30]. The element secondary pattern vector E in (4.3) is normally calculated in a transmitting approach. By reciprocity, it can be

calculated equally as well in a receiving approach when the reflector is illuminated by an incident plane wave from direction θ_0 . In the receiving approach, there is an additional advantage that the amplitude of the plane wave can be tapered. It is found that the amount of taper controls the sidelobe level of the final secondary pattern when the whole cluster is turned on.

Return now to P2 in Figure 4.1. A 19-element cluster feed is used. The individual elements are circular feeds with radius $a=1.2 \lambda$. This value is chosen to maximize directivity for a single feed scanned on-axis. This radius feed also produces a relatively good beam efficiency with $\eta=0.88$. The maximum beam efficiency was $\eta=0.89$, which is recorded for a feed with radius $a=1.3\lambda$. Sidelobes for the $a=1.2 \lambda$ feed were -23 dB. This was not nearly the best possible sidelobe value, as a feed with radius $a=1.5 \lambda$ had sidelobes that were -32 dB, along with $\eta=0.87$. The primary pattern of the $a=1.2 \lambda$ circular waveguide feed was approximated by a $(\cos\theta)^q$ pattern with $q=9.5$. This value of q gave good sidelobe matching but the main lobe was 0.6 dB higher, with a maximum directivity of 68.9 dB. Spillover loss for the $\cos^q\theta$ feed pattern was 0.4 dB for $a=1.2 \lambda$. The cluster feed is used to help compensate for the higher scan losses that result from the lower f/D . At small scan angles only the center feed element has a relatively strong excitation (Fig. 4.8a). For an 8° scan (i.e., the reflector is tilted 4°) only two of the outer ring elements have significant excitations (Fig. 4.8b). This indicates that for scans under 8° , a 7-element cluster feed would probably work almost as well as a 19-element feed. When the reflector is tilted 10° for a scan angle of 20° , nearly all of the elements are excited (Fig. 4.8c). At $\theta_0=8^\circ$, the scan loss is 3.7 dB (Figs. 4.9, 4.10), and at $\theta_0=20^\circ$, the scan loss is 7.4 dB (Fig. 4.11). Very similar scan loss results were obtained with $a=1.5 \lambda$ feed. This is not as good as the results for P1, but it is only a few decibels worse. The advantage of P2 over P1 is that the focal length has been cut in half. The disadvantage is that a 19-element feed is much more complicated than a single element feed. For both of these center-fed designs the feed blockage is negligible.

Though design P2 has a higher scan loss at $\theta_0=20^\circ$ than P1, the beam is less distorted (see Fig. 4.7 and Fig. 4.11), because at scan angles of this size, the cluster feed is able to form a much better beam pattern than does a single element feed. For angles below $\theta_0=8^\circ$, there is no benefit to design P1 from using a cluster feed. However, scan loss could be reduced for large scan angles by using a cluster feed.

4.1.3. P3: offset parabolic reflector

Design P3 is an offset parabolic reflector. Offset height must be kept as small as possible to avoid intolerably high scan loss. Unfortunately, small offset leads to serious feed blockage. A possible way out of this dilemma is to use two identical reflector antennas: one for scanning up and one for scanning down as sketched in Fig. 4.1. The focal length is $2,000 \lambda$ and the reflector diameter is $1,000 \lambda$, for a $f/d=2$. The offset height is zero. In contrast to P1 and P2, this design utilizes electronic scanning. This means that a large feed array is used. Up to 19 elements are excited at any time. In order to cover a scan range from $\theta_0=0^\circ$ to $\theta_0=8^\circ$, a semicircular array with a radius of 283λ must be used. The individual feed element has a radius $a=1.065 \lambda$, meaning that roughly 65,000 elements are needed for the entire device. This feed size is chosen so that if the excited element is turned off and an adjacent element is turned on, then the beam is scanned 1 BW. This antenna has an on-axis directivity of 66.2 dB when a single element is turned on. The spillover loss is 3.5 dB. This is quite high since the feed element is so small. Note that this antenna has roughly the same f/D ratio as P1, which uses a feed that is three times larger in radius.

The advantage of the electronic scan is well-known: it is fast and inertialess. However, electronic scanning forces the use of a feed array that has half the diameter of one of the reflectors used. Therefore, this design uses about a fourth as many elements as a phased array with the same aperture size. The savings in complexity are almost lost. In addition, the overall volume occupied by this antenna is much larger than that needed by the previous designs. For the on-axis beam, only the center element of the 19-element cluster

is significantly excited (Figs. 4.12, 4.13), with a directivity of 67.3 dB. This is slightly higher than that excited by a single element feed (66.2 dB). Although excited with small excitations, the surrounding elements do help to reduce the spillover (Fig. 4.15).

Another problem is that the design puts a physical limitation on the maximum scanning angle, because the feed elements do not move. The previous designs could have been scanned farther than 20° if it had been desired. This design has a directivity of 67.3 dB, with $BW=0.06^\circ$ and sidelobes at -18 dB. Patterns were computed at scan angles $\theta_0=0^\circ$ and $\theta_0=8^\circ$. The feed excitations used to obtain these results are shown in Figure 4.12. At $\theta_0=8^\circ$ the scan loss is already 6.3 dB (Fig. 4.13, 4.14). The advantages of electronic scanning are that it is quicker than mechanical scanning and that it will not upset the equilibrium of the spacecraft since there is no physical motion. Some of the drawbacks listed above could be avoided by mechanically moving a 19-element feed cluster instead of electronically scanning. However, this design has much more scan loss at $\theta_0=8^\circ$ than designs P1 and P2.

4.2 Dual Reflector Antennas

4.2.1. C1: cassegrainian reflector with tilted main reflector

Design C1 is a dual-reflector cassegrainian antenna. The main reflector is parabolic with a focal length of $2,000 \lambda$ and a diameter of $1,000 \lambda$ for a $f/D=2$. A Cassegrain antenna may be considered as a folded version of a parabolic reflector. In many applications, it is desirable to reduce the length of the antenna and to place the feed directly behind the vertex of the main reflector. These are the reasons for folding the antenna. With $f/D=2$ for the present case, it is not possible to fold the feed close to the vertex without either excessive spillover loss or an excessively large subreflector or even both. In the present design (Fig. 4.2), the hyperbolic subreflector has a diameter of 115λ and is located $1,650 \lambda$ from the main reflector vertex. The circular feed has a radius $a=1.5 \lambda$ and is located $1,300 \lambda$ from the main reflector vertex. This feed size is chosen to produce 10

dB edge taper on the subreflector. Directivity for this design is 67.1 dB, with BW=0.06° and a -18 dB sidelobe level. Scanning is accomplished by tilting the main reflector. The scan angle $\theta_0 \approx \alpha_1$, where α_1 is the angle at which the main reflector is tilted. The performance of C1, shown in Figures 4.15 and 4.16, is similar to that of P1, the unfolded version of C1. The use of the subreflector does change the aperture taper. Consequently, the sidelobes of C1 and P1 are different.

4.2.2. C2: cassegrainian reflector with tilted subreflector

Design C2 has the same geometry as C1. Scanning is accomplished by tilting the subreflector instead of the main reflector. Due to the substantial difference in size, tilting the subreflector is much easier mechanically than tilting the main reflector. Electrically, however, tilting the subreflector for wide-angle scan is not feasible because

- (i) the subreflector must be tilted by a much larger angle α_2 in order for the beam to scan. The approximate relation between the two angles is

$$\theta_0 \approx \alpha_2 / M$$

where $M = D_{\text{main}} / D_{\text{sub}} = \text{magnification factor}$.

- (ii) When the subreflector is tilted by a large angle, there is an excessive spillover loss.

In this case $M=8.7$. The scan loss is quite high. At $\theta_0=1.75^\circ$, the scan loss is 6.6 dB (Fig. 4.18). At $\theta_0=3.32^\circ$, the scan loss is 36.3 dB. This would seem to indicate that tilting the subreflector is not a viable option for wide-angle scan.

4.2.3. C3: cassegrainian reflector with both reflectors tilted

Design C3 has the same geometry as C1 and C2. Scanning is accomplished by tilting both the subreflector and the main reflector. The idea is to use the main reflector for coarse scanning and the subreflector tilting for local scanning within a small angular region. The scan angle $\theta_0 \approx 2(\alpha_1 + \alpha_2 / M)$. Given α_1 and α_2 , the scan loss can be obtained by looking at the results for C1 and C2.

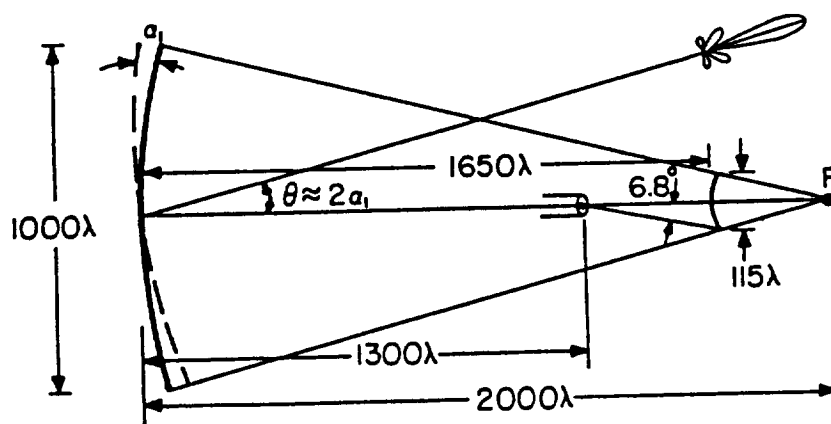
4.3. Conclusions

We have studied the wide-angle scan ability of the six reflector antennas shown in Figures 4.1 and 4.2. All reflectors have a circular diameter of $1,000 \lambda$ and $f/D=2$, except that P2 has a shorter focal length $f/D=1$. The scan loss is summarized in Figure 4.19. Conclusions are listed below.

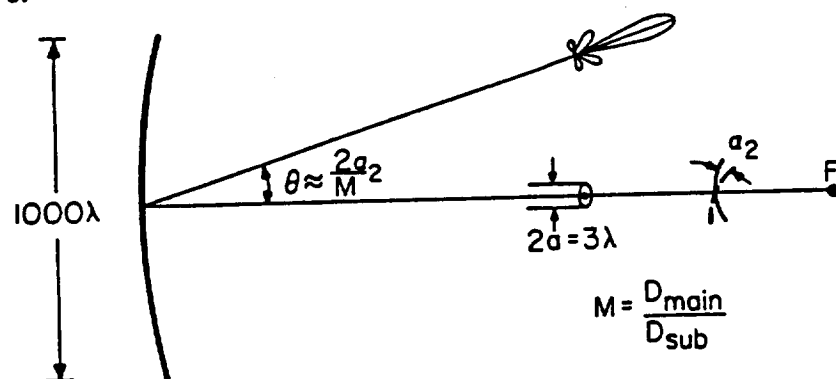
- (i) For mechanical scan by tilting reflectors, the best system is P1. The scan loss at $\theta_0=8^\circ$ (114 beamwidths) is only 0.6 dB (Figs. 4.5, 4.6). The sidelobe level for the $\theta_0=8^\circ$ position is increased considerably (from -31 dB to -13 dB). This problem, which may be alleviated by using the cluster compensation method [25, 27, 29], should be studied.
- (ii) The folded version of P1 is the Cassegrain antenna C1. In the present study, the feed is taken to be a single open-ended circular waveguide with $a=3\lambda$. As a consequence, the amount of folding achieved is small (the length reduction is from $2,000 \lambda$ to $1,650 \lambda$). If more folding is desired, a much larger feed should be used.
- (iii) To shorten the f/D from 2 to 1, reflector P2 must rely on a cluster feed to reduce its scan loss. The excitation of the cluster varies as the beam scans. The scan performance of P2 is still not as good as that of P1, indicating that a 19-element cluster cannot totally compensate for the reduction in f/D .
- (iv) Tilting the subreflector of a Cassegrain antenna can only achieve a small scan (about ± 15 BW). It can be used in conjunction with the electrically more effective but mechanically more costly main reflector tilting to achieve a small local scan.
- (v) Among the six antennas, only the offset parabolic reflector P3 scans the beam electronically. The price is high since (a) there are two identical antennas, one to scan up and one to scan down, (b) the feed has 65,000 elements, and (c)

with a 19-element feed cluster, the scan loss at $\theta_0=8^\circ$ is 6.3 dB. Without the cluster, the loss is 15.4 dB. This is much worse than the 0.6 dB loss for P1.

a. C1: Tilting Main Reflector



b. C2: Tilting Subreflector



c. C3: Tilting Both Reflectors

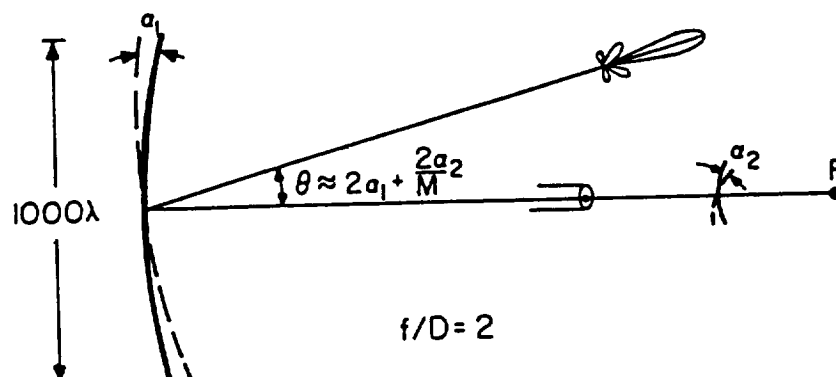


Figure 4.2. Cassegrain dual reflector antenna systems.

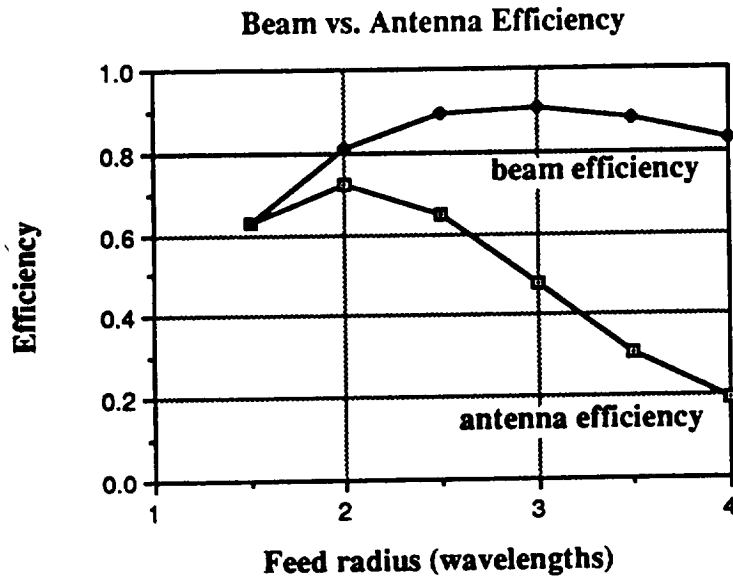


Figure 4.3. Beam efficiency and antenna efficiency for P1 symmetrical parabolic reflector as a function of feed radius. The feed is an open-ended waveguide.

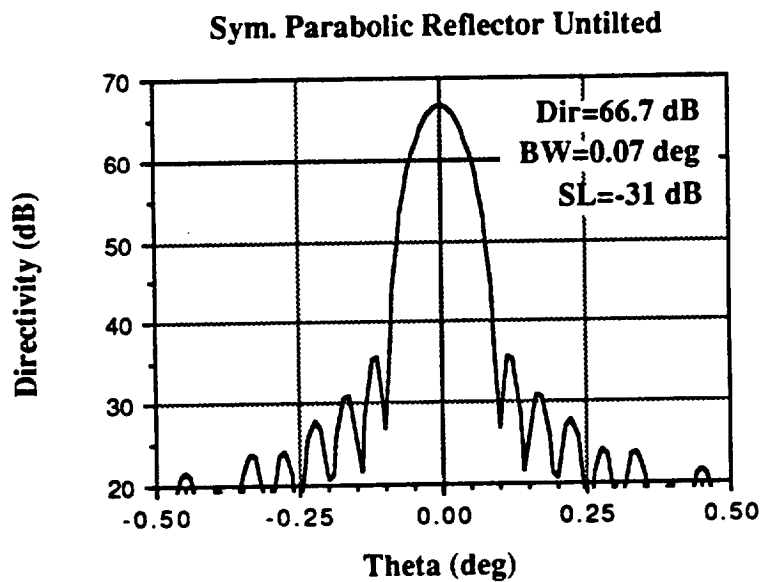


Figure 4.4. P1 symmetric parabolic reflector far-field pattern for 0° scan.

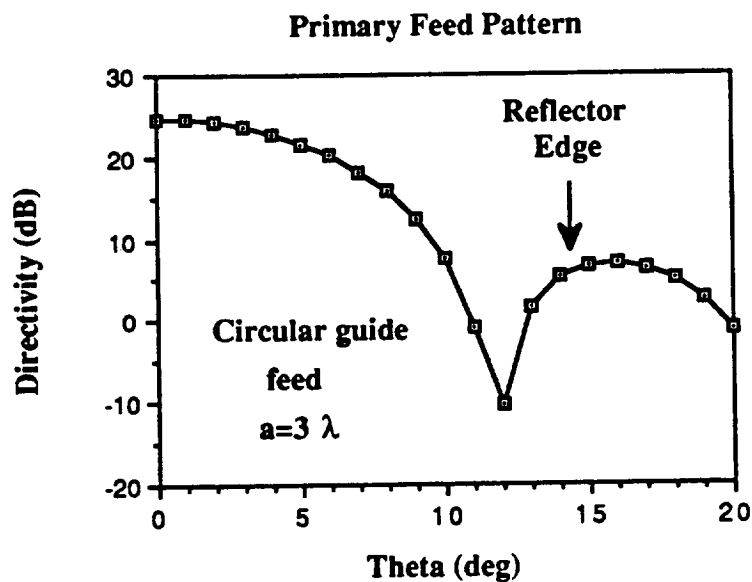


Figure 4.5. Primary feed pattern for P1 symmetrical parabolic reflector. The feed is an open-ended circular waveguide.

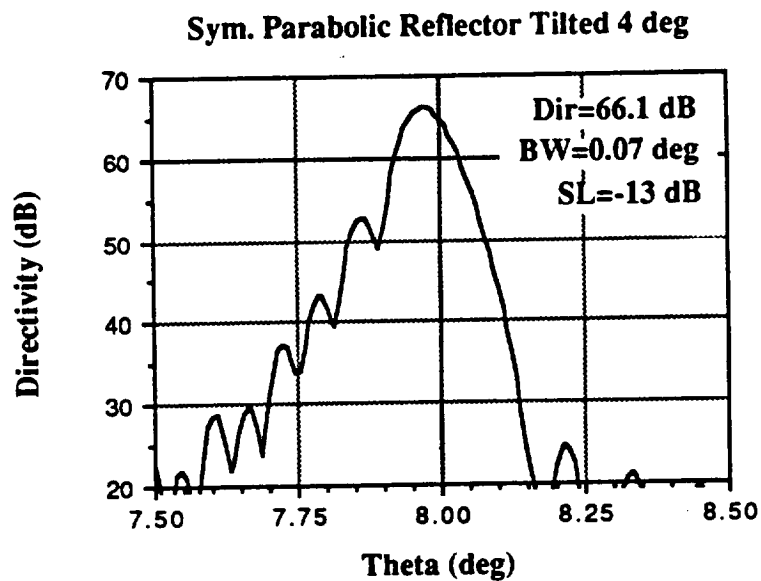


Figure 4.6. P1 symmetrical parabolic reflector far-field pattern for 8° scan (114 beamwidth scan).

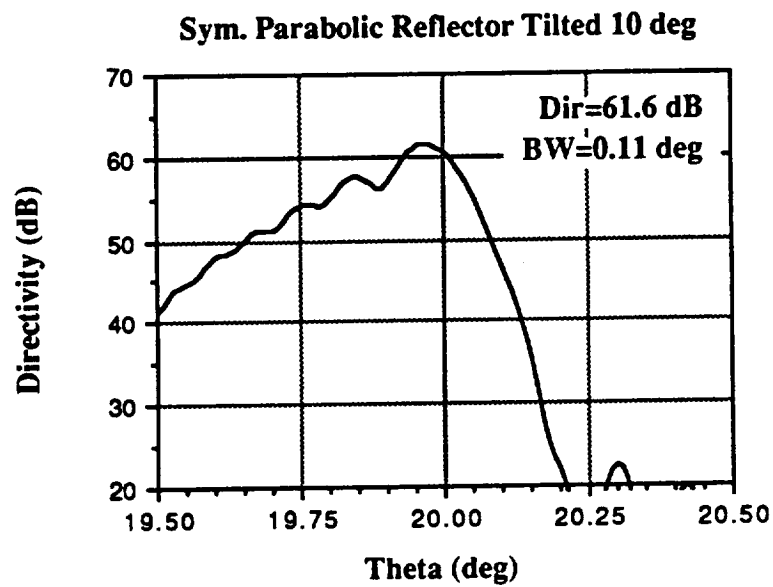


Figure 4.7. P1 symmetrical parabolic reflector far-field pattern for 20° scan (286 beamwidth scan).

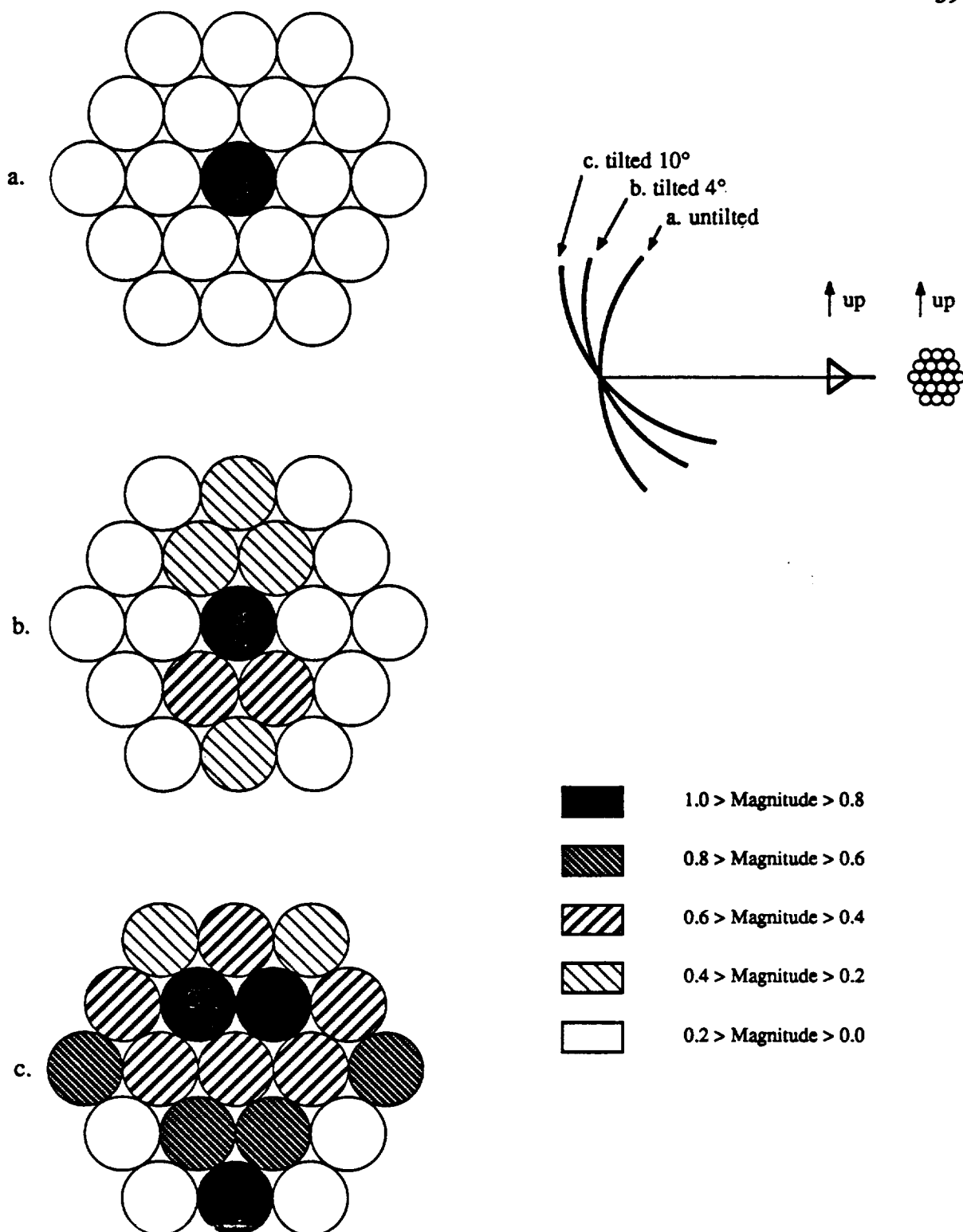


Figure 4.8. Relative excitations for the 19-element feed cluster in P2 symmetrical parabolic reflector: a. beam scanned 0° , b. beam scanned 8° , and c. beam scanned 20° .

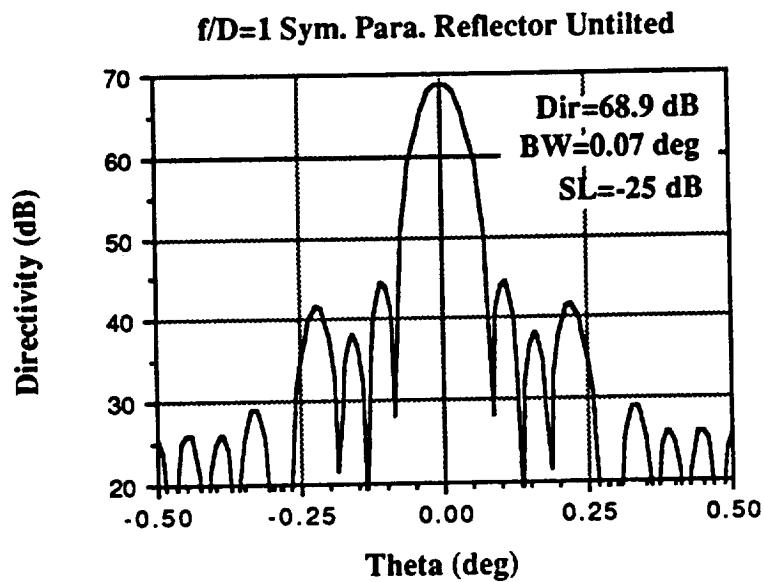


Figure 4.9. P2 symmetric parabolic reflector far-field pattern for 0° scan.

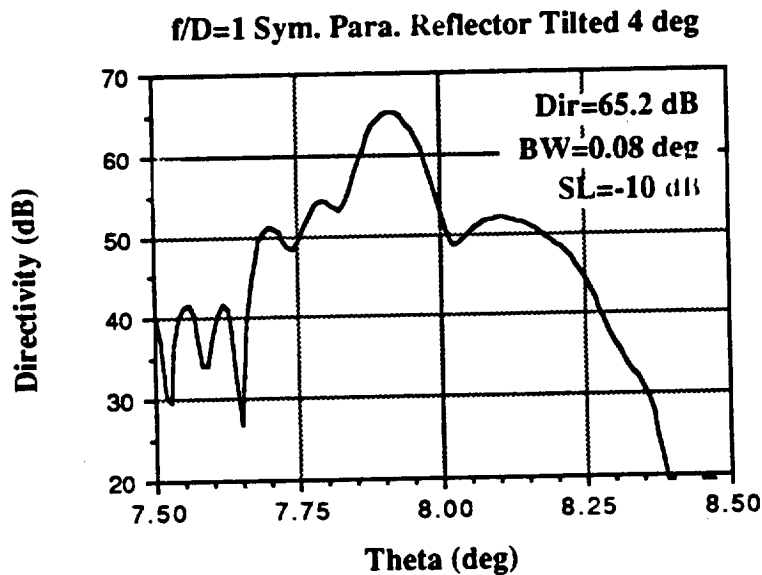


Figure 4.10. P2 symmetric parabolic reflector far-field pattern for 8° scan.

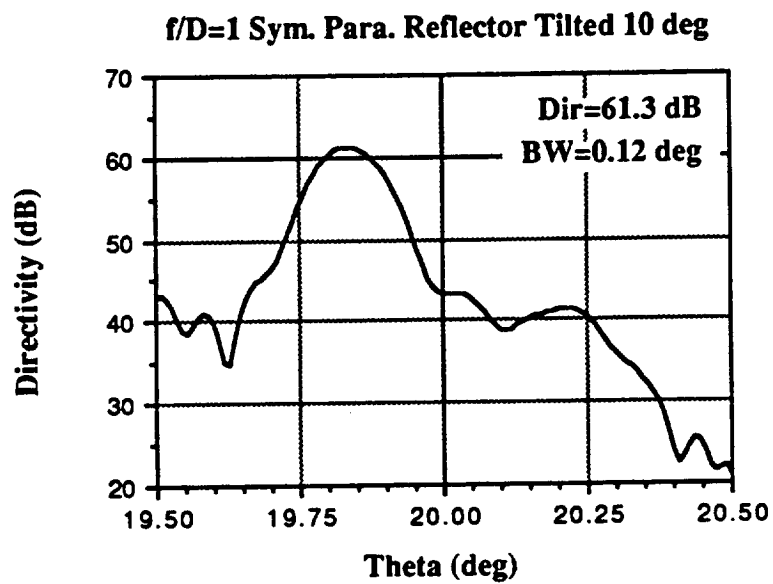


Figure 4.11. P2 symmetric parabolic reflector far-field pattern for 20° scan.

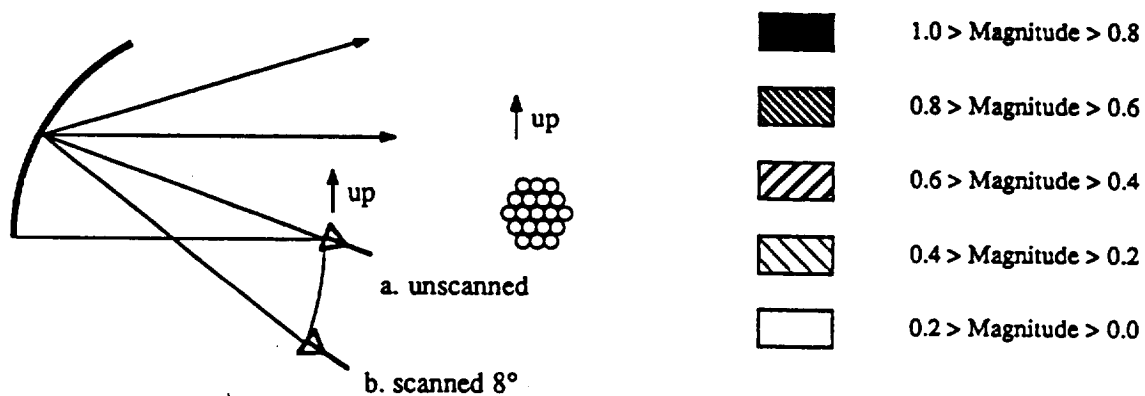
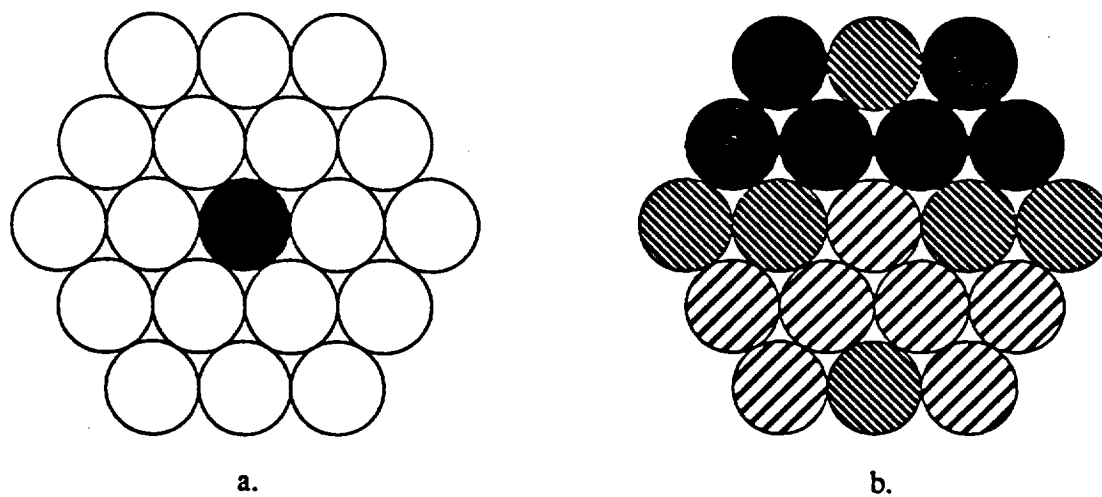


Figure 4.12. Relative feed excitations for the P3 off-set parabolic reflector.
 a. Beam unscanned. b. Beam scanned 8° .

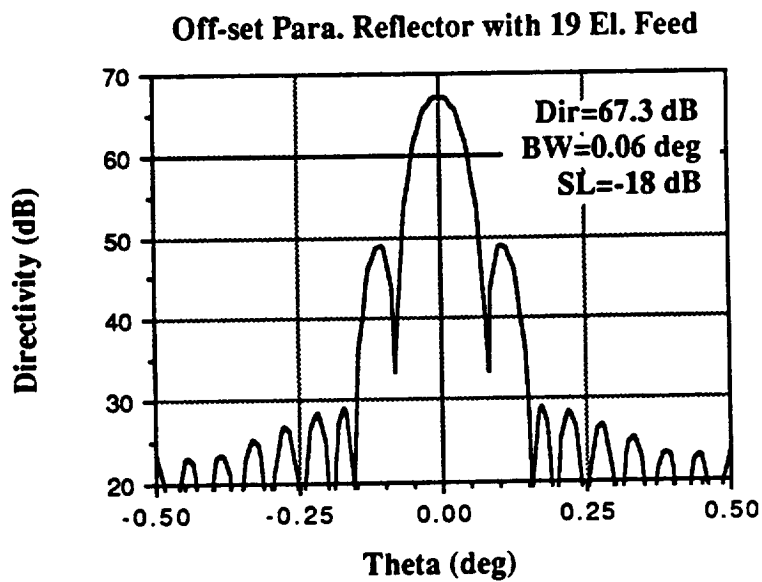


Figure 4.13. P3 offset parabolic reflector far-field pattern for 0° scan.

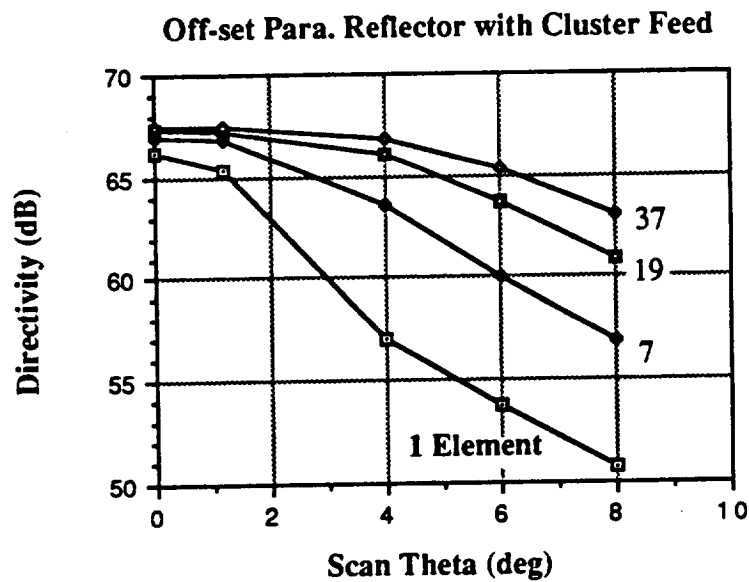


Figure 4.14. Directivity vs. scan for the offset parabolic reflector. Note that as the number of cluster elements increases, so does the directivity.

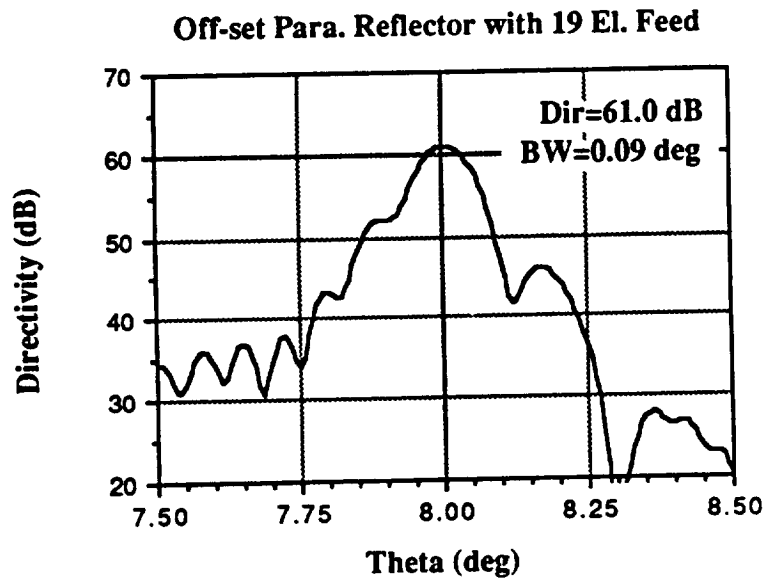


Figure 4.15. P3 offset parabolic reflector far-field pattern for 8° scan.

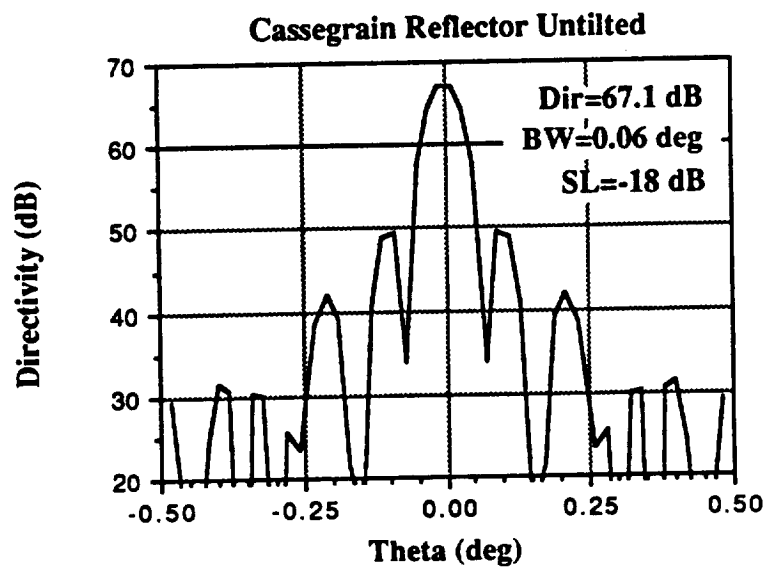


Figure 4.16. Symmetrical cassegrainian reflector far-field pattern for unscanned beam. C1, C2, and C3 have identical patterns for this case.

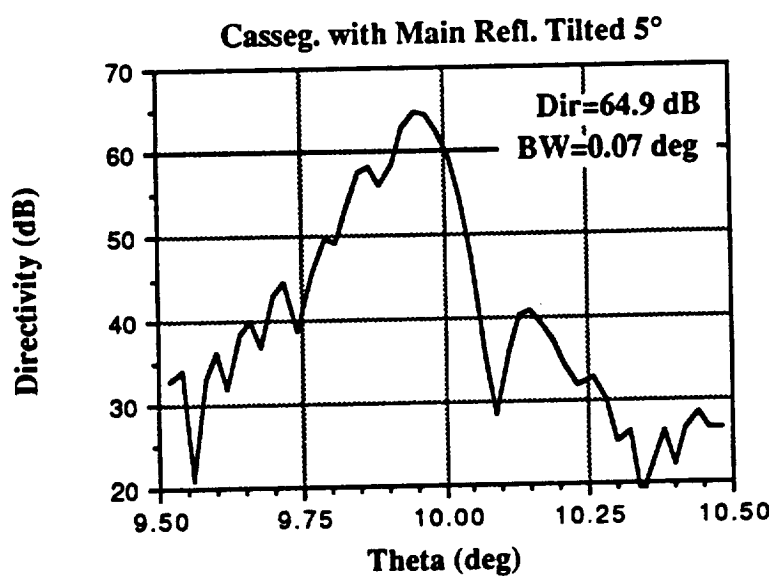


Figure 4.17. C1 symmetrical cassegrainian reflector far-field pattern with main reflector tilted to produce 9.96° scan.

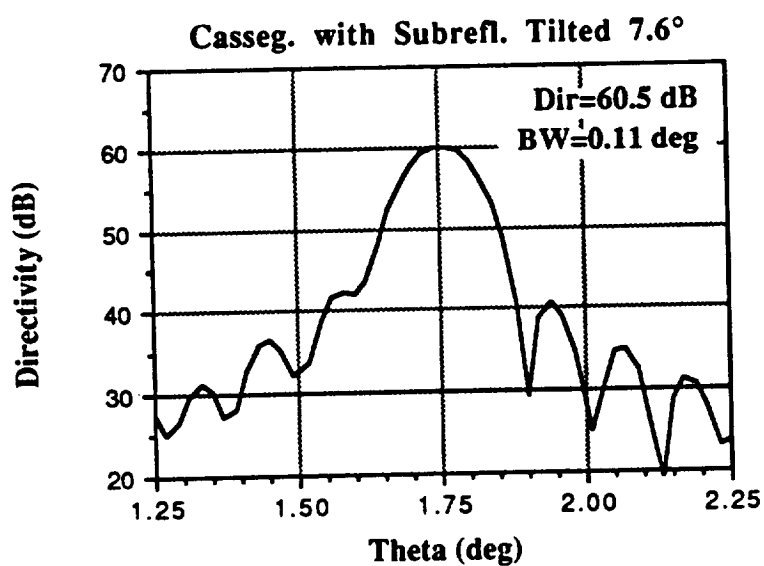


Figure 4.18. C2 symmetric cassegrainian reflector far-field pattern with subreflector tilted to produce 1.75° scan.

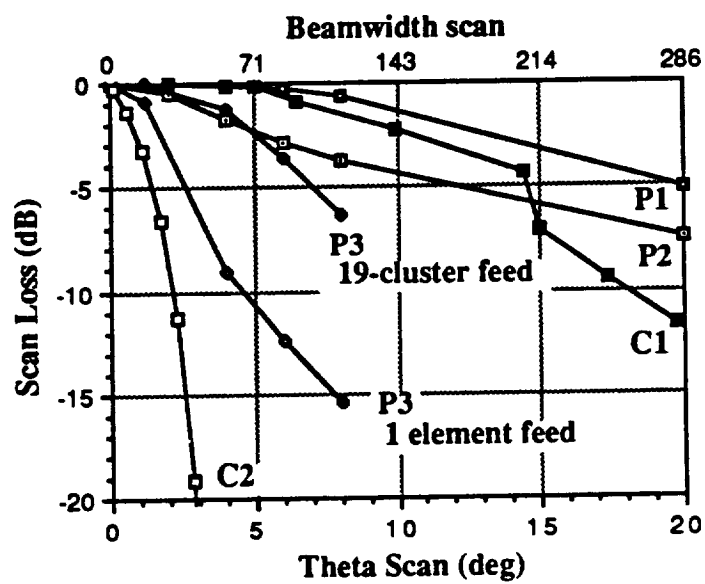


Figure 4.19. Scan loss of the six reflector antennas shown in Figures 4.1 and 4.2.

5. COMPUTATION AND OPTIMIZATION OF BEAM EFFICIENCY

When a reflector antenna is used for a radiometer application, the important figure of merit is its beam efficiency, not its directivity. In contrast to directivity, there are virtually no published results on beam efficiency for a reflector antenna. Typical beam efficiency curves exist only for idealized distribution over a circular aperture [31-33]. These are useful for general trend prediction, but do not describe the dependence of the exact reflector geometry and its feed.

In this chapter, several topics concerning computation and design aspects of beam efficiency are addressed, namely,

- (i) a discussion of three definitions of beam efficiency,
- (ii) the numerical accuracy problem arising from pattern computation codes based on physical optics theory, and a method for overcoming this problem,
- (iii) typical beam efficiency data for parabolic reflectors with a circular horn feed,
- (iv) optimization of beam efficiency by a cluster of feeds.

5.1. Three Definitions

Beam efficiency is a measure of how well an antenna manages to transmit its power within a prescribed narrow cone. It is defined as the percent of total radiated power contained in the main beam

$$\eta = \frac{P_{\text{beam}}}{P_{\text{feed}}} \times 100\% \quad (5.1)$$

where P_{feed} is the power radiated from the feed of the reflector (not including the feed mismatch loss). The unsettled question then is how the main beam is defined. Traditionally the main beam is taken as an angular region within a circular cone with a half cone angle θ_{beam} [31],[18], where

θ_{beam} = polar angle measured from the main beam (where $\theta=0^\circ$) to the first null of the pattern. (5.2)

The definition in (5.2) is sometimes difficult to apply. For a measured antenna pattern, the first null is generally not symmetrically located in all cuts, and may not be clearly identifiable. Hence, a more practical definition for the main beam is [18]

$$\theta_{\text{beam}} = 2.5 \times \theta_{3\text{dB}} \quad (5.3a)$$

where

$$\theta_{3\text{dB}} = \text{half beamwidth defined by 3 dB down points.} \quad (5.3b)$$

The second definition also has a drawback. While optimizing the beam efficiency of a reflector antenna, it encourages excessive edge taper so that the 3dB beamwidth is very wide. That leads to an antenna design with high beam efficiency but poor directivity and poor aperture efficiency. This drawback is due to the fact that $\theta_{3\text{dB}}$ is a moving target, which prevents a fair comparison between two patterns with different edge tapers.

In light of the above discussion, we propose a third definition, namely, the actual half beamwidth $\theta_{3\text{dB}}$ in (5.3) is replaced by a nominal half beamwidth, which is a prescribed number, not a moving target. For a given reflector diameter D , the nominal beamwidth depends on how much one is willing to sacrifice the aperture efficiency for the sake of improving beam efficiency. A good choice that conforms to current practice is

$$\bar{\theta}_{3\text{dB}} = \frac{36^\circ}{(D/\lambda)} \quad (5.4)$$

This choice was arrived at by choosing an ideal aperture distribution with 20 dB edge taper. This distribution (5.4) gives the correct location of the 3 dB down point. Therefore, definitions 2 and 3 are the same for a reflector antenna having a 20 dB aperture taper. This edge taper is chosen because it is a good compromise between low directivity loss (0.9 dB) and high beam efficiency (98%, not counting spillover). If a reflector antenna does not have a 20 dB edge taper, then definitions 2 and 3 can yield very different results.

Definition 3, however, is better since it does not lead to the use of patterns with excessively wide beamwidths as definition 2 does.

5.2. The Problem with Direct Computation

Given the secondary pattern of the reflector, a straightforward method to evaluate power in the main beam, denoted by P_{beam} , is to integrate the field over the main beam, namely,

$$P_{\text{beam}} = \frac{1}{120\pi} \int \int_{\Delta\Omega} |E|^2 d\Omega \quad (5.5)$$

where $\Delta\Omega$ is the half-cone solid angle. This works if the secondary pattern is known accurately. To obtain a 2% accuracy in efficiency, the pattern near the main beam region must be accurate within 0.086 dB. Such an accuracy is not attainable by standard pattern computation methods, which are invariably based on the physical optics (PO) theory. The reason can be traced to the fact that the PO does not conserve power. The finiteness of the energy condition is not obeyed by the scattered fields which result from the assumed surface fields [34]. Technically, this means that the divergence theorem can not be used in deriving integral representations for these fields. If we carried out the integral in (5.5) over the entire 4π space, the power in the pattern generally does not match the power incident on the reflector, which is feed radiated power minus the spillover. This is due to truncation of the surface currents at the reflector edge. We shall use an example to illustrate our point.

Consider a center fed parabolic reflector with

Reflector diameter = $2a = 100 \lambda$

$F/D = 2.0$

Feed: TE₁₁ mode of a circular waveguide with diameter 1.8λ

located at the focal point.

Edge taper = 10 dB

Spillover loss = 16% (-0.75 dB)

Its secondary pattern calculated by a PO code is shown in Fig. 5.1. We integrate this pattern to calculate the power within a cone with half cone angle θ_{cone} . The result is shown in Fig. 5.2. Interpolating Fig. 5.2 conservatively out to $\theta = 90^\circ$ results in a total of less than 96% power when spillover loss is added in. This clearly indicates that the secondary pattern is not entirely accurate and, therefore, power is not conserved. Unfortunately, there does not seem to be a simple fix to make PO-based pattern codes more accurate (adding fringe current does not solve the present accuracy problem). Since the error is caused by truncation of surface currents at the reflector edge, the error is less for cases in which the edge taper is higher. For the same reflector with a 2.4λ radius feed (30 dB edge taper), the sum of the radiated power and spillover power is 99%.

For the pattern in Fig. 5.1, let us compare the three definitions for the main beam:

$$\theta_{\text{beam}} = \begin{cases} 0.86^\circ & \text{using definition in (5.2)} \\ 0.85^\circ & \text{" (5.3a)} \\ 0.90^\circ & \text{" (5.4)} \end{cases}$$

which gives beam efficiencies, respectively, of 75.5%, 75.5%, and 75.6%. In general, the difference in computed beam efficiency will not vary significantly (i.e., the difference in efficiency is only a few percent) for values of θ_{beam} calculated using the various definitions, since the difference between the two solid cone angles is a thin ring located in the neighborhood of a pattern null. When a much larger feed (3.0λ) is used, the respective beam efficiencies from the three definitions are 90%, 90%, and 88%.

5.3. Indirect Computation of Beam Efficiency

In order to achieve beam efficiency results more accurate than those in Section 5.2, an indirect method of computation will be described here. The calculated secondary pattern is calibrated by an ideal aperture distribution, whose far-field pattern and power enclosed in the far-field pattern can both be obtained via closed-form solutions. If the calculated

pattern's power enclosed graph (e.g., Fig. 5.2) is matched carefully to an ideal pattern, then the resulting beam efficiency calculation should be more accurate than for the direct computation method.

The following definition is used for calculating beam efficiency by the indirect method. The beam efficiency η is defined as

$$\eta = \eta_{\text{pat}} \eta_{\text{acc}} \eta_{\text{feed}} \quad (5.6)$$

where the various elements are defined as follows:

η_{pat} : The calculated secondary pattern is examined for relative accuracy. Causes of inaccuracies could include overly sparse FFT grids or other errors caused by numerical integration. At this point, inaccuracy due to nonconservation of power by the PO method is ignored. It is only really necessary for the pattern to be accurate over the first few sidelobes since that is where almost all of the power in the secondary pattern is located. The cutoff point for the accurate region is denoted by θ_{acc} . Then the pattern efficiency is defined as

$$\eta_{\text{pat}} = \frac{P(\theta_{\text{beam}})}{P(\theta_{\text{acc}})} \quad (5.7)$$

where $P(\theta)$ is the power inside the cone half-angle θ (Fig. 5.3).

η_{acc} : The exact definition of η_{acc} is

$$\eta_{\text{acc}} = \frac{P(\theta_{\text{acc}})}{\text{Power in the actual pattern}} \quad (5.8)$$

Because of the nonpower conservation of the PO-based pattern code, it can be difficult to calculate the power in the actual secondary pattern. Here, we propose an approximation. An ideal closed-form solution for the far-field pattern is used. The following aperture amplitude distribution is assumed:

$$Q(\rho) = C + (1 - C)[1 - (\rho/a)^2]^P \quad (5.9)$$

where the parameter C is the aperture edge taper in decibels ($ET = 20\log C$) and the parameter P is used to change the shape of the taper (Fig. 5.4) [4]. A similar distribution is used in Equation 2 of [31]. If the feed blockage is negligible, then the far-field integration over the aperture produces

$$T = \pi a^2 [C \Lambda_1(ka \sin \theta) + (1 - C) \Lambda_{P+1}(ka \sin \theta)] \quad (5.10)$$

where

$$\Lambda_n(\zeta) = 2^n \Gamma(P+1) \frac{J_n(\zeta)}{\zeta^n} \quad (5.11)$$

The total amount of power in this far-field pattern can be easily determined. Note that the pattern is plotted versus $ka \sin \theta$. For a given antenna, the reflector radius a is fixed and the pattern truncates at $ka \sin \theta = ka$ [4]. This can then be converted into the cone half-angle θ . Then, the η_{acc} defined in (5.8) is approximated by

$$\eta_{acc} \approx \eta_{acc}(\text{ideal}) \quad (5.12)$$

η_{feed} : The feed efficiency, η_{feed} , is a measure of how much of the power radiated from the feed hits the reflector(s). This term takes into account spillover loss. In some previous works it is referred to as feed efficiency factor [31], which is a function of the feed pattern and the angle subtended by the reflector dish [35]. For a multiple reflector antenna system, η_{feed} would appear once for each reflector.

As an example of the indirect method described in (5.6), consider the following case of a symmetric parabolic reflector with the following parameters:

Reflector diameter = $2a = 1,000 \lambda$

Feed: TE₁₁ mode of a circular waveguide with diameter 1.8λ located at the focal point

Edge taper = 10 dB

Spillover loss = 18% (-0.85 dB)

Its secondary pattern is shown in Figure 5.5. From the calculated pattern, we find $\theta_{\text{beam}} = 0.090^\circ$ (using (5.4)) and we choose $\theta_{\text{acc}} = 4.2^\circ$. This leads to a pattern efficiency $\eta_{\text{pat}} = 0.956$ (Fig. 5.6). Using the ideal pattern with $p = 1.0$ and a 10 dB edge taper leads to $\eta_{\text{acc}} = 0.997$. The feed efficiency is $\eta_{\text{feed}} = 0.822$. The resulting beam efficiency is $\eta = 78\%$. On the other hand, a direct (conventional) calculation using (5.1) leads to $\eta = 76\%$. When a 2.2λ radius feed is used, the corresponding efficiencies are 88% and 86%, respectively. Therefore, as expected, the PO error leads to the efficiency being 1-2% low. A limitation of the indirect method is that it can only be used in symmetric situations, since the ideal pattern is symmetric.

5.4. Optimization of Beam Efficiency for Cluster Feeds

5.4.1. Use of cluster feeds

In some reflector applications a cluster feed consisting of multiple elements is used instead of a single feed element. This cluster feed can be used in two different ways:

- **One-to one Excitation** in which only one feed in the array is used to produce one beam.
- **Cluster Excitation** in which a group of feeds (normally 7 to 50) is used to produce one beam.

The cluster excitation method can produce a more desirable secondary pattern due to its higher number of degrees of freedom. The complexity of the feed is also higher for the cluster excitation method. The complexity is outweighed if sufficient improvement in the results is obtained.

By properly setting the excitations of the cluster elements, it is possible to optimize various performance parameters of the reflector antenna. In the past, this has been done for optimizing the directivity for wide-angle scans [17,24,36], compensating reflector surface distortion [17], reducing sidelobes [24,29,30], etc. In this section we apply the cluster

excitation to optimize the beam efficiency. This optimization is solved by means of a matrix formulation similar to that employed in [36].

5.4.2. Matrix formulation

Consider a reflector antenna with N feed elements (Fig. 5.7). When element m is excited with a unit amplitude ($J_m = 1$) while all other elements are idle ($J_n = 0$ for $n \neq m$), the secondary pattern from the reflector is called the active element secondary pattern of element m and is denoted by $E_m(r)$. In particular, we are interested in the reference polarization of $E_m(r)$, namely,

$$E_m(r) \cdot R^* = \frac{e^{-jkr}}{r} E_m^{\text{ref}}(\theta, \phi), \quad kr \rightarrow \infty \quad (5.13)$$

Here, R and C are two unitary vectors describing the reference and cross polarizations. If all of the feed elements are excited with weighted amplitudes $\{J_m\}$, the composite secondary pattern is given by

$$Q(\theta, \phi) = \sum_{m=1}^N J_m E_m^{\text{ref}}(\theta, \phi) \quad (5.14)$$

The radiated power within the main beam of pattern $Q(\theta, \phi)$ is

$$\begin{aligned} P_{\text{beam}} &= \frac{1}{Z_0} \iint_{\text{beam}} Q Q^* d\Omega \\ &= \sum_{m=1}^N \sum_{n=1}^N J_m^* B_{mn} J_n = (J^*)^T \bar{B} J \end{aligned} \quad (5.15)$$

where $Z_0 = 120\pi$ ohms, $d\Omega = \sin\theta d\theta d\phi$ is the differential solid angle, and the integration is over the main beam. The square matrix B has elements B_{mn}

where

$$B_{mn} = \frac{1}{Z_0} \iint_{\text{beam}} E_m^{\text{ref}}(\theta, \phi) [E_n^{\text{ref}}(\theta, \phi)]^* d\Omega \quad (5.16)$$

The power radiated by the feed cluster may be calculated by integrating over the primary pattern of the feed cluster or by integrating the secondary pattern over all space. These two

integrals are roughly but not exactly equal [35]. For the purpose of this thesis the integral over the secondary pattern at infinity, which is more valid, is used. This power is given by

$$P_{\text{feed}} = \sum_{m=1}^N \sum_{n=1}^N J_m^* J_n A_{mn} = (\mathbf{J}^*)^T \bar{\mathbf{A}} \mathbf{J} \quad (5.17)$$

where

$$A_{mn} = \frac{1}{Z_0} \int \int_{\text{space}} E_m^{\text{ref}}(\theta, \phi) [E_n^{\text{ref}}(\theta, \phi)]^* d\Omega \quad (5.18)$$

The ratio of (5.14) to (5.16) is

$$\text{Beam eff.} = \eta = \frac{P_{\text{beam}}}{P_{\text{feed}}} = \frac{(\mathbf{J}^*)^T \bar{\mathbf{B}} \mathbf{J}}{(\mathbf{J}^*)^T \bar{\mathbf{A}} \mathbf{J}} \quad (5.19)$$

It is now desired to find the \mathbf{J} that optimizes the beam efficiency.

5.4.3. Optimization of beam efficiency

Given Hermitian matrices \mathbf{A} and \mathbf{B} , we wish to maximize η in (5.19). It is well-known that \mathbf{A} can be diagonalized in the fashion

$$\bar{\mathbf{U}}^{-1} \bar{\mathbf{A}} \bar{\mathbf{U}} = \bar{\mathbf{D}} \quad (5.20)$$

where

$\bar{\mathbf{U}}$ = a unitary matrix formed by $\mathbf{U}_1, \mathbf{U}_2, \dots, \mathbf{U}_N$,

α_n, \mathbf{U}_n = an eigenvalue and its corresponding eigenvector of \mathbf{A} ,

$\bar{\mathbf{D}}$ = diagonal matrix with diagonal elements $d_{nn} = \alpha_n$.

Substitute

$$\bar{\mathbf{A}} = (\bar{\mathbf{C}}^*)^T \bar{\mathbf{C}}, \quad \text{where } \bar{\mathbf{C}} = \bar{\mathbf{D}}^{\frac{1}{2}} \bar{\mathbf{U}}^{-1} \quad (5.21)$$

where use is made of the fact that $\bar{\mathbf{U}}^{*T} = \bar{\mathbf{U}}^{-1}$. Introduce a new unknown \mathbf{K} in terms of the unknown \mathbf{J} ,

$$\mathbf{K} = \bar{\bar{\mathbf{C}}} \mathbf{J} = \bar{\bar{\mathbf{D}}}^{\frac{1}{2}} \bar{\bar{\mathbf{U}}}^{-1} \mathbf{J}. \quad (5.22)$$

Then (5.19) can be written as

$$\eta = \frac{\mathbf{K}^{*T} \bar{\bar{\mathbf{F}}} \mathbf{K}}{\mathbf{K}^{*T} \mathbf{K}} \quad (5.23)$$

where

$$\bar{\bar{\mathbf{F}}} = \bar{\bar{\mathbf{D}}}^{\frac{1}{2}} \bar{\bar{\mathbf{U}}}^{-1} \bar{\bar{\mathbf{B}}} \bar{\bar{\mathbf{U}}}^{\frac{1}{2}} \quad (5.24)$$

Equation (5.22) is the Raleigh quotient in the matrix theory [37]. The maximum value of η is

$$\eta = \lambda_{\max}, \quad (5.25a)$$

which occurs when

$$\mathbf{K} = \mathbf{V}_{\max}. \quad (5.25b)$$

Here, λ_{\max} is the maximum eigenvalue of $\bar{\bar{\mathbf{F}}}$, and \mathbf{V}_{\max} is the corresponding eigenvector.

From the relation

$$\bar{\bar{\mathbf{F}}} \mathbf{V}_{\max} = \lambda_{\max} \mathbf{V}_{\max} \quad (5.26)$$

and (5.23), it can be shown that

$$\bar{\bar{\mathbf{A}}}^{-1} \bar{\bar{\mathbf{B}}} \mathbf{W}_{\max} = \lambda_{\max} \mathbf{W}_{\max} \quad (5.27)$$

where

$$\mathbf{W}_{\max} = \bar{\bar{\mathbf{U}}} \bar{\bar{\mathbf{D}}}^{-\frac{1}{2}} \mathbf{V}_{\max} \quad (5.28)$$

Next the solution of \mathbf{J} that maximizes η is desired. From (5.21), (5.24), and (5.27), we obtain

$$\mathbf{J} = \bar{\bar{\mathbf{U}}} \bar{\bar{\mathbf{U}}}^{*T} \mathbf{W}_{\max} = \mathbf{W}_{\max} \quad (5.29)$$

In conclusion, given a feed element cluster with a known geometry, the maximum achievable beam efficiency η is obtained by using the element excitations (within a scaling constant) contained in \mathbf{J} in (5.28), which depends on the element pattern matrices in (5.16) and (5.18).

5.5. Results and Discussion

5.5.1. Power as a function of sidelobes

It is of interest to know what percentage of power is located inside a certain number of sidelobes. For example, if 99% of the far-field power is within the first three sidelobes for a given far-field pattern, then the integral over the secondary pattern to determine this power need only cover the solid angle covering the first three or four sidelobes. For the ideal pattern described in Section 5.3, the integral is closed form (5.9) and the enclosed power can be readily found. The power inside the first, second, and third nulls as a function of the aperture edge taper is shown in Figure 5.8. This indicates that for patterns with high edge tapers, the total radiated far-field power can be approximated by integrating over the cone containing the main beam and first three sidelobes.

5.5.2. Efficiency of reflector antennas

The results in Figure 5.8 for the ideal aperture distribution do not show the dependence on antenna geometry and feed pattern. In order to study the efficiency of a reflector antenna, the actual pattern must be used instead of the idealized pattern in (5.10). It is interesting to observe that, for a reflector antenna, high efficiency is achieved by severe "underillumination." By underillumination, we mean that both the main beam and part of the first sidelobe of the feed pattern are intercepted by the main reflector. This point will be explained further in Section 5.5.3.

5.5.3. Dependence of beam efficiency on feed size

Consider a parabolic reflector fed by a single circular waveguide with the following parameters:

Reflector diameter = $D = 1,000 \lambda$

f/D ratio: $f/D = 1.0$ and $f/D = 0.4$

Feed: TE₁₁ mode of a circular waveguide with diameter $2a$ at the focal point

We consider the cases:

Case 1: Symmetric reflector

Case 2: Offset reflector (lower edge of reflector is on the parabolic axis)

The variation of beam efficiency with respect to feed radius is shown in Figure 5.9a for the symmetric case and in Figure 5.9b for the offset case. The corresponding results for directivity are shown in Figures 5.10a and 5.10b, and for edge taper in Figures 5.11a and 5.11b. It is interesting to note that

1. Optimum efficiency and optimum directivity do not coincide.
2. Near optimum efficiency occurs for edge tapers ≥ 20 dB but optimum efficiency occurs when the reflector is slightly "underilluminated" (i.e., the first null hits the reflector near its edge).

Optimum directivity occurs for a 12-15 dB edge taper.

5.5.4. Scanned beam

A single symmetric reflector with a single circular waveguide feed is used. The f/D ratio is 2.

Reflector diameter = $D = 1,000 \lambda$

Feed: TE₁₁ mode of a circular waveguide located at the focal point.

Two feed radii are examined. The information for them is given in Table 5.1.

Table 5.1. Information for scanned reflector antennas

Radius (λ)	Edge taper (dB)	$\theta_{\text{beam}} (2)$	$\theta_{\text{beam}} (4)$	Spillover loss (dB)
1.8	10	0.35°	0.36°	-0.85
2.2	20	0.36°	0.36°	-0.44

Scanning is accomplished by tilting the reflector. When the reflector is tilted by α° , the beam is scanned by angle $\theta_{\text{scan}} \approx 2\alpha$ (Fig. 5.12). This is known as the mirror effect and it more than doubles the maximum scanning ability of an antenna when compared to that of the usual method of shifting the feed and keeping the reflector fixed. The results are shown in Figure 5.13.

An f/D ratio of 2 is very large but large f/D ratios contribute to much better scanning results. As an example of this, a comparison of beam efficiencies is made between the 2.2λ case above and a third case. This case uses a $1,000\lambda$ reflector with $f/D = 0.4$. A feed radius $= 0.7\lambda$ is used to maximize the on-axis beam efficiency. The nominal half-cone angle is $\theta_{\text{beam}} = 0.36^\circ$ (5.4) and the first null is at $\theta_{\text{beam}} = 0.44^\circ$ (5.2). The spillover loss is very low (-0.16 dB) and results in a very high on-axis beam efficiency of 94.7%. However, even for small scans, the antenna with the higher f/D ratio has a much higher beam efficiency (Fig. 5.14).

5.5.5. Cluster feed

A single symmetric reflector is used. The f/D ratio is 0.4.

Reflector diameter $= 2a = 1,000\lambda$

Feed: Seven-element hexagonal cluster of circular waveguides excited by the TE₁₁ mode. The feed radius is 0.7λ . Cluster is centered at the focal point. Element spacing is 1.42λ .

Spillover loss $= -0.16$ dB (on-axis with only the center element lit)

The excitations of the feed elements are chosen as above to maximize beam efficiency. In Figure 5.15, results for scanning by an optimized seven-element hexagonal cluster feed (ring of six elements surrounding one element) are compared to those for an antenna with a single element of the same type as those used in the cluster feed. The feed element size is chosen so that beam efficiency is optimized for a single element in the unscanned case. For this reason, at small scan angles the optimal result comes from using very small excitations

on the outer elements; as a result, the improvement is small. The improvement due to using the more complex cluster feed is more evident for wider scans. In this case, the efficiency improved by over 10% for some scan angles.

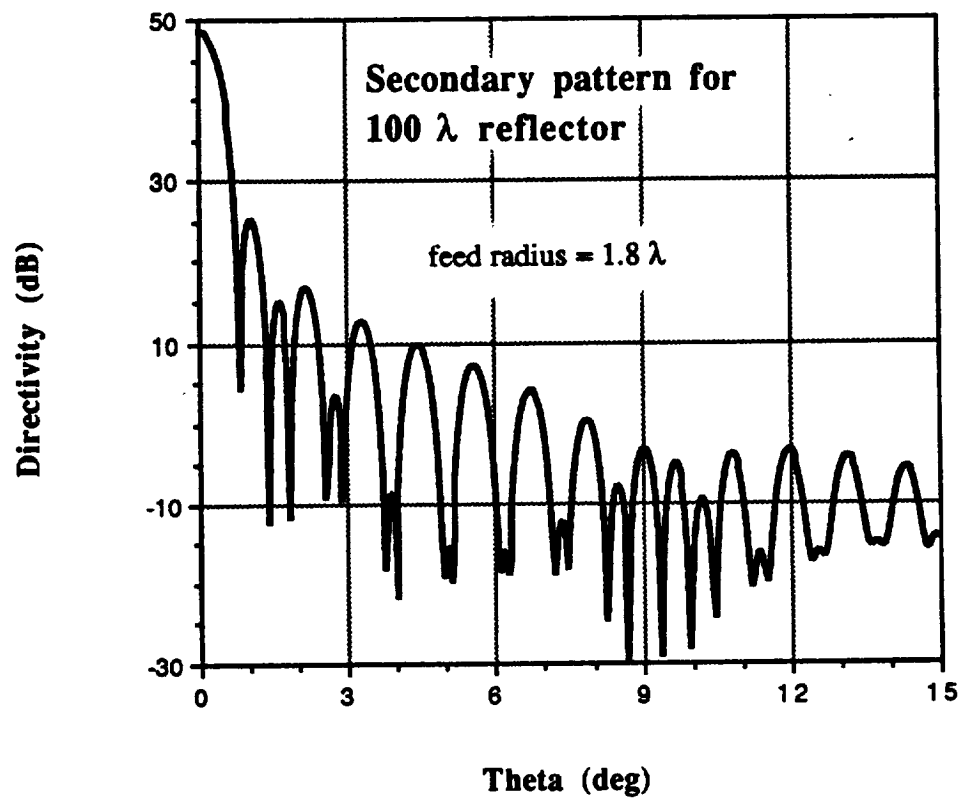


Figure 5.1. Secondary pattern for reflector antenna with $f/D = 2.0$ and a 10 dB edge taper. The feed is an open-ended circular waveguide of radius 1.8λ excited by the TE_{11} mode.

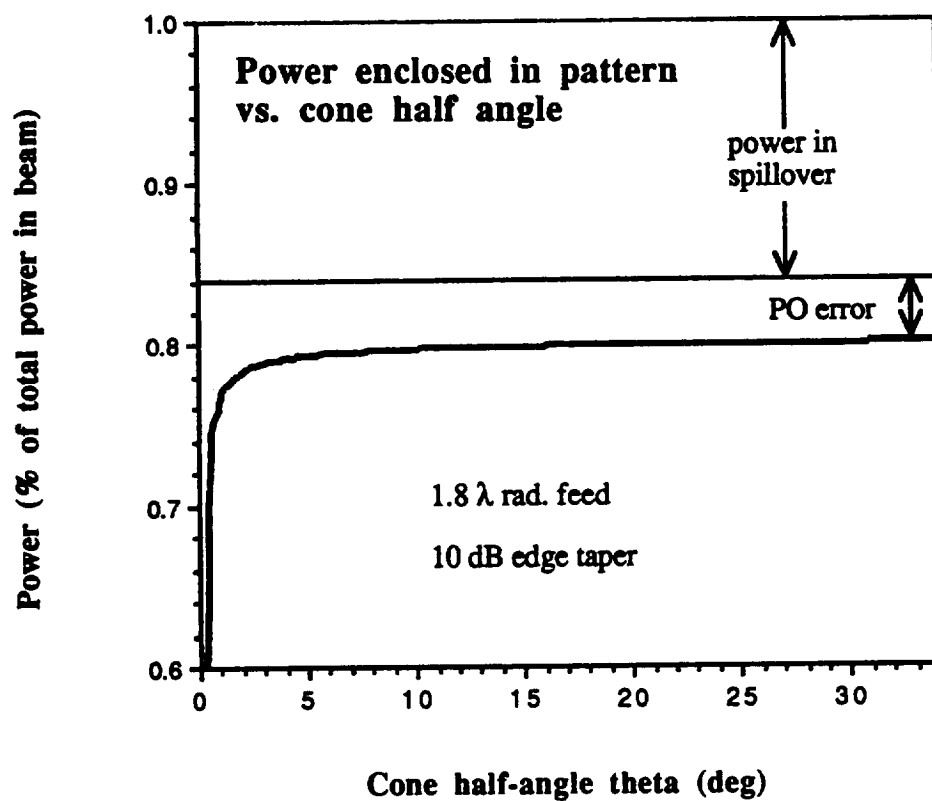


Figure 5.2. Power enclosed in the secondary pattern as a function of cone-angle. The discrepancy between the enclosed power and the spillover loss is the PO error.

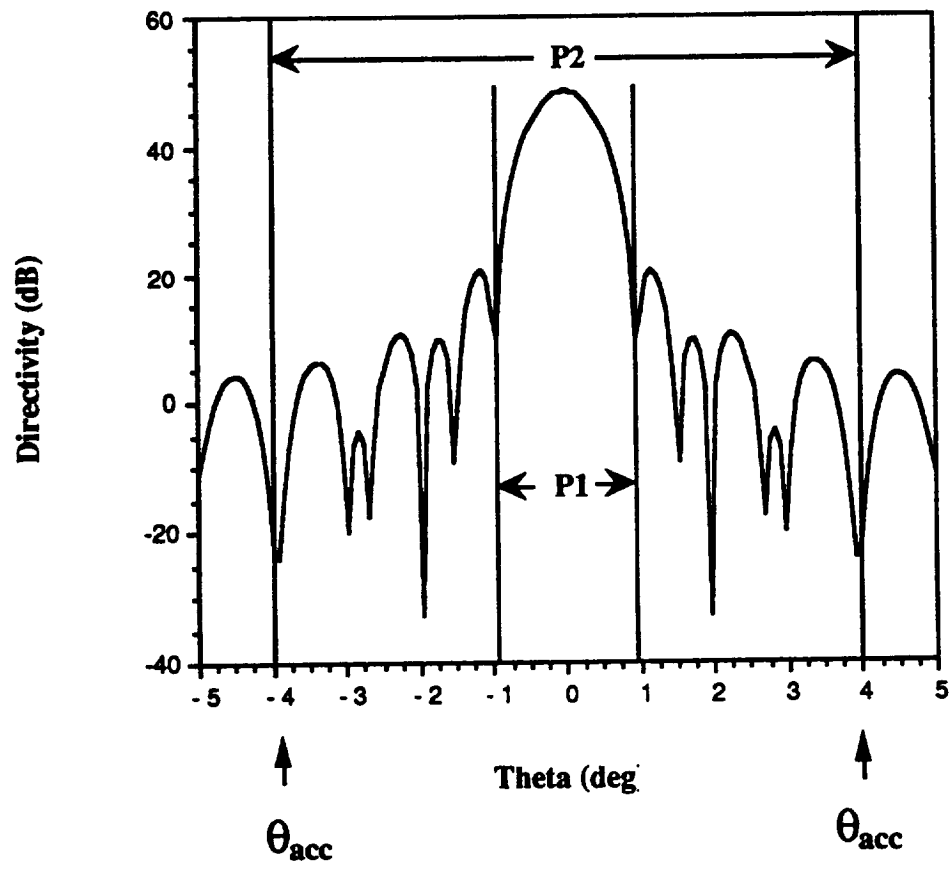


Figure 5.3. The pattern efficiency as defined in (5.7).

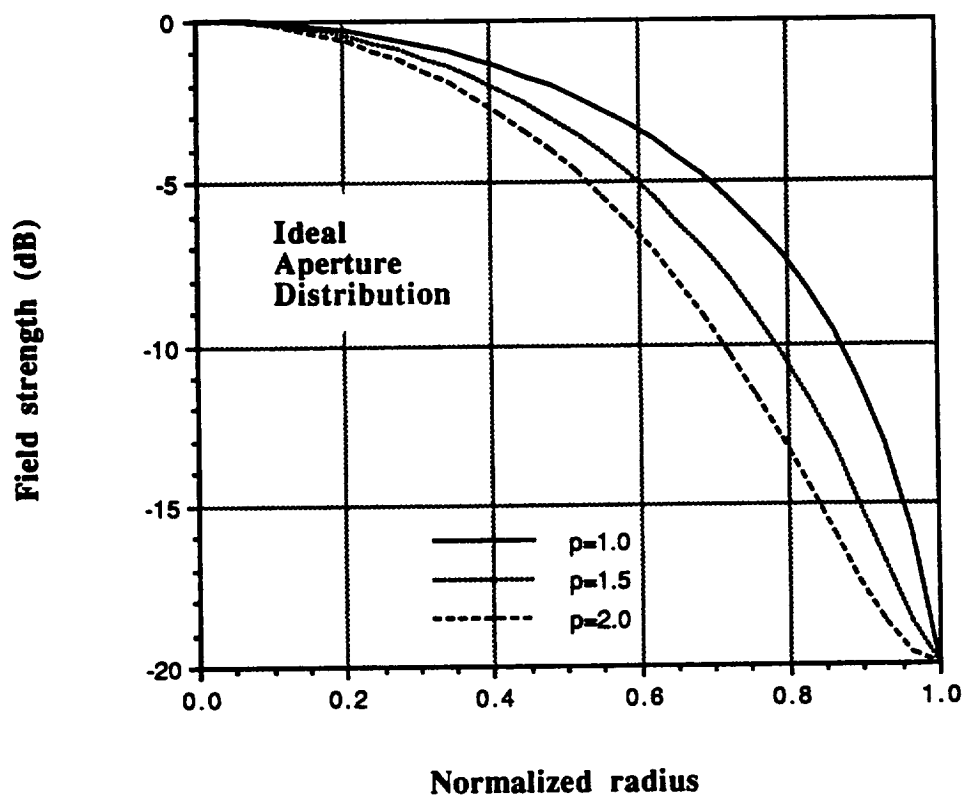


Figure 5.4. Aperture distribution for the ideal feed pattern (5.8) with a 20 dB edge taper ($\bar{C} = 0.1$) and various values of p .

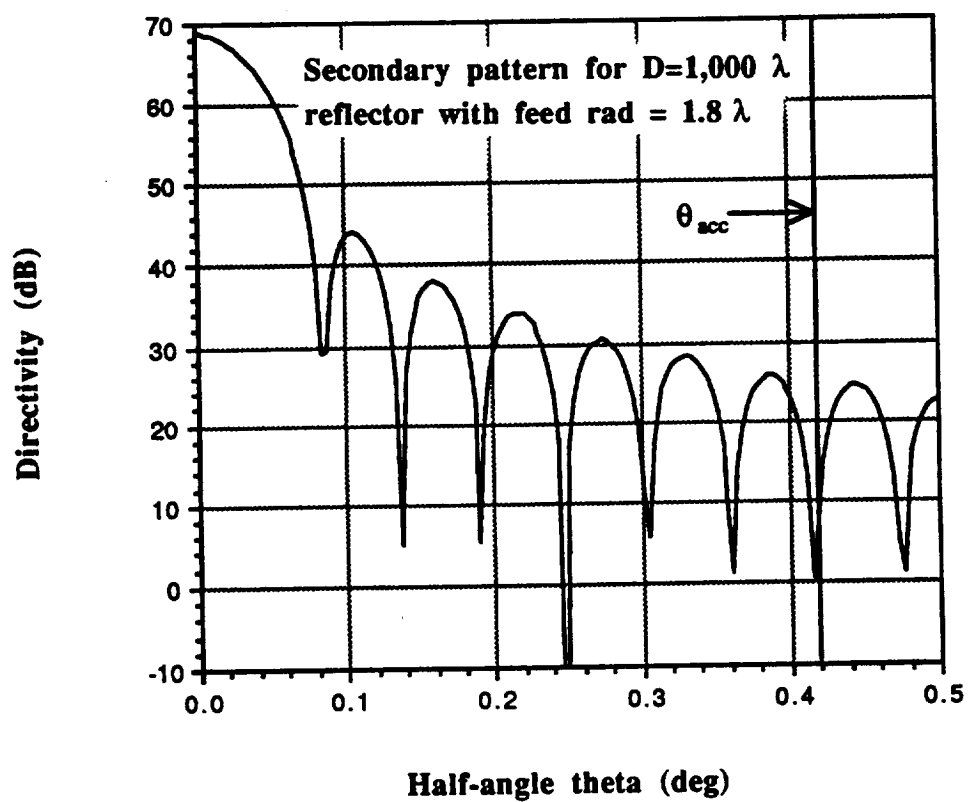


Figure 5.5. Secondary pattern with the region of accuracy, bounded by θ_{acc} , shown.

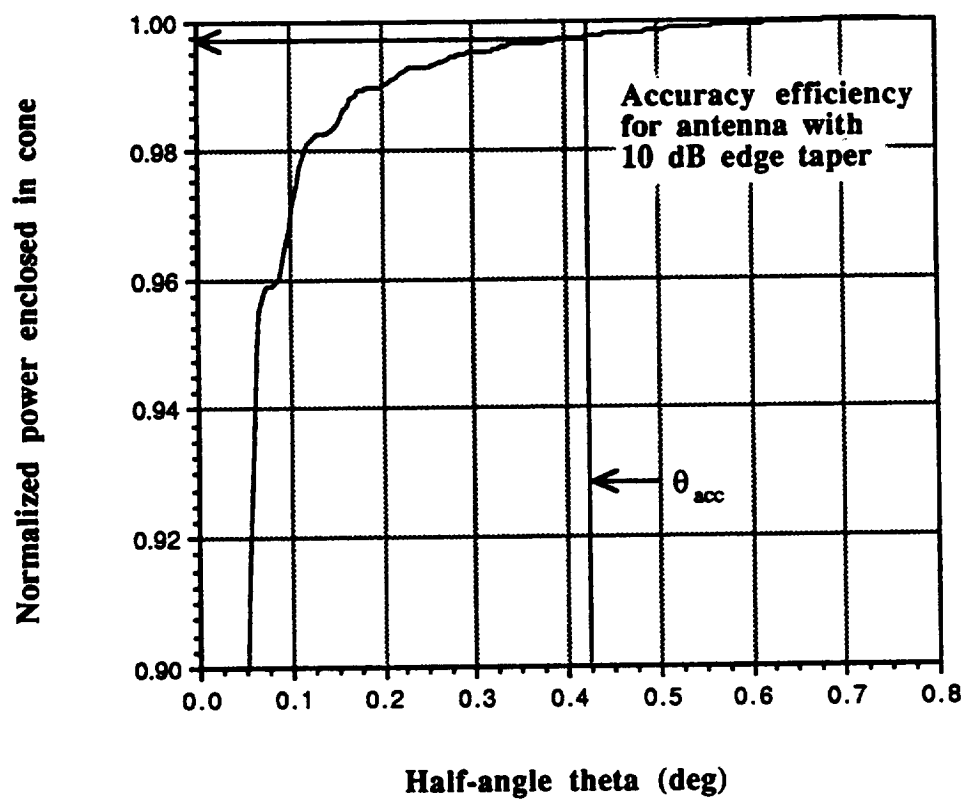


Figure 5.6. Power enclosed, as a function of the cone angle. Almost all of the power in the far-field pattern is in the region of accuracy.

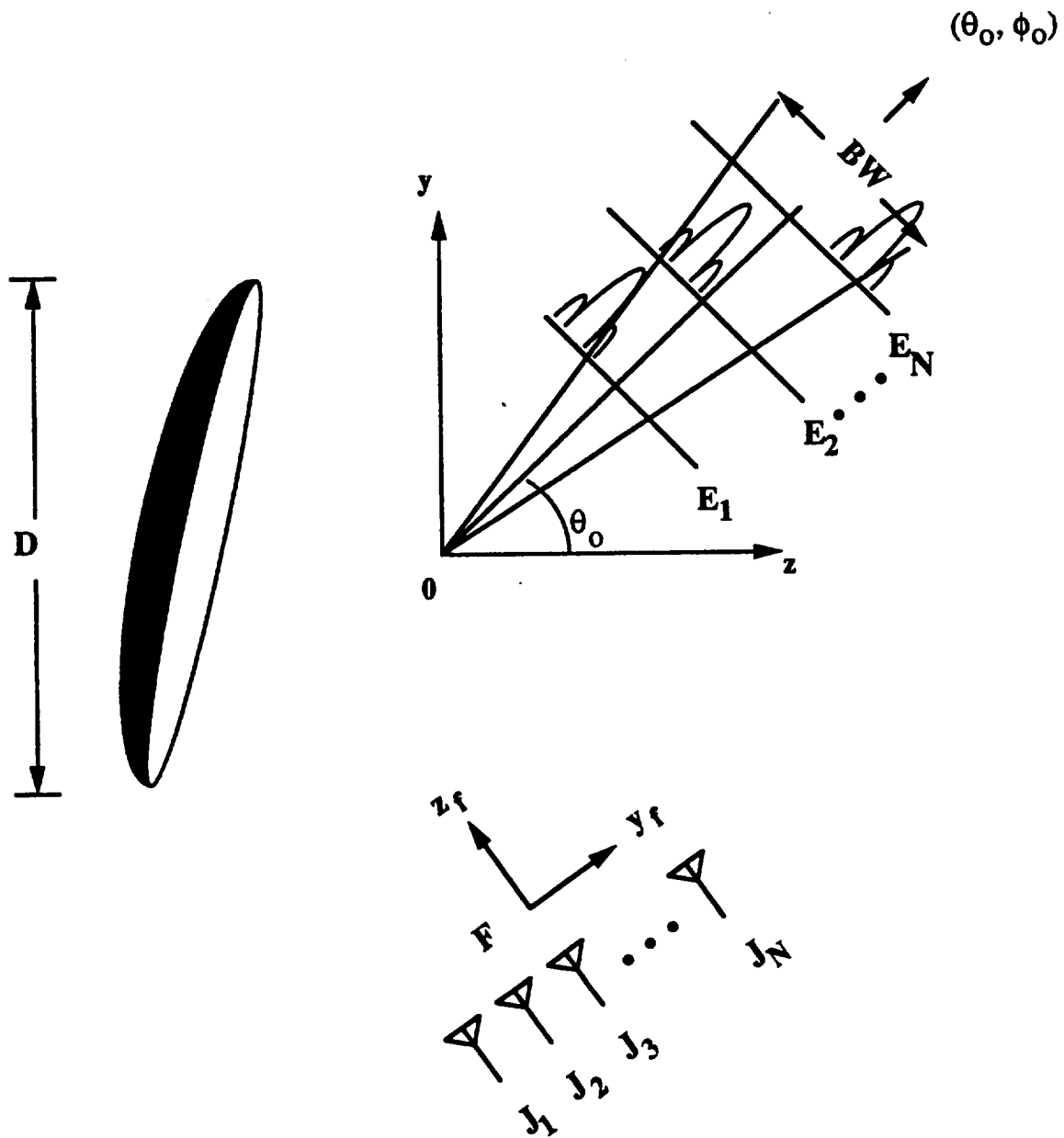


Figure 5.7. A reflector antenna with a feed cluster. The secondary pattern due to the excitation of element 2 ($J_2 = 1$ and all other $J_n = 0$) is E_2 .

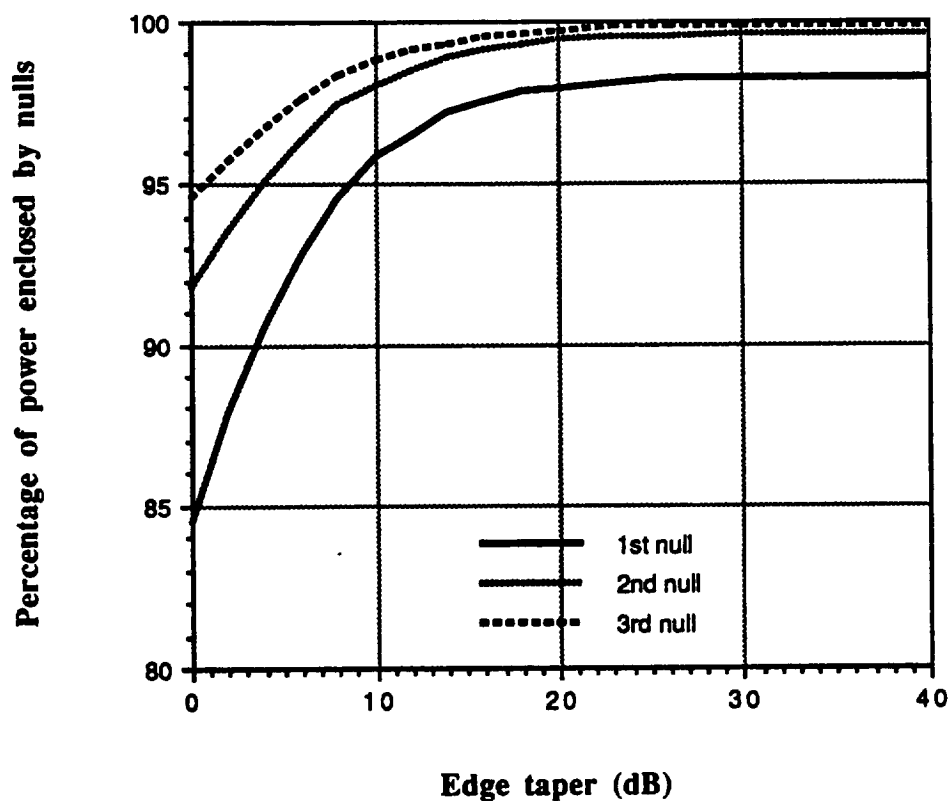


Figure 5.8. Power enclosed within the main beam and first two sidelobes for the ideal aperture distribution given in (5.10). The power is shown as a function of the edge taper of the feed aperture distribution. Note that the curves level out for edge tapers greater than 20 dB.

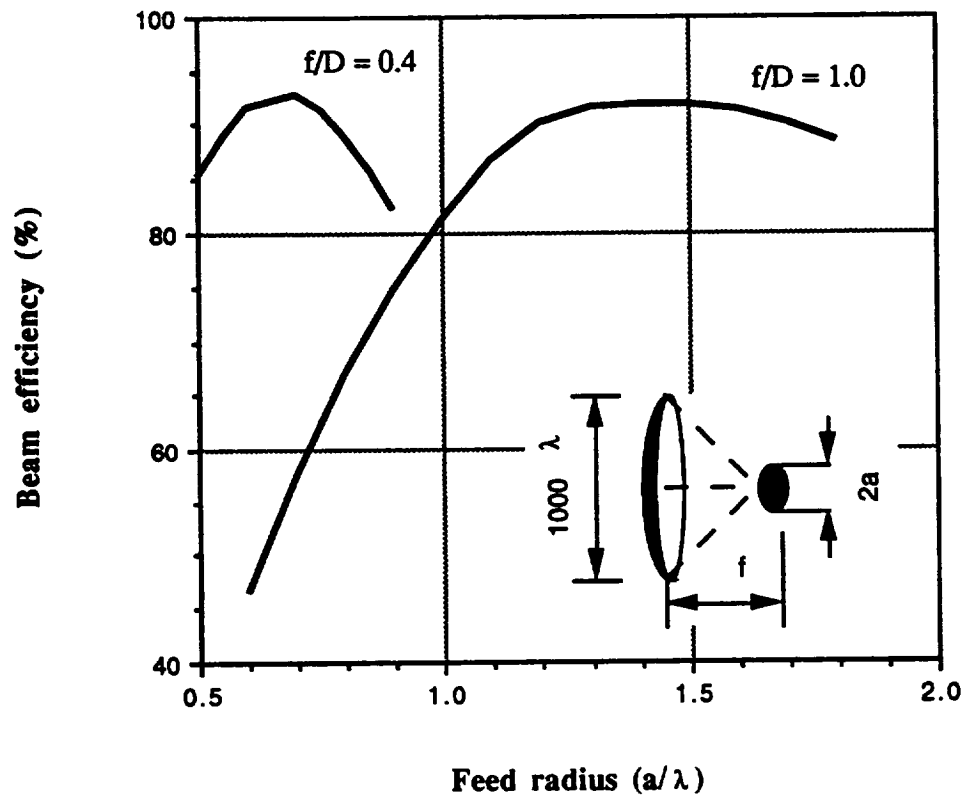


Figure 5.9a. Variation of beam efficiency (using definition in (5.4)) with feed radius for a symmetrical antenna with various f/D s. The feed is an open-ended circular waveguide.

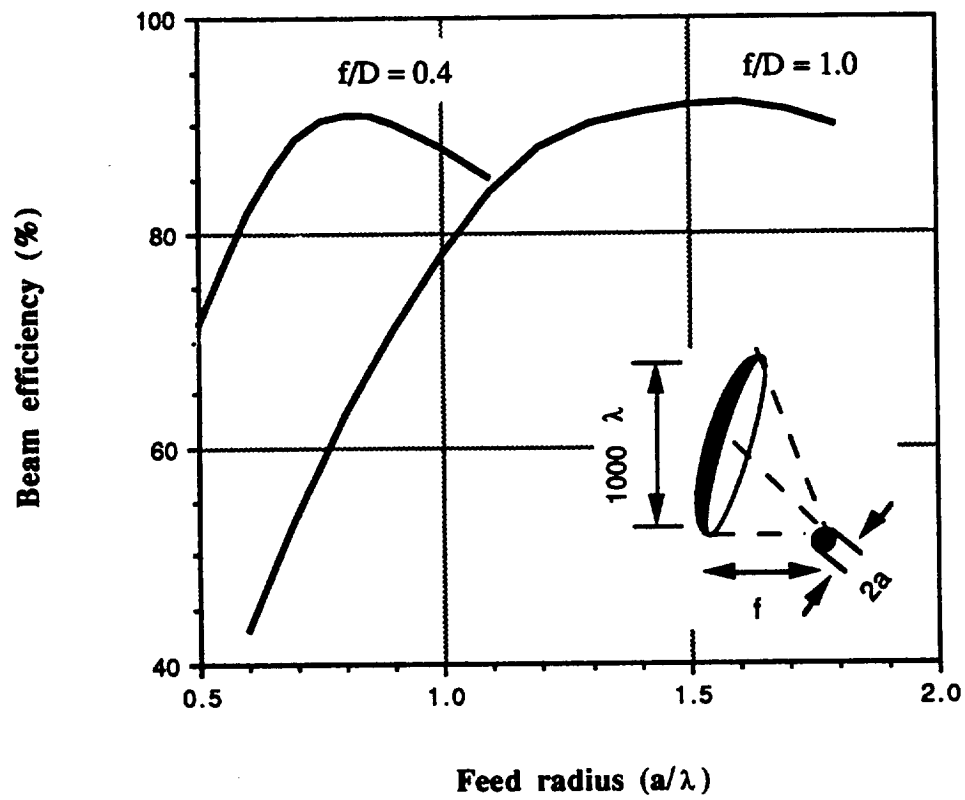


Figure 5.9b. Variation of beam efficiency (using definition in (5.4)) with feed radius for an offset antenna with various f/D s. The feed is an open-ended circular waveguide.

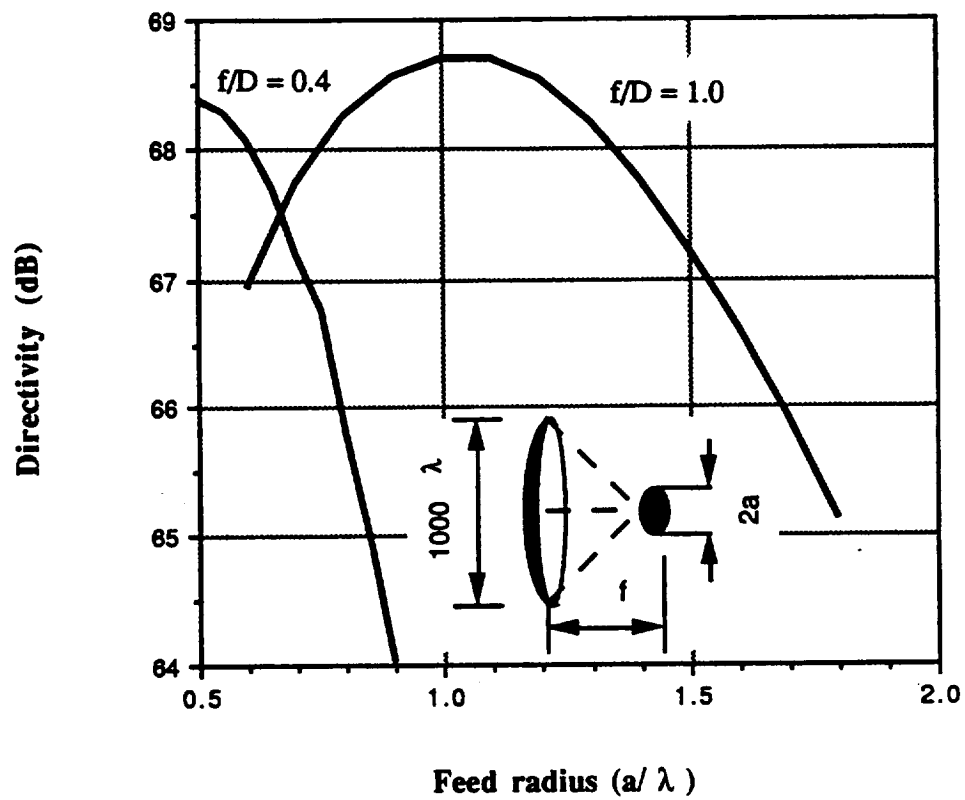


Figure 5.10a. Variation of directivity with feed radius for a symmetrical antenna with various f/D s. The feed is an open-ended circular waveguide.

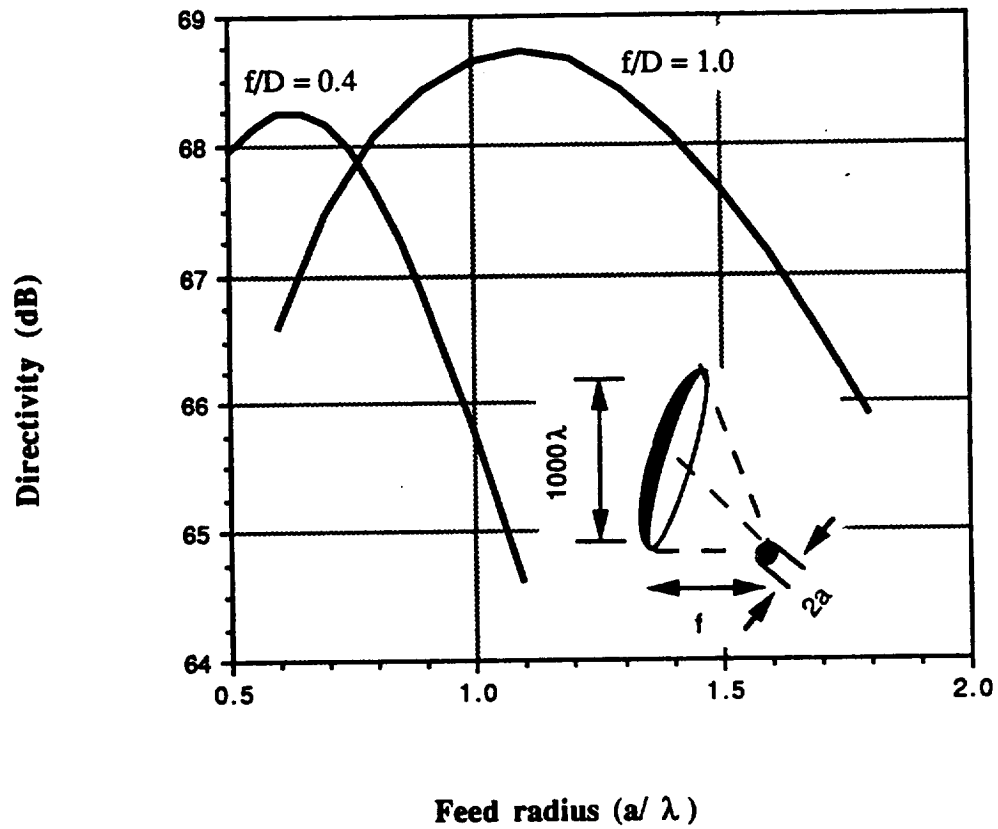


Figure 5.10b. Variation of directivity with feed radius for an offset antenna with various f/D s. The feed is an open-ended circular waveguide.

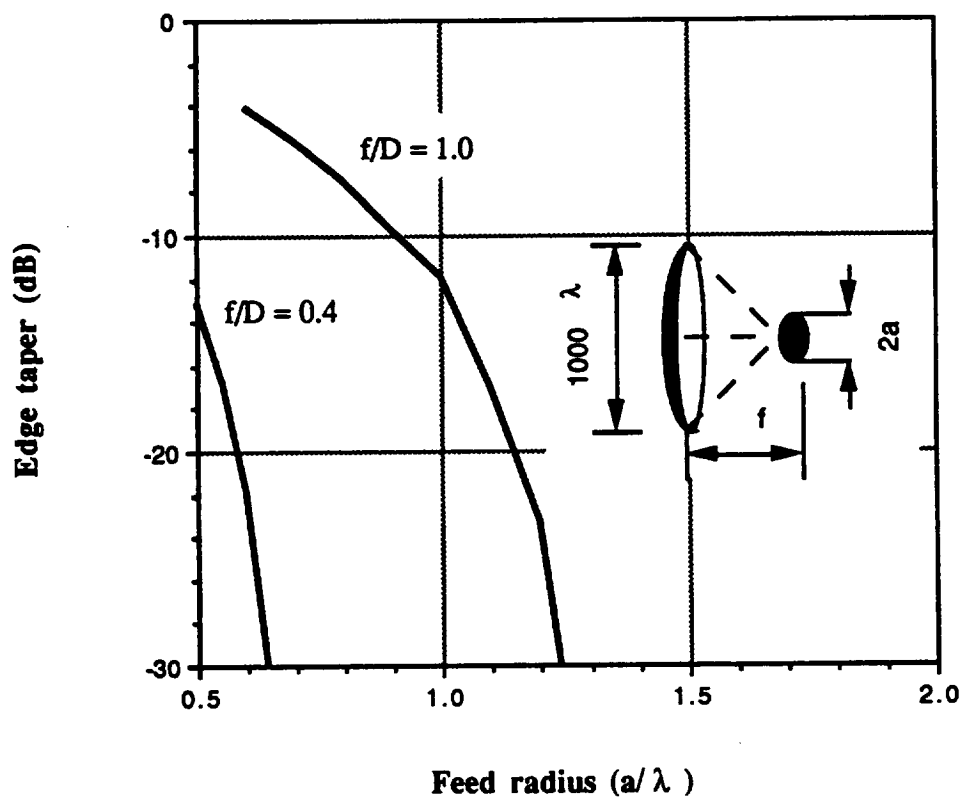


Figure 5.11a. Variation of edge taper with feed radius for a symmetric antenna with various f/D s. The feed is an open-ended circular waveguide (cutoff occurs if the radius is roughly less than 0.4λ).

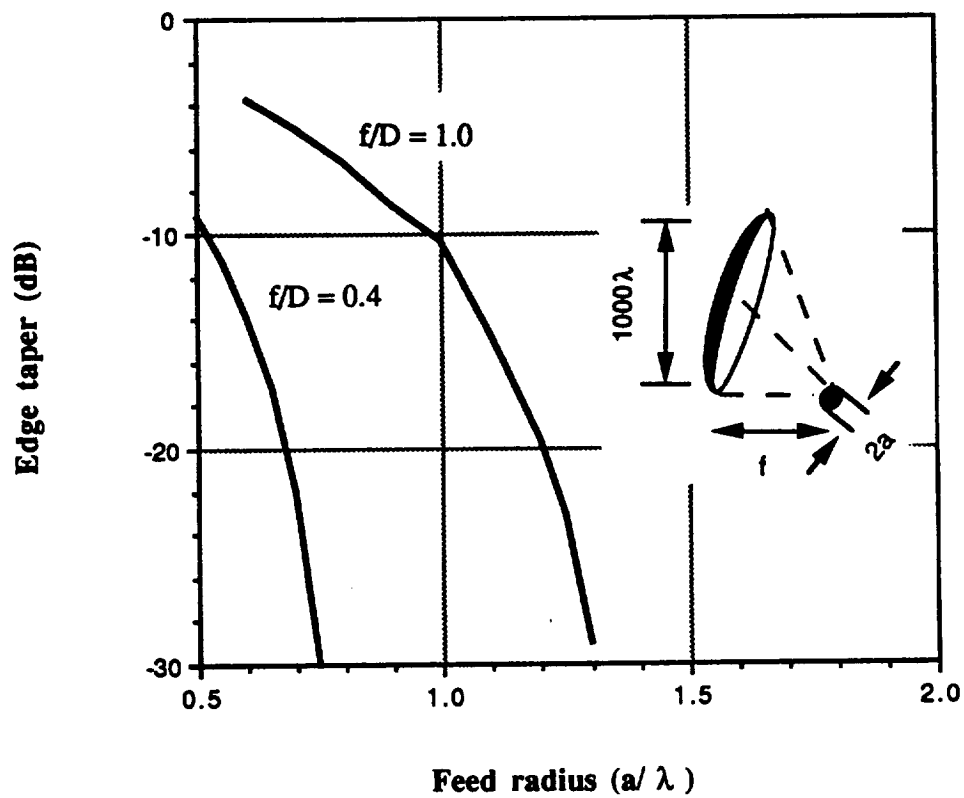


Figure 5.11b. Variation of edge taper with feed radius for a symmetric antenna with various f/D s. The feed is an open-ended circular waveguide (cutoff occurs if the radius is roughly less than 0.4λ).

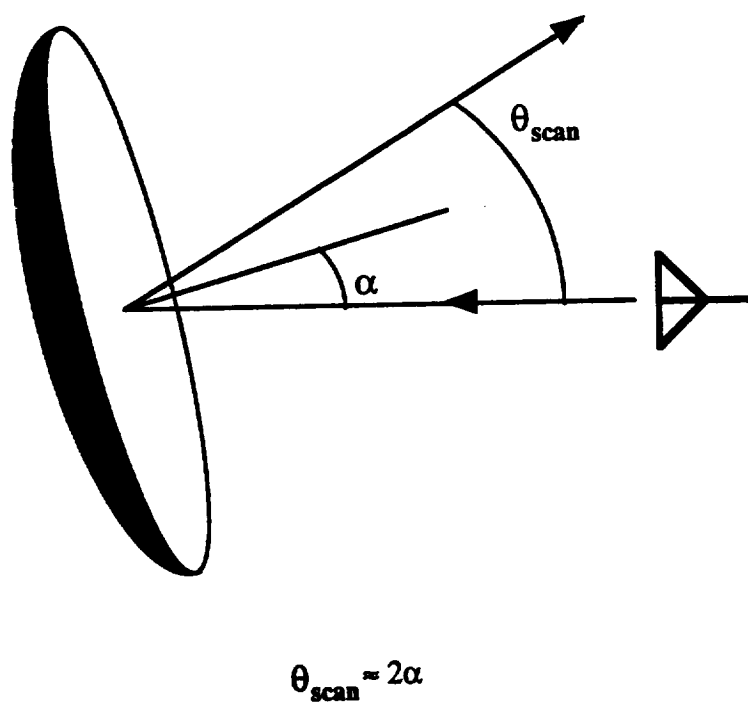


Figure 5.12. The beam is scanned by tilting the reflector and keeping the feed fixed.

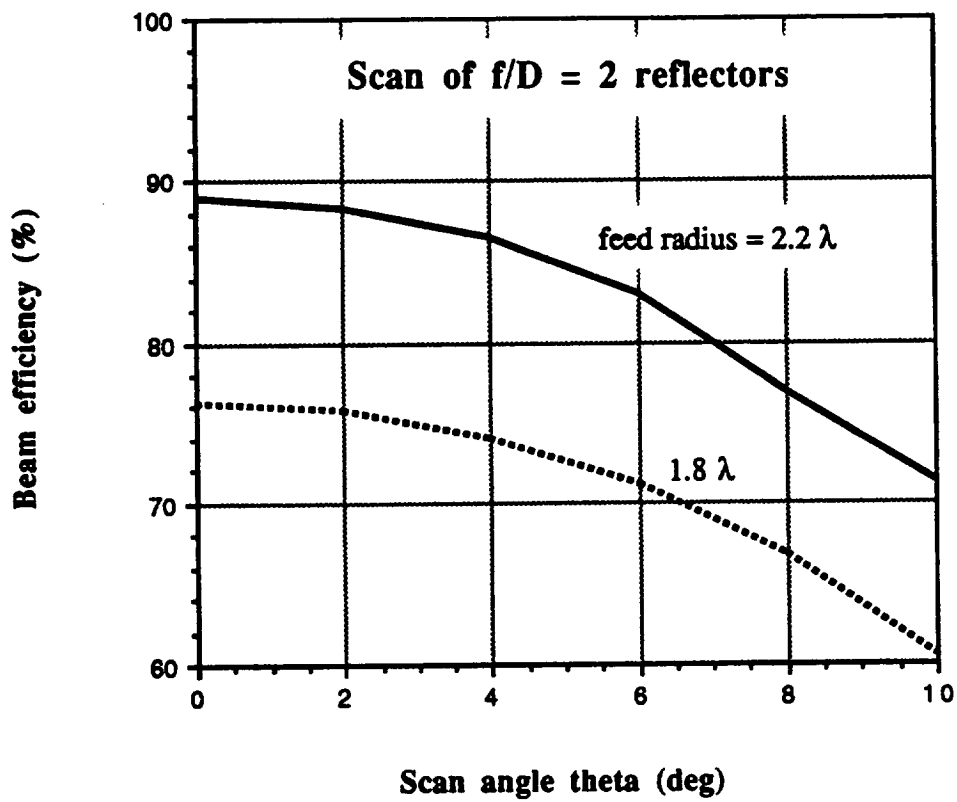


Figure 5.13. Comparison of scanning ability for two antennas with different sized feeds (single open-ended waveguide excited by TE₁₁ mode).

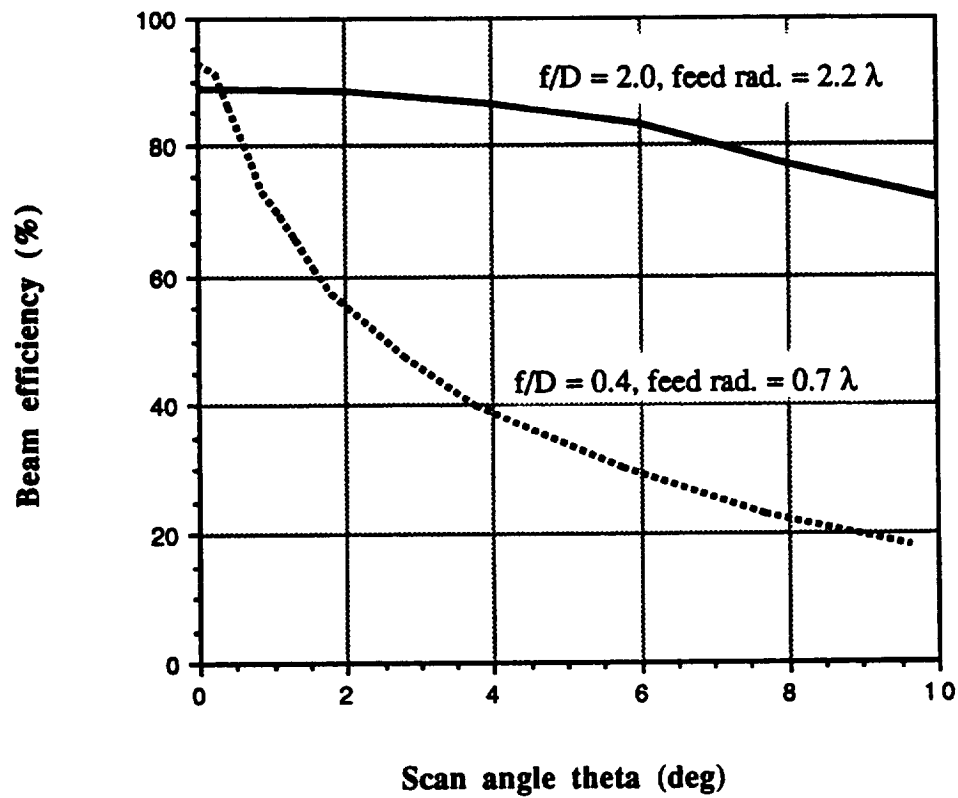


Figure 5.14. Comparison of scan-loss results for antennas with different f/D ratios. A large f/D ratio allows much better scanning. The feed is a single open-ended circular waveguide excited by the TE_{11} mode.

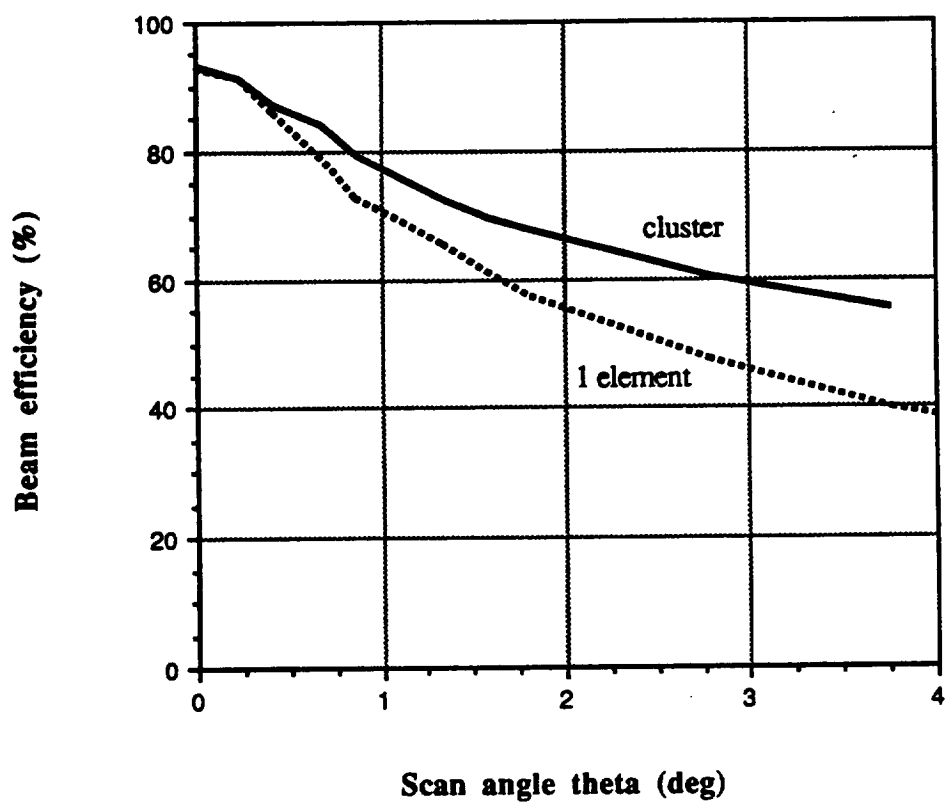


Figure 5.15. Comparison showing the improvement obtainable by use of a cluster feed with feed excitations optimized for beam efficiency. The antennas have $f/D = 0.4$ and all feed elements are open-ended waveguides with radius $= 0.7 \lambda$. The cluster feed used seven elements in a hexagonal arrangement (six around one) with center-to-center spacing $= 1.42 \lambda$.

6. USE OF FREQUENCY SELECTIVE SURFACES IN REFLECTOR ANTENNA DESIGN

Frequency selective surfaces (FSS) are very valuable for the design of multiband reflector antennas. In a standard antenna design, it is desired to place the phase center of the feed at the focal point of the main reflector. However, in multiband applications it is often necessary to use more than one feed. In this case the feeds must be kept physically separate. This can be achieved by placing one or more of the feeds at an image point of the focal point. This is often done in dual reflector configurations, such as cassegrainian or gregorian. In a cassegrainian configuration, the subreflector is located between the main reflector and its focal point (Fig. 6.1). An additional feed could be placed at the focal point of the main reflector, but its energy would be blocked by the subreflector. This problem is avoided if the subreflector is transparent to the energy emitted behind it, but reflects the energy emitted from the cassegrainian feed. This effect can be achieved with use of an FSS. In this chapter, the use of FSS in the design of the ATDRSS triband reflector antenna is examined.

6.1. The ATDRSS Project

NASA's Tracking and Data Relay Satellite System (TDRSS) presently provides a vital link in space communications. The TDRSS satellites substantially increase earth-to-space link availability and provide a near continuous exchange of information. A single TDRSS satellite can transmit and receive high-data-rate information to and from low earth orbiting spacecraft via two single access (SA) reflector antennas. These steerable SA antennas can provide simultaneous S-band and Ku-band communications with one spacecraft at a time. Communications to and from orbiting spacecraft can also be accomplished via an S-band multiple access phased array antenna, though at much lower data rates. A separate space-to-ground link antenna operating at Ku-band provides

communications between a TDRSS satellite and the TDRSS White Sands Ground Terminal in New Mexico.

In order to provide additional bandwidth for increased communications demand, the advanced TDRSS, or ATDRSS, project has been proposed and is scheduled for launch in 1997. As conceived, the ATDRSS satellites will incorporate Ka-band capability in the SA reflector antennas, in addition to the S-band and Ku-band services. Therefore, in order to meet these future requirements, the development of a triband reflector antenna for ATDRSS is critical.

6.2. Design

There are two approaches to designing a triband reflector antenna. Both approaches use a single-band feed for S-band and isolate the S-band from the other two bands by means of a frequency selective surface (FSS). In the first approach a multiband feed (usually a corrugated horn) is used. In the second approach two single-band feeds are used which are isolated from each other by means of a second FSS. Both approaches have pluses and minuses. The multiband feed is more compact and avoids additional FSS losses [38-40]. However, design of a multiband feed is much more difficult than that of a single-band feed. It is more difficult to optimize parameters such as feed size and taper. Performance will further degrade if the phase centers of the two bands do not coincide. In contrast, the horn design for the second approach is much easier and feed losses will be lower. The design will not be as compact since there is an extra feed and FSS. The challenge is in designing a low-loss FSS. The task is made more challenging by the relatively small separation (about 2:1) between the Ka-band and Ku-band. FSSs are today typically used to discriminate between bands with a 6:1 ratio (for example between S-band and Ku-band).

In this thesis, we have chosen the second approach, in which three separate feeds are used. It is felt that the improvement in feed performance will not be offset by the higher

FSS losses. It is also easier to analyze the feed system in the second approach since the design of the multiband feed is to some extent a hardware design problem. Each feed is optimized for a single band and the feeds are isolated by means of frequency selective surfaces (FSS). The FSS will transmit certain frequencies while reflecting others. Two reflector antenna configurations are presented below, an offset single reflector (Figs. 6.2, 6.3) and a symmetric shaped dual reflector (Figs. 6.4, 6.5). The advantages of each design are presented in Table 6.1.

Table 6.1. Design summary

Main reflector	FSS	Advantages
parabolic, offset Fig. 6.1	2 planar	planar FSS only smaller diameter main reflector (12.5 ft.) solid reflector, not mesh
shaped, symmetrical Fig. 6.3	1 planar and 1 curved	smaller volume (shorter focal length) similar to existing TDRSS design

6.2.1. FSS design

Planar FSSs have an advantage in that they can be theoretically analyzed by methods such as Floquet modes. Curved FSSs must be analyzed as being locally flat. The initial design is then tested to observe the perturbation caused by the curvature. Several iterations are then usually necessary to completely compensate for the effects of the curvature.

FSS designs have been developed that will provide the necessary transmission and reflection characteristics. The FSSs use ring elements, due to the circular polarization of the radiated field. A total of four FSSs were designed. FSS1 and FSS2 are used in the

offset configuration. FSS3 and FSS4 are used in the symmetric configuration. A breakdown of the requirements for each surface is shown in Table 6.2.

Table 6.2. FSS requirements

FSS	S-band	Ku-band	Ka-band
1	transmit	---	reflect
2	transmit	reflect	transmit
3	transmit	reflect	reflect
4	---	transmit	reflect

FSS3 is the only curved surface, being the subreflector of the dual cassegrainian design. Using these designs, far-field patterns have been computed for the above antenna systems, including losses due to the FSS effects.

6.2.2. Offset reflector

The offset configuration uses a reflector with a diameter of 150", a focal length of 130", and an offset height of 15". Both FSSs are planar. FSS1 is farther from the reflector and is orientated vertically (Fig. 6.3). This surface uses Arlon D1CLAD880 that is 15 mil thick and has a dielectric constant $\epsilon = 2.17 - j0.0017$. The lattice angle is 60° (as it is for all four FSSs); the dimensions for the ring elements are shown in Figure 6.4. FSS2 is tilted 5° from vertical. The substrate is Arlon D1CLAD880 but the thickness is 30 mil. The dimensions of the ring elements are shown in Figure 6.5. All feeds are assumed to be corrugated circular horns. The S-band feed has $D = 10"$ (1.8λ at 2.2 GHz), the Ku-band has $D = 1.6"$ (2.0λ at 14.9 GHz), and the Ka-band feed has $D = 0.94"$ (2.0λ at 25.25 GHz).

6.2.3. Symmetric reflector

The symmetric configuration uses a cassegrainian subreflector. The main reflector has $D = 168''$ and a hole at the vertex $28''$ in diameter. The subreflector has $D = 28''$. The subreflector is shaped to avoid sending energy into the hole in the main reflector. The main reflector is shaped to avoid energy blockage by the subreflector (Fig. 6.6). This shaping is subtle and at S-band frequencies the main reflector and subreflector appear to be parabolic and hyperbolic in shape respectively. The Ku-band and Ka-band feed structures are inside the shadow cast by the subreflector on the main reflector so that feed blockage losses will be minimal (Fig. 6.7). The S-band feed is located at the focal point of the main reflector. At S-band the main reflector can be considered to be parabolic because the deviation due to shaping is only a fraction of a wavelength. This feed is a crossed dipole with $4.4''$ diameter subreflector. The Ku-band and Ka-band feeds are corrugated circular horns that are $3.6''$ and $1.88''$ in diameter, respectively. These feeds are significantly larger than the corresponding feeds for the symmetrical case. The offset design has $f/D = 0.87$. For the dual reflector design, the distance from the feeds to the subreflector is about 1.5 times the diameter of the subreflector. Therefore, the Ku-band and Ka-band feeds for the dual design need to be more directive to maintain spillover losses comparable to those for the offset design. The subreflector is FSS3, transmitting at S-band and reflecting at the higher frequency bands. The substrate is Arlon D1CLAD810 with dielectric constant $\epsilon = 10.5 - j0.0158$ and thickness 14 mil. The dimensions of the periodic element are shown in Figure 6.8. FSS4 is tilted 35° from vertical. The substrate is Arlon D1CLAD880 with a thickness of 200 mil. There are two layers with the rings facing inward towards each other. The separation between the layers is 84 mil and is also filled with D1CLAD880. The dimensions of the ring elements are shown in Figure 6.9.

6.2.4. Comparison of reflector size

Most Phase A designs for ATDRSS have proposed 16' diameter mesh main reflectors [41,42]. The large diameter compensates for blockage, feed losses, and RMS

errors which are higher for a mesh surface than for a solid surface. By combining high feed efficiency and a shaped reflector to lower blockage losses, the size of the reflector is reduced to 14' for our symmetric design. For the offset case, there is no blockage. An assumption of a solid surface reduces RMS surface losses. In this case a diameter of 12.5' is achievable while meeting link budget requirements. If the solid reflector is hinged to allow folding, then it is possible to fit a solid reflector of this size on the launch vehicle (Space Shuttle or Atlas-Centaur).

6.3. Results

A physical optics-based model for an open-ended circular waveguide is used as the feed. Physical optics is used to calculate the field incident on the reflector (or main reflector in the case of the dual reflector design). An FFT is then used to calculate the far-field pattern.

It is important to integrate the effects of the FSS into the reflector analysis, because the transmission and reflection coefficients of the FSS are a function of the incident angle of the radiation. The theta and phi components of the incident field interact differently with the FSS. Therefore, the incident wave must be broken down into its theta and phi components as defined in the FSS coordinate system. The local z-axis is chosen as being the normal to the surface at the point of intersection, and directed into the same half-plane as the global z-axis (Fig. 6.10). The reflected and transmitted fields are then related to the incident field via a matrix formulation.

$$\begin{aligned} \begin{bmatrix} H_t^\theta \\ H_t^\phi \end{bmatrix} &= \begin{bmatrix} t_1 & t_2 \\ t_3 & t_4 \end{bmatrix} \begin{bmatrix} H_i^\theta \\ H_i^\phi \end{bmatrix} \\ \text{and} \quad \begin{bmatrix} H_r^\theta \\ H_r^\phi \end{bmatrix} &= \begin{bmatrix} r_1 & r_2 \\ r_3 & r_4 \end{bmatrix} \begin{bmatrix} H_i^\theta \\ H_i^\phi \end{bmatrix} \end{aligned} \quad (6.1)$$

In the case of a transparent surface for transmission and a perfect electrical conductor (pec) surface for reflection, (6.1) reduces to

$$\begin{bmatrix} H_t^\theta \\ H_t^\phi \end{bmatrix} = \begin{bmatrix} 1 & 0 \\ 0 & 1 \end{bmatrix} \begin{bmatrix} H_i^\theta \\ H_i^\phi \end{bmatrix}$$

and

$$\begin{bmatrix} H_r^\theta \\ H_r^\phi \end{bmatrix} = \begin{bmatrix} -1 & 0 \\ 0 & 1 \end{bmatrix} \begin{bmatrix} H_i^\theta \\ H_i^\phi \end{bmatrix} \quad (6.2)$$

In the reflector system the energy spreads out as it leaves the feed. Therefore, it is incident on the FSS over a wide range of incident angles (Fig. 6.11). For example, in the offset configuration the energy from the Ka-band feed is incident on FSS1 at a range of incident angles of $6.6^\circ < \theta < 64.8^\circ$. The strength of the field also varies as a function of the angle from the feed axis. In addition, the losses due to phase shifting by the FSS must also be considered. These factors can not be adequately accounted for unless the FSS effects are integrated into the reflector system. In general, the FSS losses are less than 1 dB and are usually on the order of a few tenths of a dB. The most noticeable effect is reduction of the null in the cross-pol at boresight. However, in all cases the cross-pol is at least 20 dB below the ref-pol. The results for the two configurations are shown in Table 6.3. The FSS losses are shown in parentheses. TRW's estimated link budget requirements [43] are also shown for comparison.

Table 6.3. Directivity results

Band	Freq. (GHz)	Offset dir. (dB)	Symmetric dir. (dB)	Required (TRW est.) (dB)
S	2.2	37.2 (0.1)	37.7 (0.1)	36.0
Ku	13.7	---	54.6 (0.6)	51.0
Ku	14.9	54.0 (0.1)	55.4 (0.5)	51.0
Ka	25.25	58.7 (0.1)	60.2 (0.4)	54.0
Ka	27.5	58.8 (0.6)	60.3 (1.0)	54.0

The 2.2 GHz, 14.9 GHz, and 25.25 GHz frequencies are the center frequencies (the lower edge of the receive band) for the S, Ku and Ka bands, respectively. Results were computed for two additional frequencies where FSS losses were a maximum. For both designs, at the upper edge of the Ka band (27.5 GHz), increased FSS losses almost completely negated the increase in directivity resulting from using the same-size reflector at a higher frequency. For the symmetric design, FSS losses in the Ku band were highest at the lower band edge (13.7 GHz). In all other cases, the FSS losses at the band edges were lower than or roughly equal to losses at the center frequency. At every frequency, the offset design has lower directivity than the symmetric design, despite having lower FSS losses. This is due to the fact that the offset design uses a smaller reflector.

It should be noted that Table 6.3 does not give the complete picture. The computed directivities shown include spillover/illumination losses, blockage losses, and FSS losses. They do not include reflector surface losses, radome losses, feed losses, and feed line run losses. These losses are taken from published Phase A results [41-43]. When these additional losses are added, all link budget requirements are still satisfied. The gain margin (over TRW's Phase A report specifications [43]) is shown in Table 6.4. The margin is

Table 6.4. Antenna gain margin over TRW specifications

Band	Freq. (GHz)	Gain Margin (dB)	
		Offset	Symmetric
S	2.2	0.7	0.8
Ku	13.7	2.3	2.3
Ka	27.5	3.3	2.9

computed in each band for the frequency at which the margin is a minimum. This is 2.2 GHz for S-band and 27.5 GHz for the Ka-band. The actual Ka-band margin is actually

slightly lower, since the TRW Ka-band specification is for 25.25 GHz, not 27.5 GHz. For the Ku-band, the margin is computed at 14.9 GHz for the offset design and at 13.7 GHz for the symmetric design.

6.4. Physical Layout

The offset fed single reflector antenna configuration has been selected for integration into proposed ATDRSS designs. The offset design uses a solid reflector and planar FSSs, which can be accurately modeled by existing computer programs using modal analysis. The offset fed single access antenna geometry shown in Figure 6.2 has been adapted for a conceptual spacecraft design. Some of the assumptions for this design are (a) an Atlas Centaur launch vehicle, (b) an Advanced Communications Technology Satellite (ACTS) size spacecraft body and ACTS type solar arrays and (c) the S-band amplifier can be located in the spacecraft body and the Ku- and Ka-band equipment can be located in the antenna arms near the feed horns.

CADAM drawings have been completed for the design concept and a 1/13th scale model has been constructed, employing this offset-fed antenna configuration. Figure 6.12 is a photograph of the spacecraft model in the launch ready state. Figure 6.13 shows the spacecraft model with both offset fed antennas fully deployed and pointed north and south. This configuration allows for a full 360° offset antenna scanning capability. Lunar access, which has been recently added to the ATDRSS mission, is achievable with this configuration.

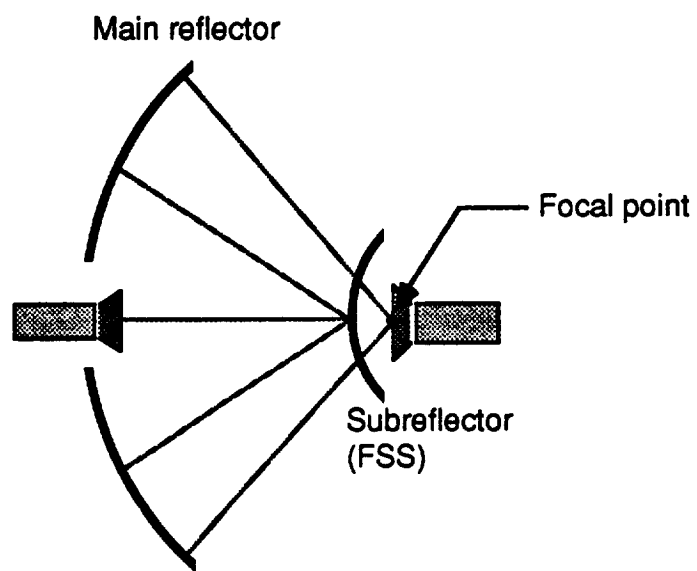


Figure 6.1. Cassegrain antenna. The focal point of the parabolic main reflector coincides with a focal point of the hyperbolic subreflector.

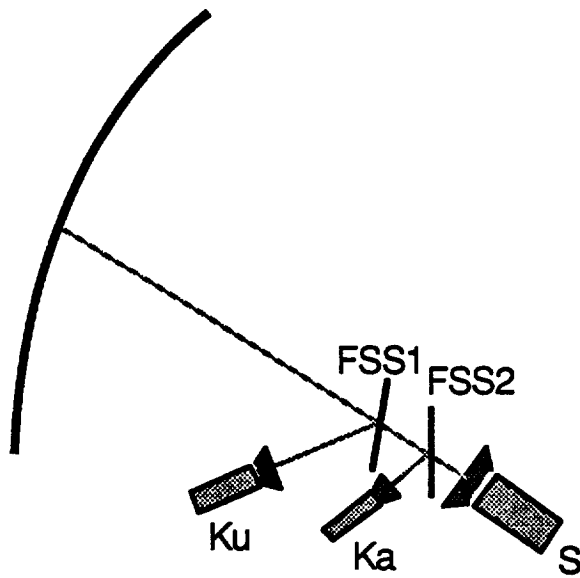


Figure 6.2. Offset design for proposed ATDRSS triband reflector antenna. The single reflector dish is parabolic and has a solid surface. The reflector is 150" in diameter with an offset height of 15" and a focal length of 130".

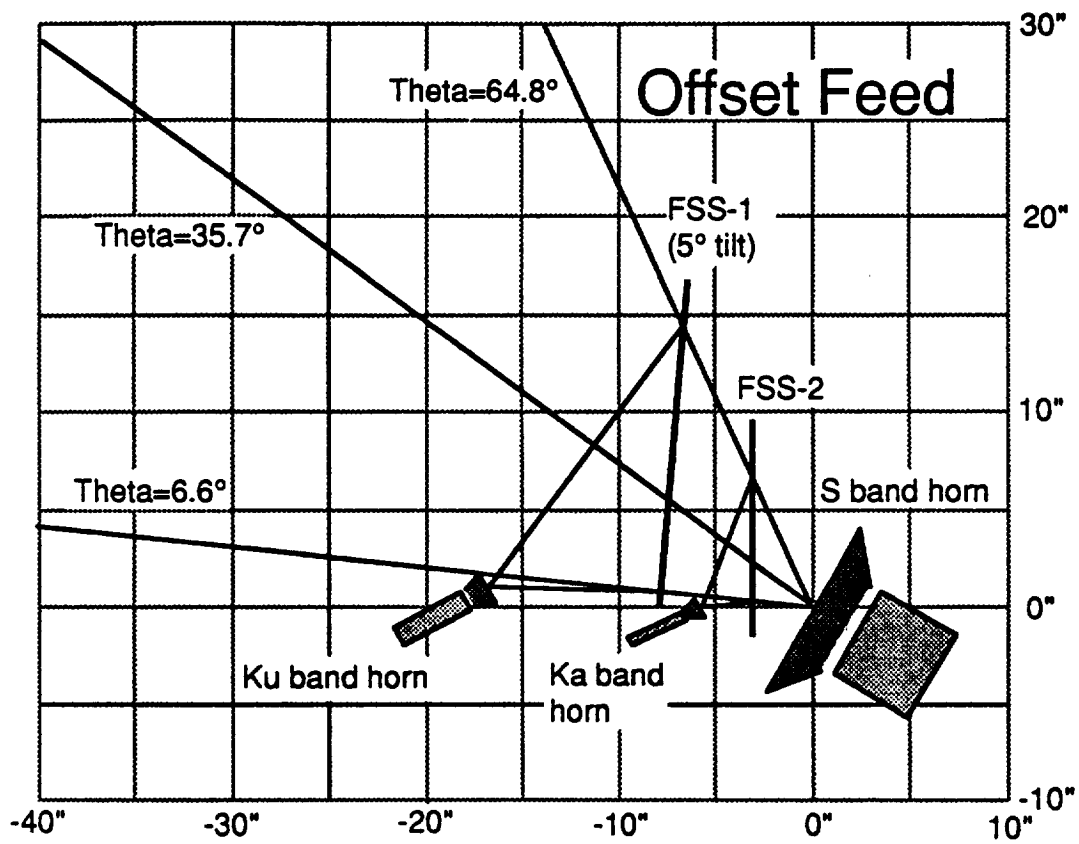


Figure 6.3. Close-up of offset design feed system. All three feeds are corrugated horns.

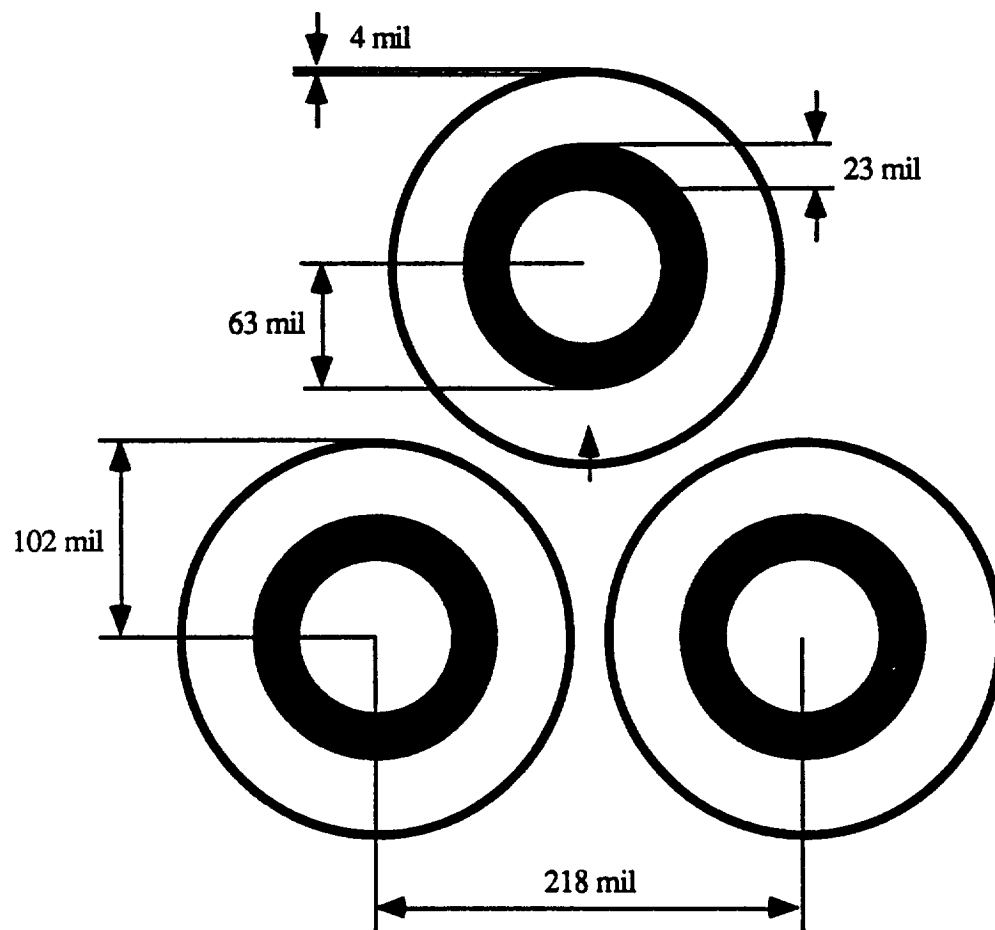


Figure 6.4. Geometry for FSS1.

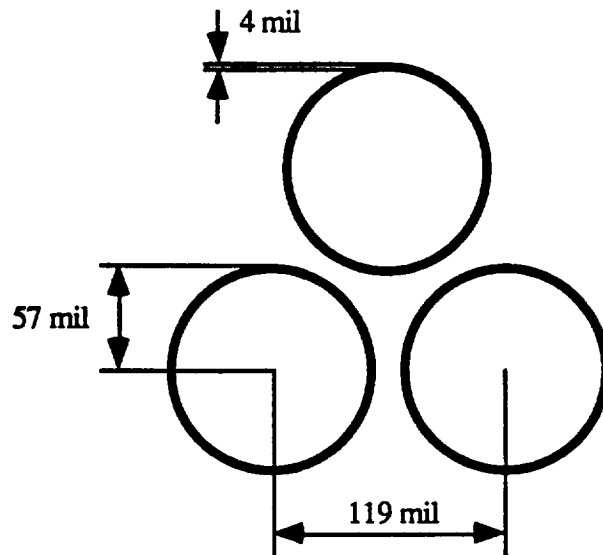


Figure 6.5. Geometry for FSS2.

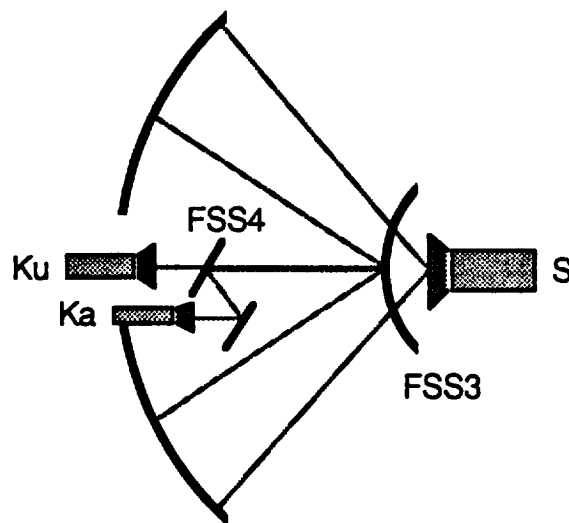


Figure 6.6. Dual symmetric design. The reflector is shaped and has a diameter=168". The subreflector has diameter=28".

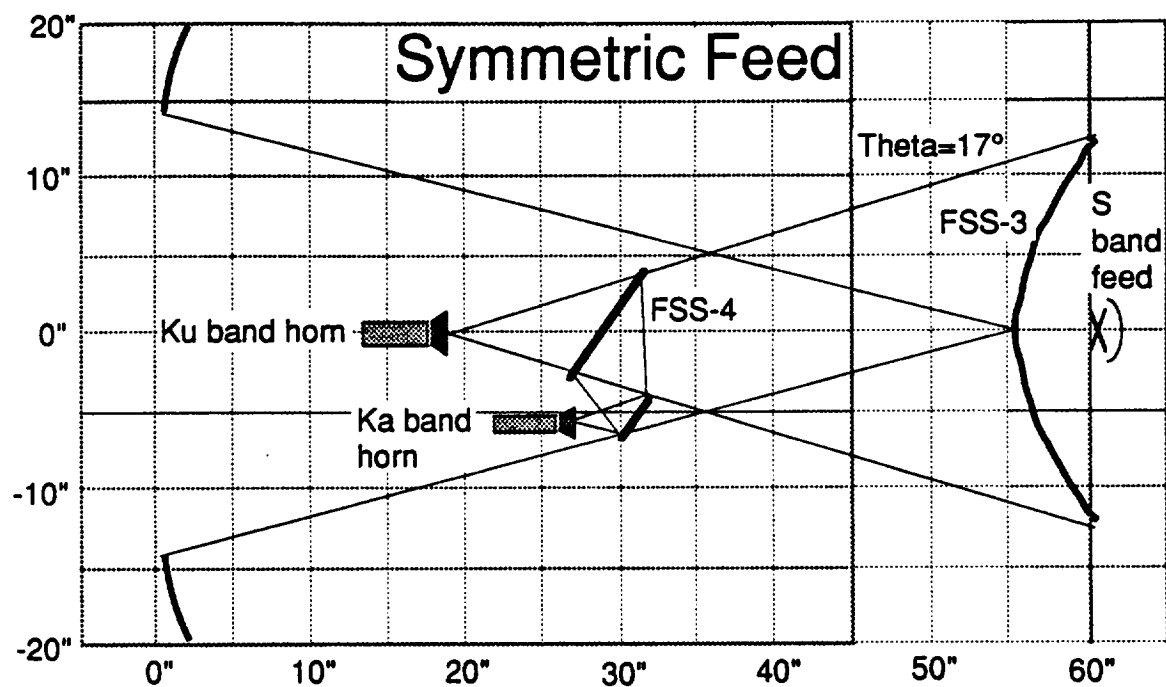


Figure 6.7. Close-up of the symmetric design feed system. The S-band feed is a crossed dipole with reflector, and the other feeds are corrugated circular horns.

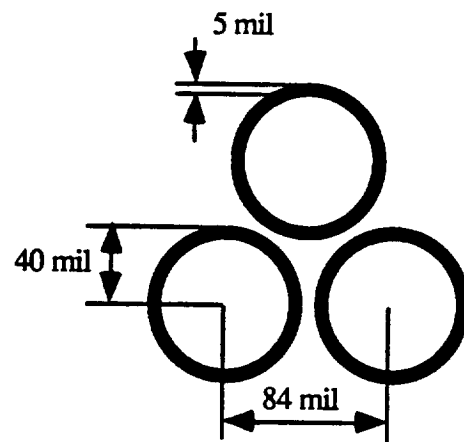


Figure 6.8. Geometry for FSS3.

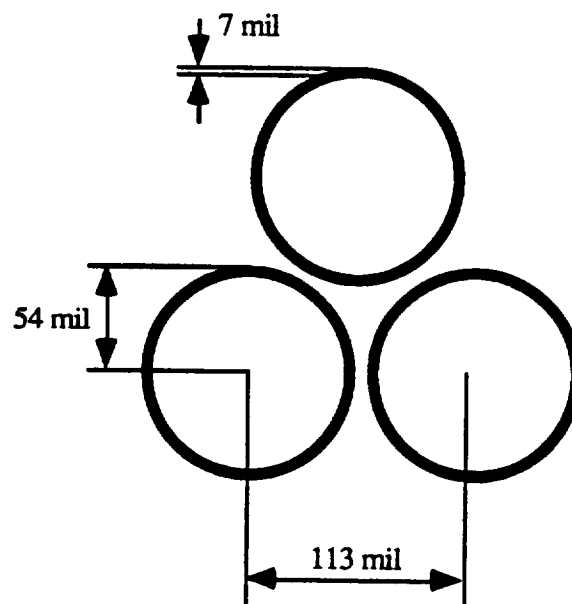


Figure 6.9. Geometry for FSS4.

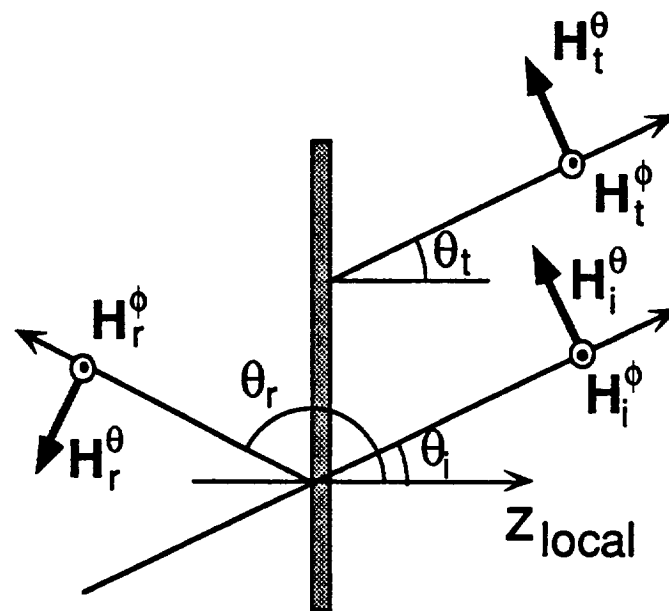


Figure 6.10. Interaction of wave with a surface. In general the surface may be curved.

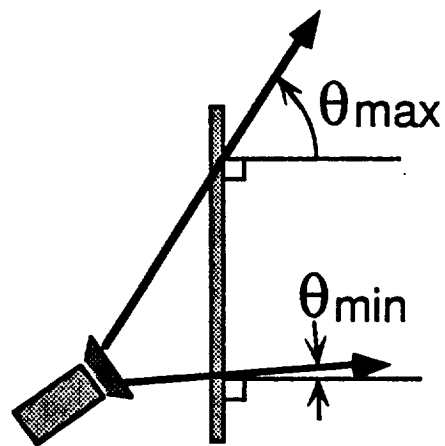


Figure 6.11. Since the feed does not emit a plane wave, the energy radiated is incident on a surface over a broad range of incident angles.

NASA
C-91-04635

1/13 Scale Model of Advanced Tracking and Data Relay Satellite (ATDRS) Concept Stowed for Launch

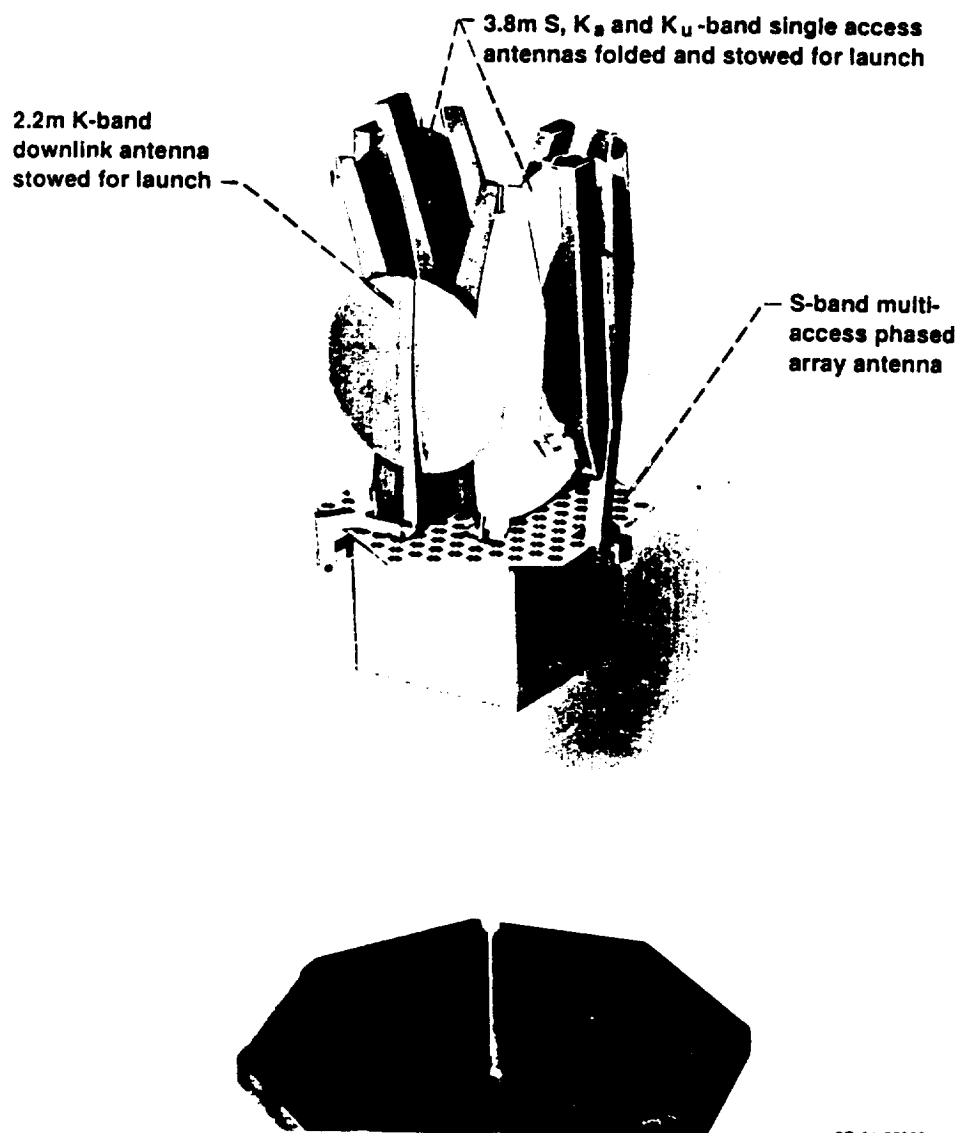


Figure 6.12. Model of proposed ATDRSS satellite showing the launch-ready configuration (photo courtesy of NASA).

MM2M
C-91-04633

1/13 Scale Model of Advanced Tracking and Data Relay Satellite (ATDRS) Concept Configured for Lunar and Out of Ecliptic Plane Missions

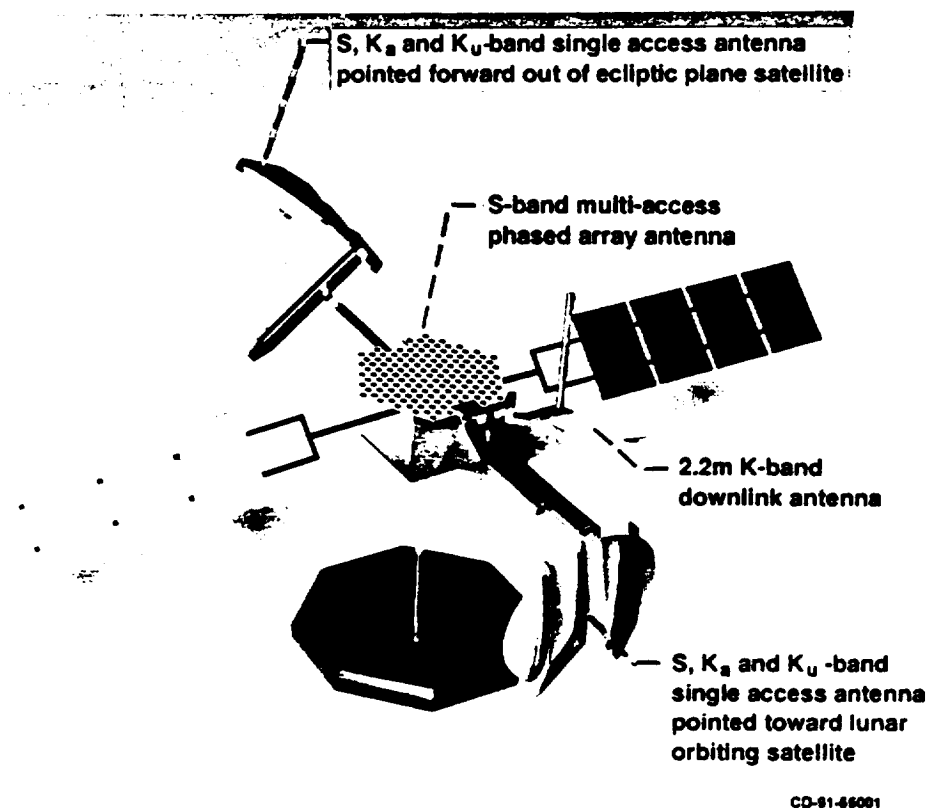


Figure 6.13. Model of proposed ATDRSS satellite showing the triband reflector antennas in the fully deployed mode (photo courtesy of NASA).

7. CONCLUSIONS

We have expanded existing methods of calculating far-field patterns for reflector antennas to include many of the difficulties presently encountered in reflector antenna design and analysis. By using methods of analysis that are generalized and allow for more variation, the scope of problem types that may be tackled is broadened. The purpose is to develop methods of analysis flexible enough to handle tomorrow's problems as well as today's. Using these techniques, problems such as spillover loss for reflector antenna waveguide feeds, optimization of beam efficiency for reflector antennas, and the analysis of reflector antenna systems including frequency selective surfaces have been addressed.

REFERENCES

- [1] L. J. Chu, "Calculation of the radiation properties of hollow pipes and horns," *J. Applied Phys.*, vol. 11, pp. 603-610, 1940.
- [2] J. R. Risser, "Waveguide and horn feeds," ch. 10 in *Microwave Antenna Theory and Design*, S. Silver, Ed. New York: Dover Publications, pp. 334-347, 1965.
- [3] C. A. Balanis, *Antenna Theory*, New York: Harper & Row, pp. 473-486, 1982.
- [4] Y. Rahmat-Samii, "Reflector antennas," ch. 15 in *Antenna Handbook*, Y. T. Lo and S. W. Lee, Ed. New York: Van Nostrand Reinhold, pp. 15-89 to 15-93, 1988.
- [5] A. D. Yaghjian, "Approximate formulas for the far field and gain of open-ended rectangular waveguide," *IEEE Trans. Antennas Propagat.*, vol. AP-32, pp. 378-384, April 1984.
- [6] S. Silver, *Microwave Antenna Theory and Design*. New York: McGraw-Hill, 1949.
- [7] J. F. Kaufman, W. F. Croswell, and L. J. Jowers, "Analysis of the radiation patterns of reflector antennas," *IEEE Trans. Antennas and Propagat.*, vol. AP-24, pp. 53-65, January 1976.
- [8] Y. Hwang, C. H. Tsao, and C. C. Han, *AP Digest*, p. 88, May 1983.
- [9] P. Lam and S. W. Lee, "Analysis and optimization of reflector antenna systems," EM Lab Report No. 85-9, University of Illinois, Urbana-Champaign, November 1985.
- [10] Y. Rahmat-Samii, P. Cramer Jr., K. Woo, and S. W. Lee, "Realizable feed-element patterns for multi-beam reflector antenna analysis," *IEEE Trans. Antennas and Propagat.*, vol. AP-29, pp. 961-963, 1981.
- [11] S. W. Lee, "Uniform asymptotic theory on electromagnetic edge diffraction: A review," EM Lab. Rep. 77-1, University of Illinois, Urbana-Champaign, Jan. 1977.
- [12] R. C. Menendez and S. W. Lee, "On the role of the geometrical optics field in aperture diffraction," *IEEE Trans. Antennas and Propagat.*, vol. AP-25, pp. 688-695, 1977.
- [13] S. W. Lee and G. A. Deschamps, "A uniform asymptotic theory of electromagnetic diffraction by a curved wedge," *IEEE Trans. Antennas and Propagat.*, vol. AP-24, pp. 25-34, 1976.
- [14] D. S. Ahluwalia, R. M. Lewis, and J. Boersma, "Uniform asymptotic theory of diffraction by a plane screen," *SIAM J. Appl. Math.*, vol. 16, pp. 783-807, 1968.
- [15] R. M. Lewis and J. Boersma, "Uniform asymptotic theory of edge diffraction," *J. Math. Phys.*, vol. 10 pp. 2291-2305, 1969.
- [16] A. C. Ludwig, "The definition of cross polarization," *IEEE Trans. Antennas and Propagat.*, vol. AP-29, pp. 580-586, 1981.

- [17] C. C. Hung and R. Mittra, "Wide-angle scanning for reflector antennas," *URSI Symposium Digest*, pp. 75, 1983.
- [18] J. C. Shiue and L. R. Dod, ch. 22 of *Antenna Handbook*, Y. T. Lo and S. W. Lee, Ed. New York: Van Nostrand Reinhold, pp. 15-89 to 15-93, 1988.
- [19] P. T. Lam, S. W. Lee, C. C. Hung, and R. Acosta, "Strategy for reflector pattern calculation: Let the computer do the work," *IEEE Trans. Antennas and Propagat.*, vol. 34, pp. 592-594, 1986.
- [20] H. C. Minnett and B. MacA. Thomas, "Fields in the image space of symmetrical focusing reflectors," *Proc. IEEE*, vol. 115, pp. 1419-1430, 1968.
- [21] A. W. Rudge and M. J. Withers, "Design of flared-horn primary feeds for parabolic reflector antennas," *Proc. IEEE*, vol. 117, pp. 1741-1749, 1970.
- [22] H. H. S. Luh, "On the radiation pattern of a multibeam antenna," *IEEE Trans. Antennas and Propagat.*, vol. AP-24, pp. 101-102, 1976.
- [23] Y. Rahmat-Samii and S. W. Lee, "Applications of the conjugate field matching technique to reflector antennas - a critical review," *URSI Digest*, pp. 85, 1981.
- [24] A. V. Mrstik and P. G. Smith, "Scanning capabilities of large parabolic cylinder reflector antennas with phased-array feeds," *IEEE Trans. Antennas and Propagat.*, vol. AP-31, pp. 756-763, 1983.
- [25] C. C. Hung and R. Mittra, "Secondary pattern and focal region distribution of reflector antennas under wide-angle scanning," *AP Digest*, vol. AP-31, pp. 463-470, 1983.
- [26] H. Y. Jong, B. Popovich, W. R. Adams, and A. W. Love, "Analysis of paraboloidal reflector fields under oblique incidence," *AP Digest*, vol. 1, pp. 305-308, 1984.
- [27] R. J. Acosta, "Compensation of reflector surface distortion using conjugate field matching," *AP Digest*, vol. 1, pp. 259-262, 1986.
- [28] P. T. Lam, S. W. Lee, D. C. D. Chang, and K. C. Lang, "Directivity optimization of a reflector antenna with cluster feeds: A closed form solution," *IEEE Trans. Antennas and Propagat.*, vol. AP-33, pp. 1163-1174, 1985.
- [29] R. Acosta, A. Zaman, E. Bobinsky, A. R. Cherrette, and S. W. Lee, "Case study of active array feed compensation with sidelobe control for reflector surface distortion," *AP-S International Symp. Digest*, vol. 2, pp. 863-867, 1988.
- [30] R. Acosta, "Active feed array compensation for reflector antenna surface distortion," NASA TM100826, NASA Lewis Research Center, Cleveland, OH, June 1988.
- [31] R. T. Nash, "Beam efficiency limitations of large antennas," *IEEE Trans. Antennas and Propagat.*, vol. AP-12, pp. 918-923, December 1964.
- [32] W. F. Croswell, Section 18 of *Electronics Engineer's Handbook*, Ed. D. G. Fink. New York, McGraw-Hill, 1976, p. 18-13 - 18-15.

- [33] C. A. Balanis, *Antenna Theory*. New York: Harper & Row, 1982, Fig. 11-21, p. 488.
- [34] J. A. Asvestas, "The physical optics method in electromagnetic scattering," *Journal of Math. Phys.*, vol. 21, pp. 290-299, February 1980.
- [35] S. W. Lee and M. L. Zimmerman, "Reflector spillover loss of an open-ended rectangular and circular waveguide feed," *IEEE Trans. Antennas and Propagat.*, June 1990, pp. 940-942.
- [36] M. Zimmerman, S. W. Lee, B. Houshmand, Y. Rahmat-Samii, and R. Acosta, "A comparison of reflector antenna designs for wide-angle scanning," *Microwave and Optical Technology Letters*, pp. 233-235, July 1990.
- [37] David K. Cheng, "Optimization techniques for antenna arrays," *Proc. IEEE*, vol. 59, No. 12, December 1971.
- [38] H. Kumazawa, M. Koyama, and Y. Kataoka, "Wide-band communication satellite antenna using a multifrequency primary horn," *IEEE Trans. Antennas and Propagat.*, vol. AP-23, pp. 403-407, May 1975.
- [39] M. S. Narasimhan and M. S. Sheshadri, "Propagation and radiation characteristics of dielectric loaded corrugated dual-frequency circular waveguide horn feeds," *IEEE Trans. Antennas and Propagat.*, vol. AP-27, p. 858-860, November 1979.
- [40] J. C. Lee, "A compact Q-/K-band dual frequency feed horn," *IEEE Trans. Antennas and Propagat.*, vol. AP-32, pp. 1108-1111, October 1984.
- [41] GE Astro Space, Tracking and data relay spacecraft (TDRS) study, advanced concept design report (SE-904), vol. 3, prepared for NASA GSFL, April 1989.
- [42] Ford Aerospace Corp., Space Systems Division, TDRSS advanced concept design report (SE-904), vol. 1, prepared for NASA GSFL, April 1989.
- [43] TRW Space & Technology Group, Tracking and data relay satellite study, advanced concept design report (SE-904), prepared for NASA GSFL, April 1989.

Technical Report GF92-1

ATDRSS: Further FSS Study

S. W. Lee, Sean Ni and M. Christensen
January, 1992

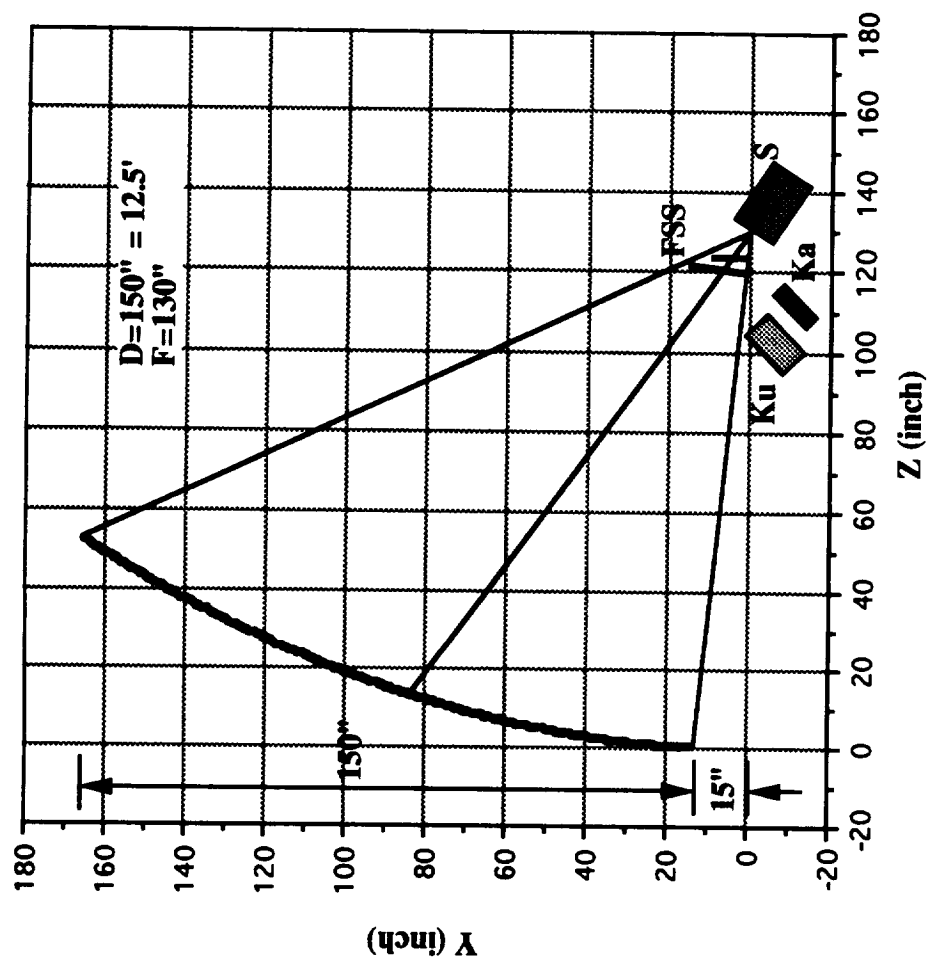
Electromagnetic Laboratory, University of Illinois
1406 W Green, Urbana, IL 61801
Tel (217)-333.0278, Fax (217)-333.5962

APPENDIX

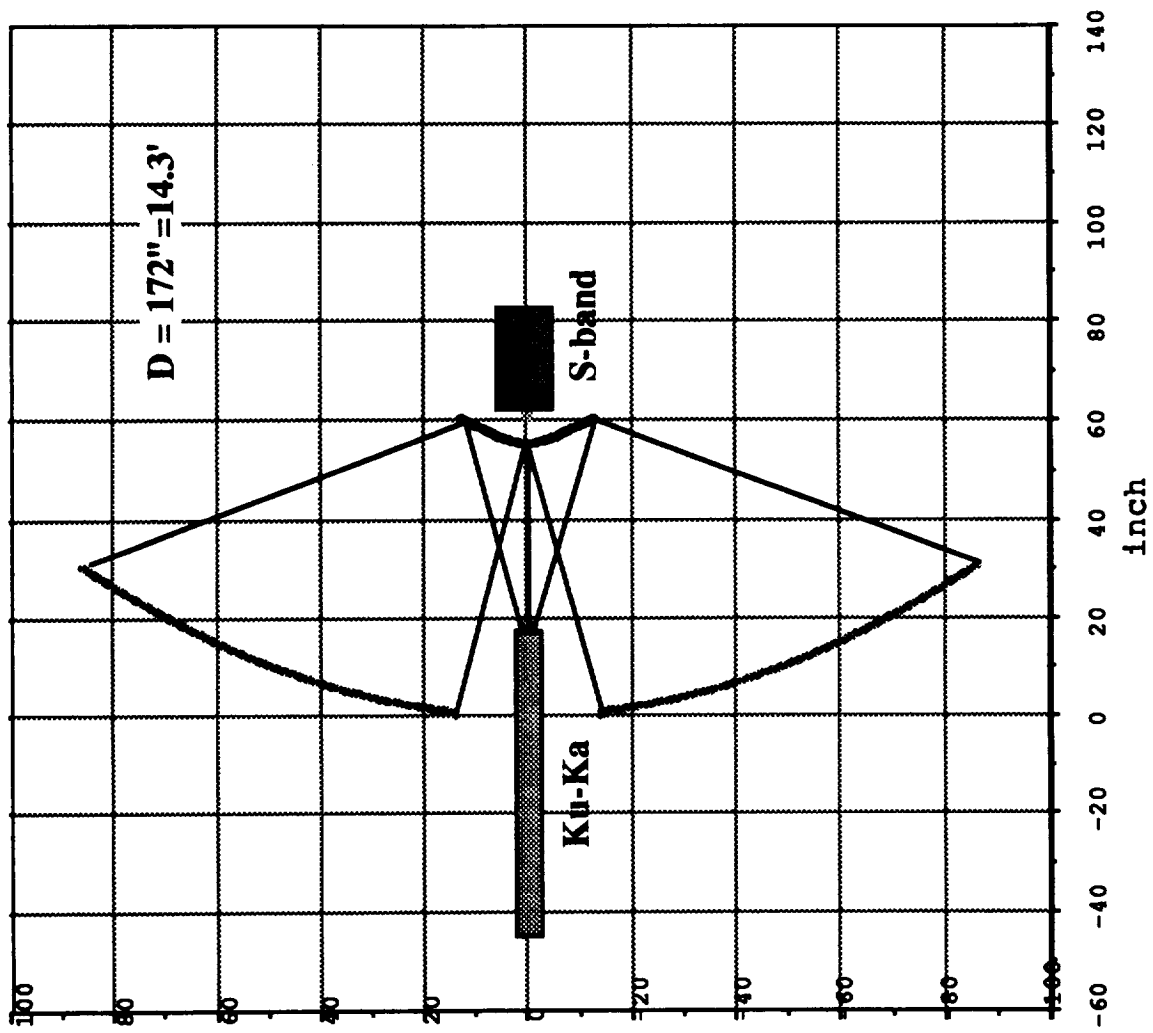
Review : 1990-1991

1. Design two reflectors: Offset 2 and Sym3
2. Design 4 FSS
3. Develop Integrated Analysis & computer code for reflector-FSS

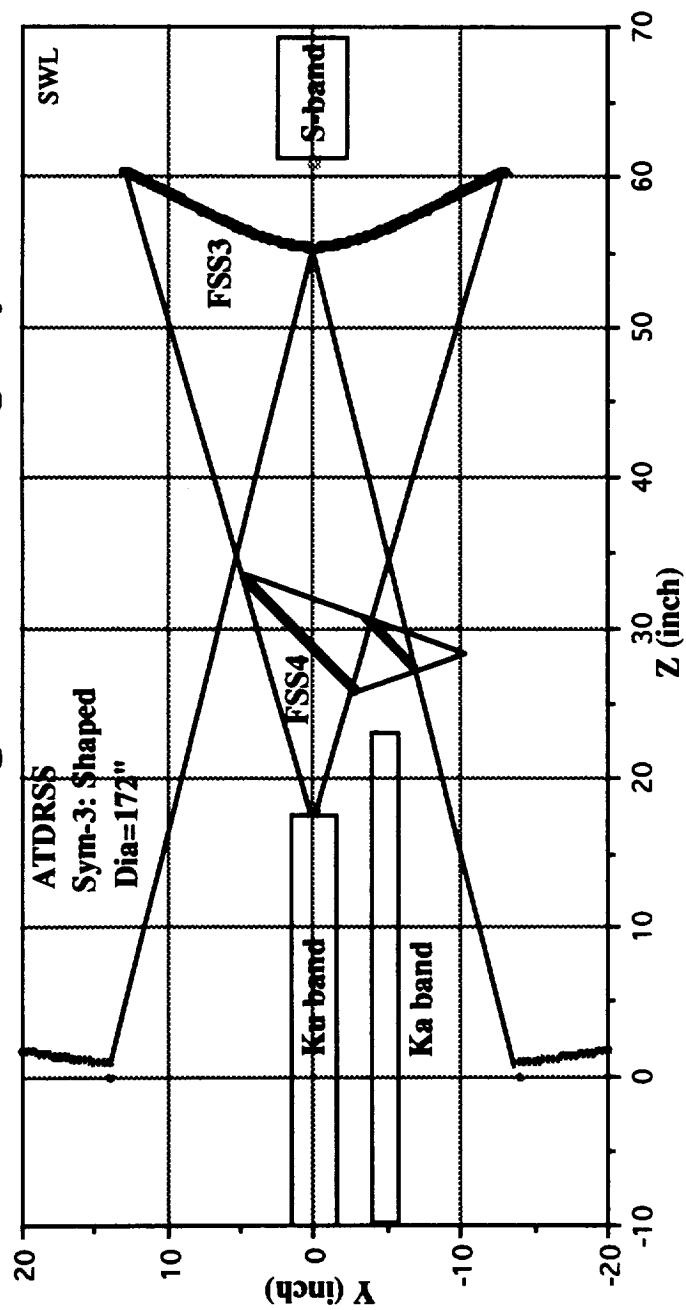
ATDRSS Design Offset-2



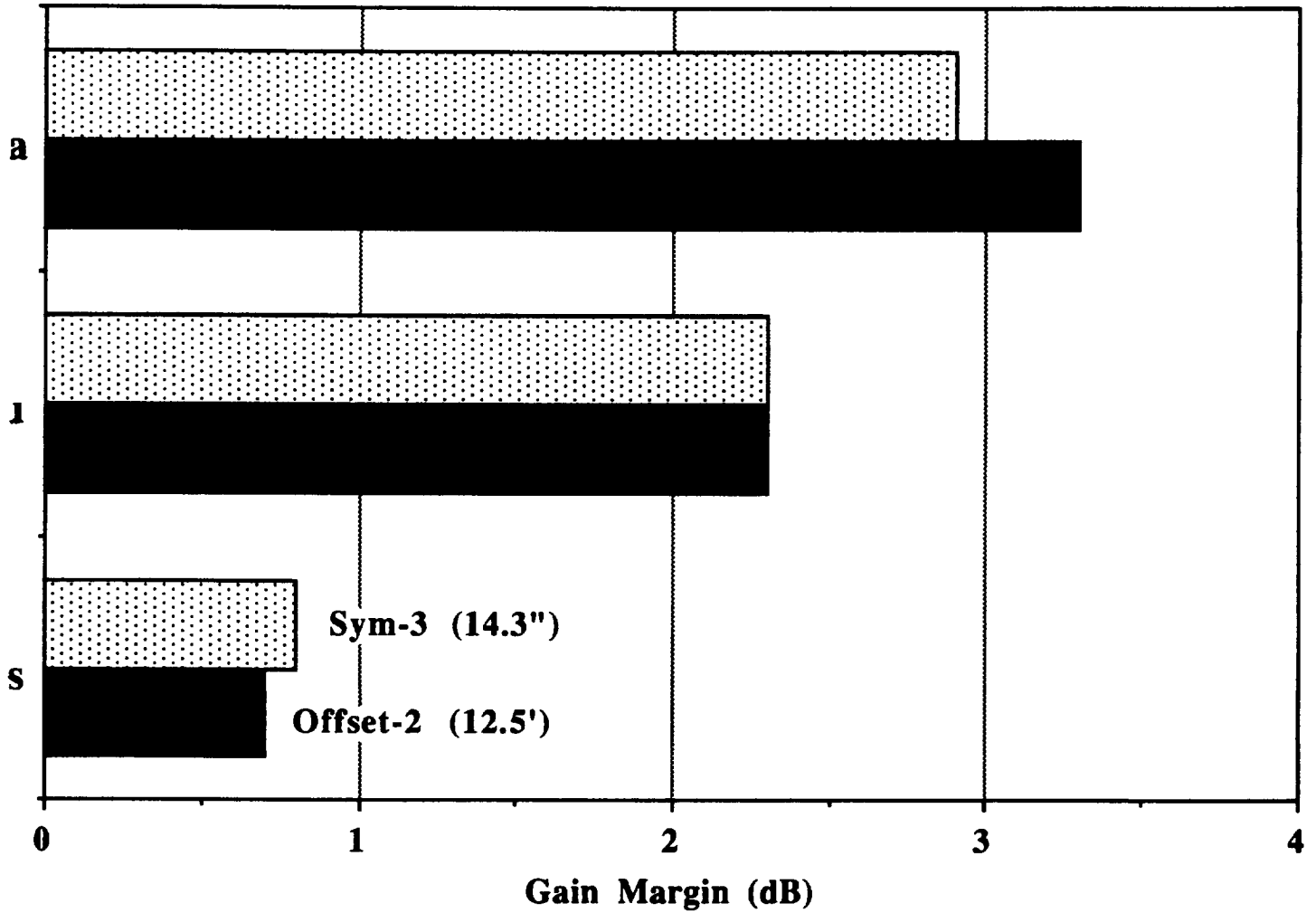
ATDRSS Sym-3 Shaped Reflector



Feed Arrangement for Design Sym-3



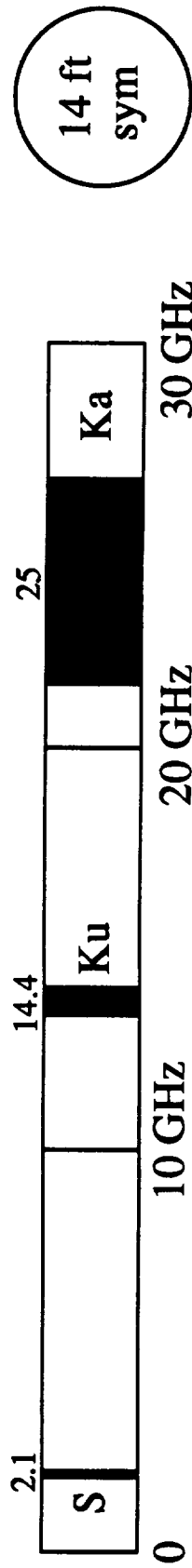
Gain Margin over TRW Spec



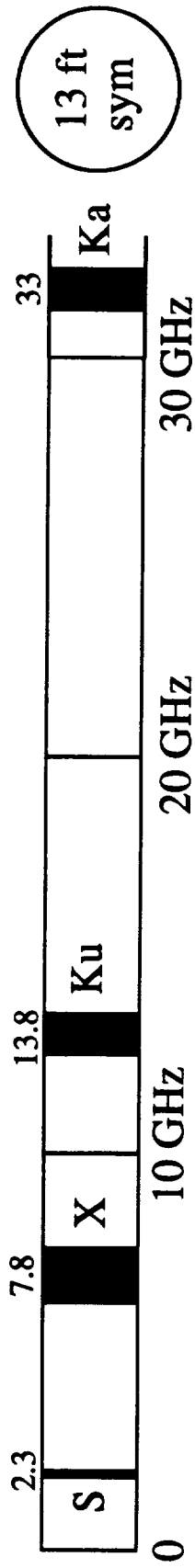
1992 Task: FSS

1. Who are using FSS ?
2. How accurate is our FSS computation model ?
3. FSS Problems to be studied.

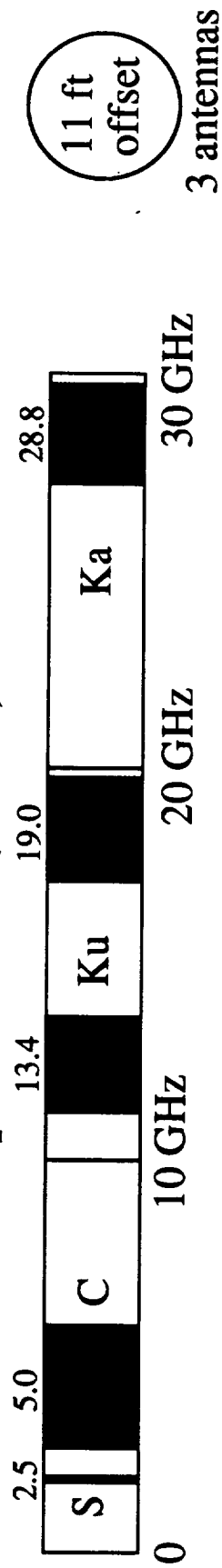
ATDRSS 1997



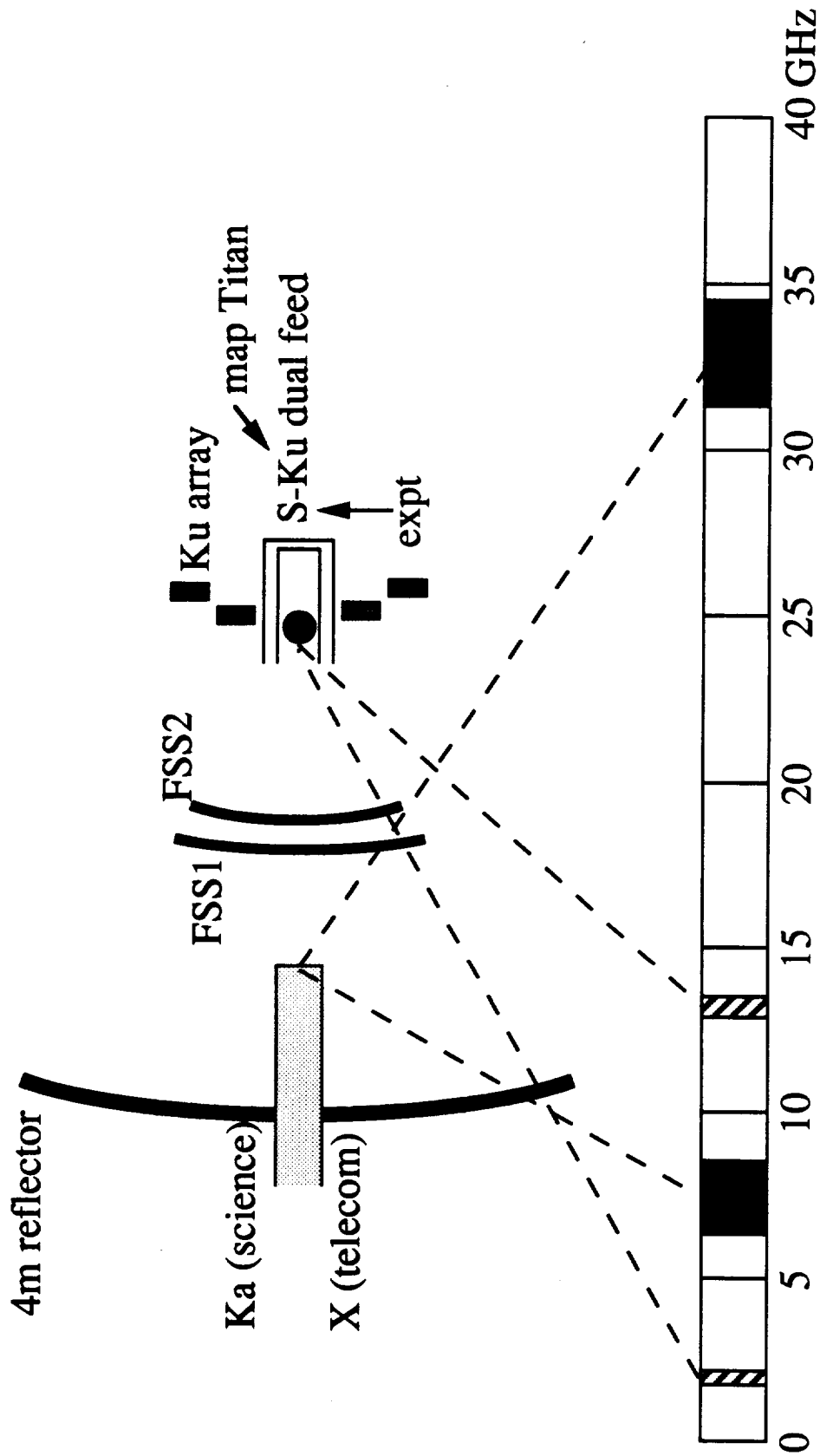
Italian Cassini 1997

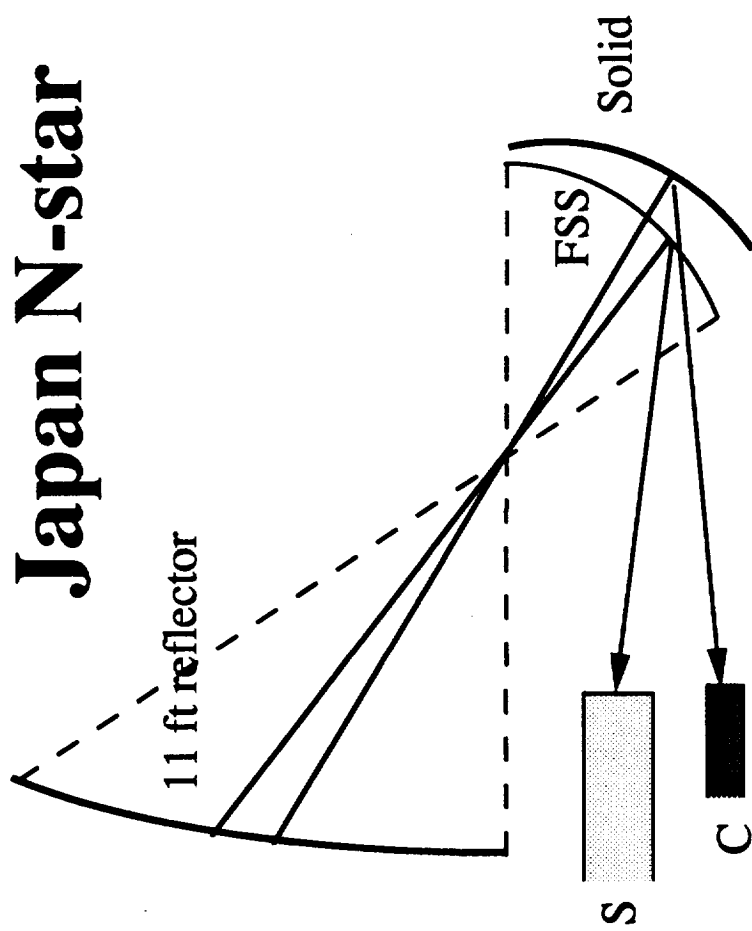


Japan N-star (Loral)



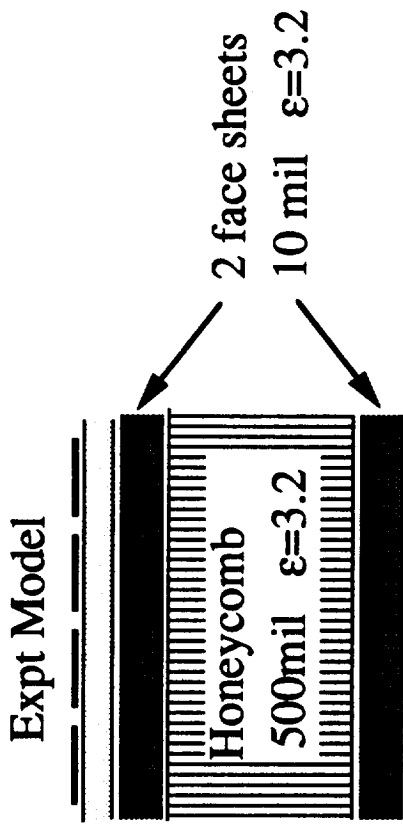
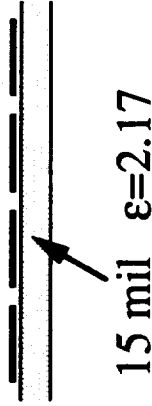
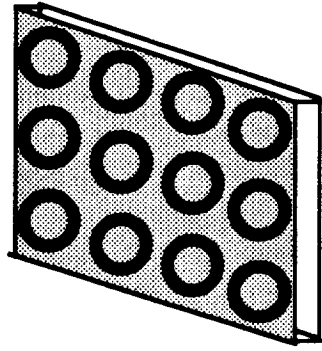
Cassini: Planet Saturn





FSS Problems

1. Mechanical Support Layers



Prob:

1. Extend analysis to multi-layer case
2. Re-design FSS with support layers

2. Curved Surface FSS arrangement

3. N-Star type FSS applied to ATDRSS

4. Cooperation with industry

Technical Report GF92-2

Multi-Ring FSS Analysis Using Coaxial Waveguide Modes

S. W. Lee, M. Christensen and Sean Ni
October 5, 1992

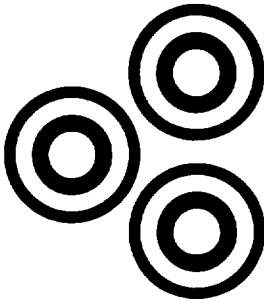
Electromagnetic Laboratory, University of Illinois
1406 W Green, Urbana, IL 61801
Tel (217)-333.0278, Fax (217)-333.5962

1992 FSS Study

1. Developing FSS analysis with thick-rings and honeycomb support
2. Optimizing a dozen FSS configurations for ATDRSS application
3. A side product: analysis of meander-line polarizer
4. Report for 1992 study:
 - * Rept 92-1: Viewgraphs for January 92 visit
 - * Rept 92-2: Viewgraphs for October 92 visit
 - * Rept 92-3: Detailed analysis of thick-ring FSS

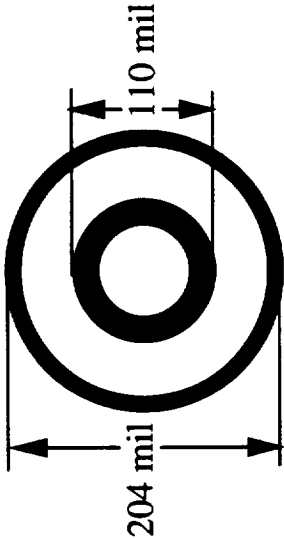
RING-001

Lattice



lattice side = 217 mil
lattice angle = 60°

Ring element



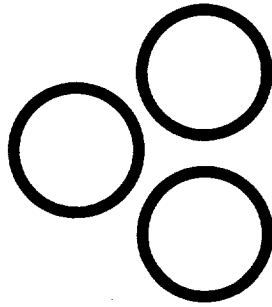
outer ring width = 5 mil
inner ring width = 20 mil

Side View



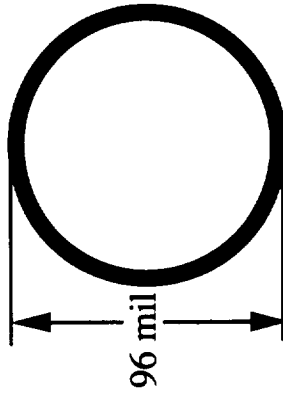
RING-002

Lattice



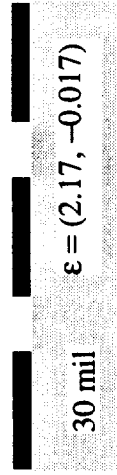
lattice side = 98 mil
lattice angle = 60°

Ring element



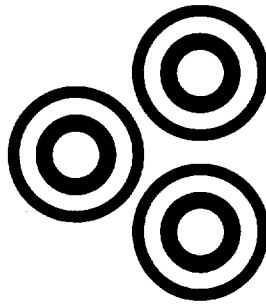
ring width = 2 mil

Side View



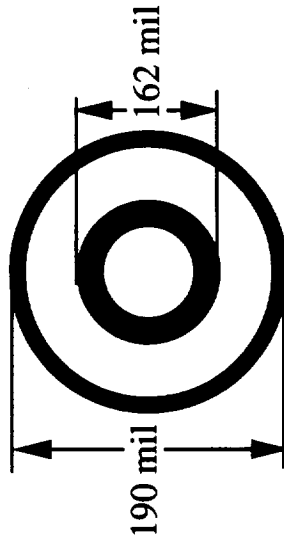
RING-003

Lattice



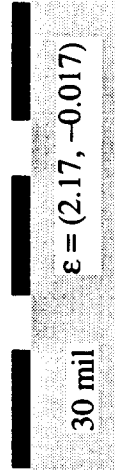
lattice side = 197 mil
lattice angle = 60°

Ring element



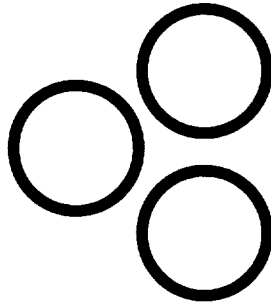
outer ring width = 6 mil
inner ring width = 20 mil

Side View



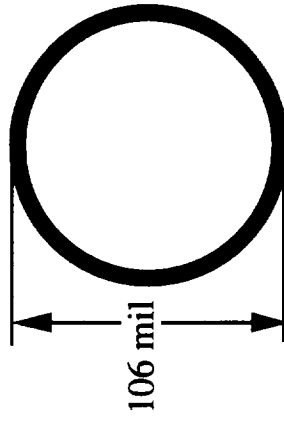
RING-004

Lattice



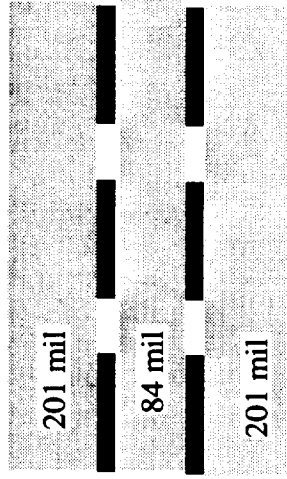
lattice side = 111 mil
lattice angle = 60°

Ring element



ring width = 8 mil

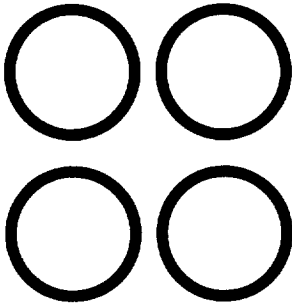
Side View



All $\epsilon = (2.17, -0.017)$

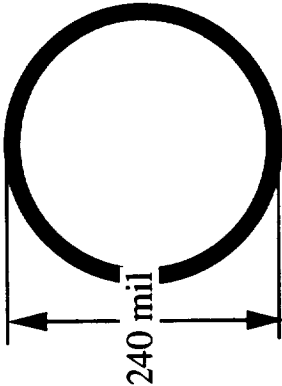
RING-005

Lattice



lattice side = 285 mil
lattice angle = 90°

Ring element



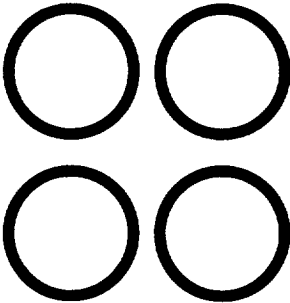
ring width = 10 mil

Side View



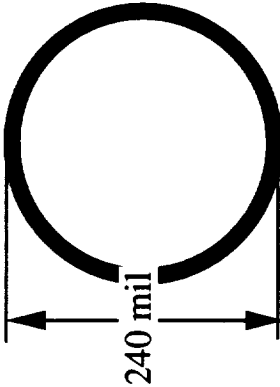
RING-006

Lattice



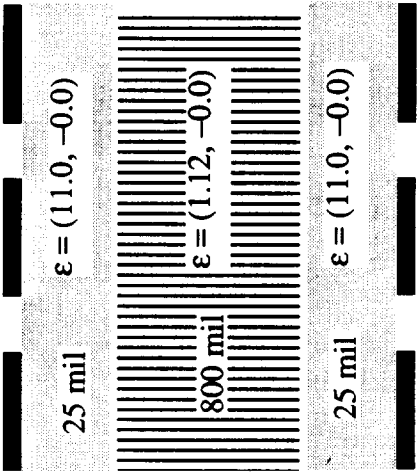
lattice side = 285 mil
lattice angle = 90°

Ring element



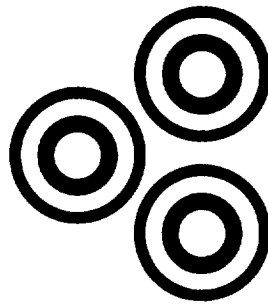
ring width = 10 mil

Side View



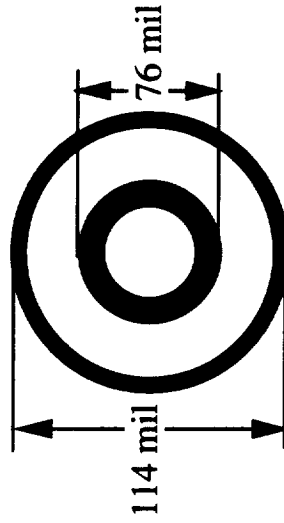
RING-007

Lattice



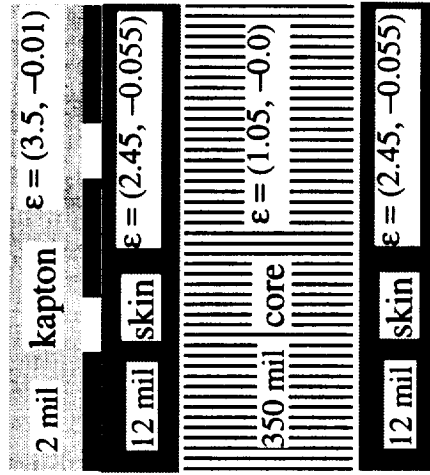
lattice side = 169 mil
lattice angle = 60°

Ring element

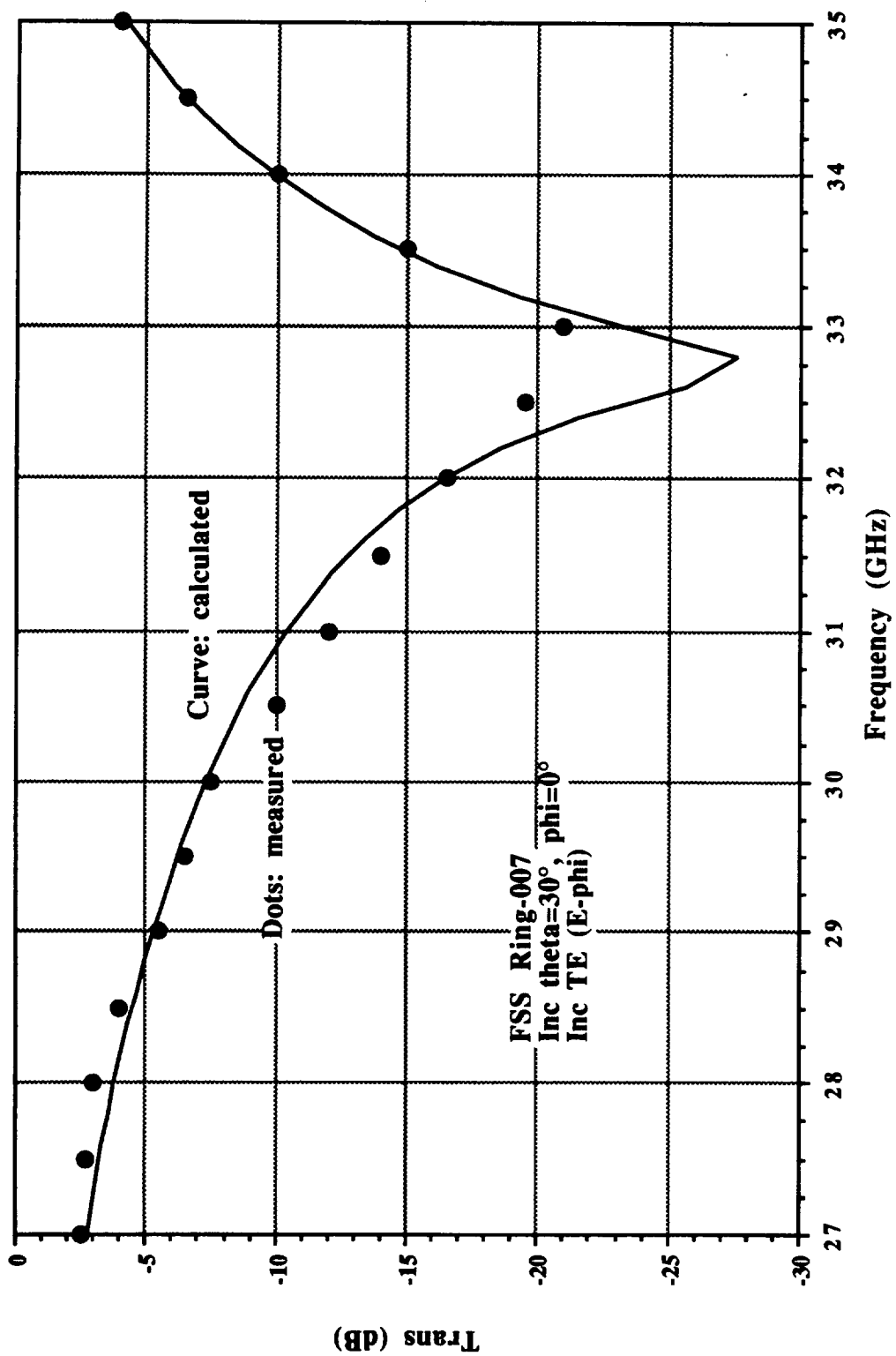


outer ring width = 10 mil
inner ring width = 10 mil

Side View

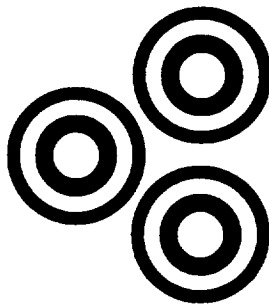


Kevlar honeycomb



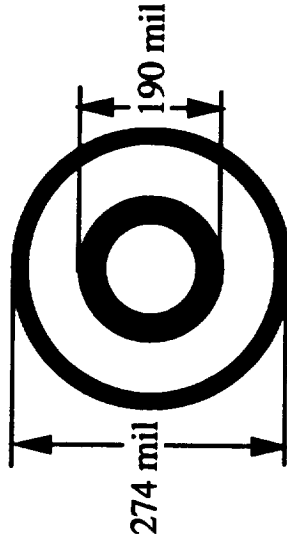
RING-008

Lattice



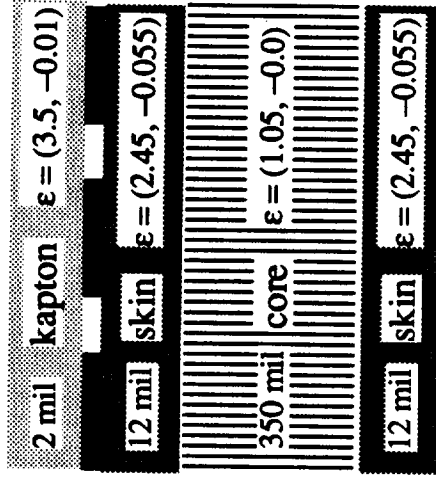
lattice side = 280 mil
lattice angle = 60°

Ring element

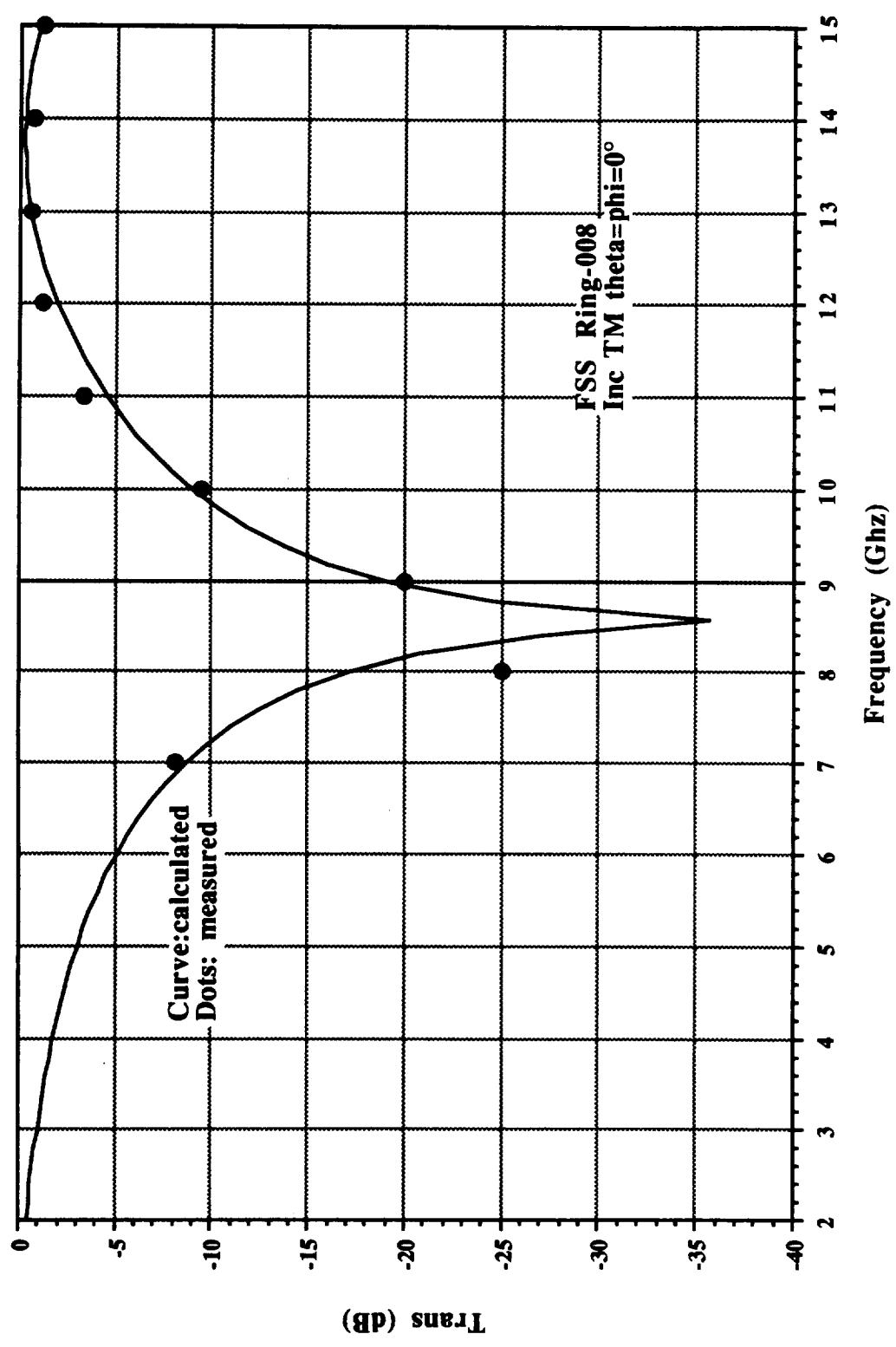


outer ring width = 5 mil
inner ring width = 8 mil

Side View

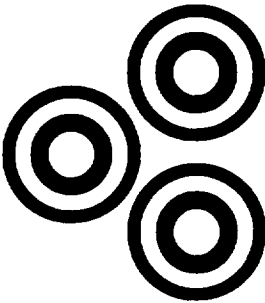


Kevlar honeycomb



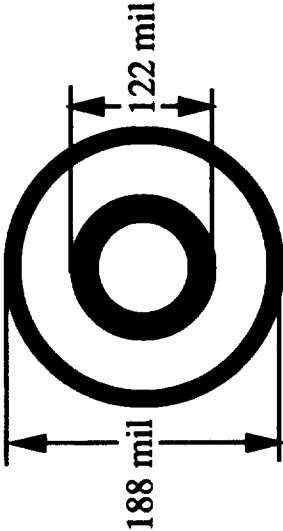
RING-009

Lattice



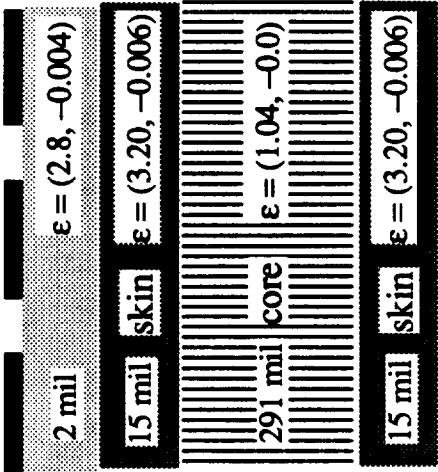
lattice side = 197 mil
lattice angle = 60°

Ring element



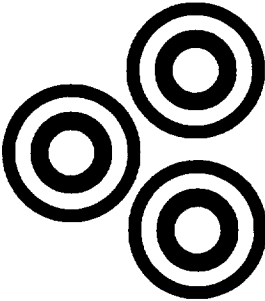
outer ring width = 8 mil
inner ring width = 26 mil

Side View



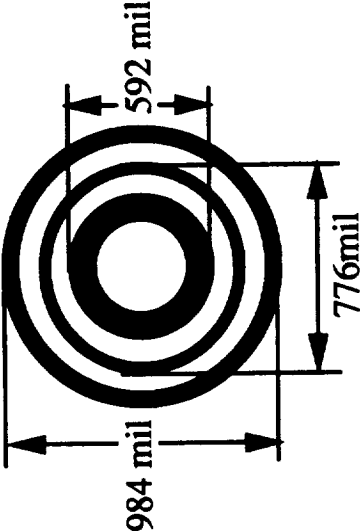
RING-010

Lattice



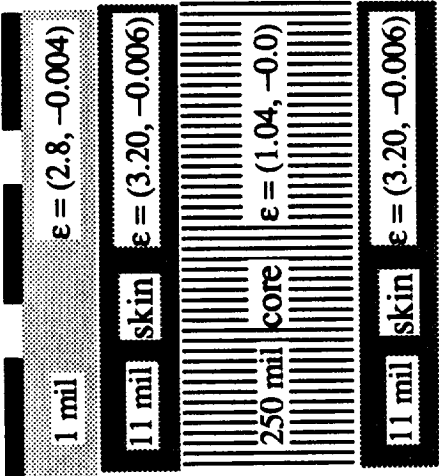
lattice side = 1010 mil
lattice angle = 60°

Ring element

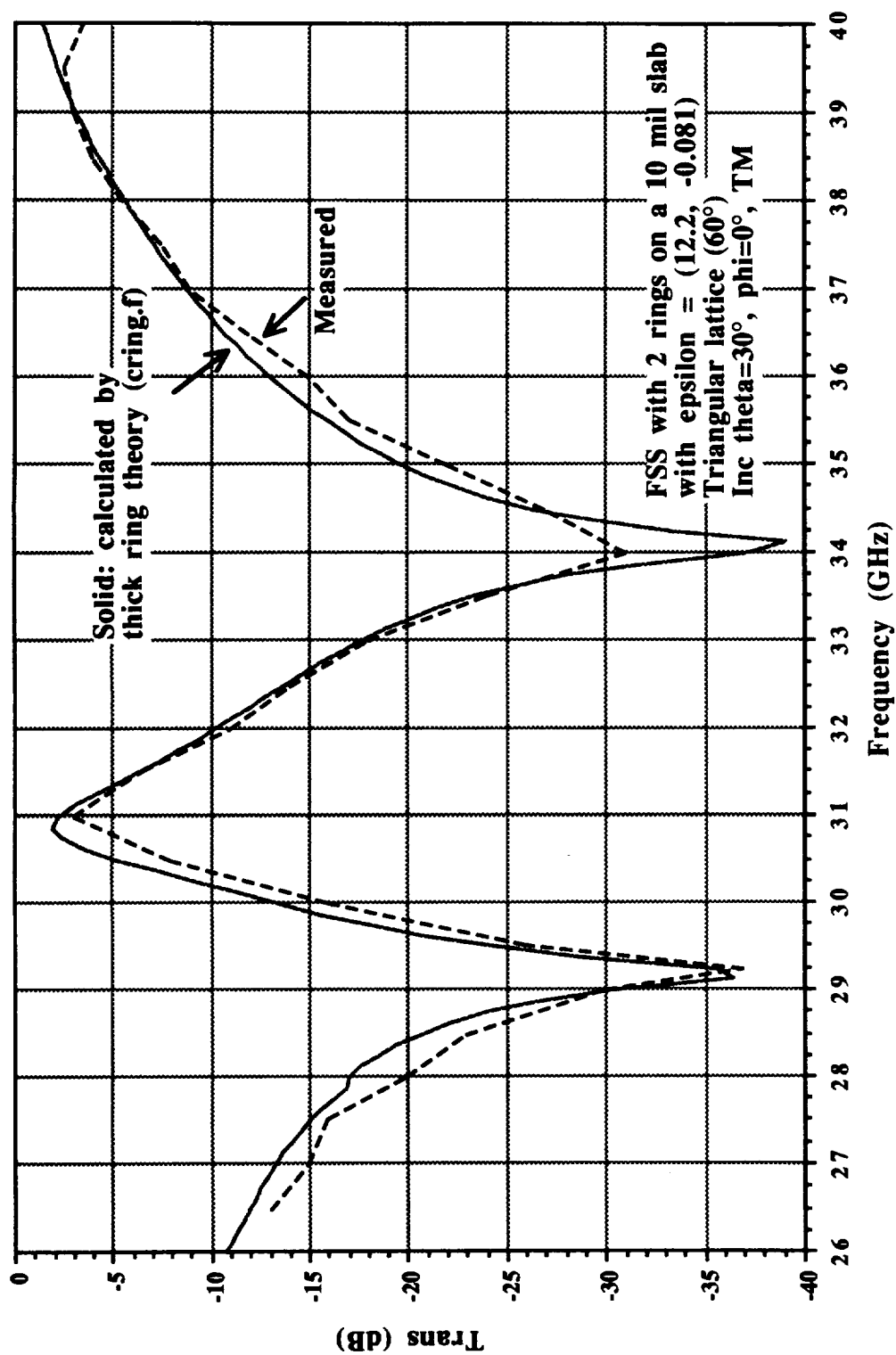


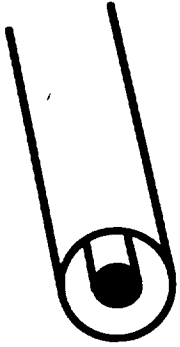
outer ring width = 12 mil
middle ring width = 88 mil
inner ring width = 186 mil

Side View

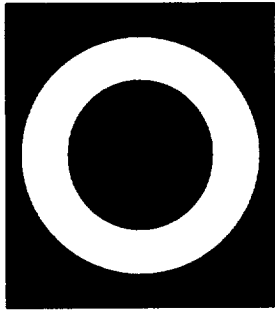


Computer code using thick ring theory gives good results



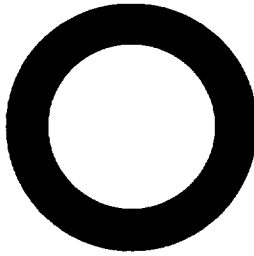


Coaxial waveguide modes



For inductive FSS:

Field in gap = Σ Coaxial modes with unknown coeff



For capacitive FSS (used in ATDRSS)

Current on ring = Σ Coaxial modes with unknown coeff

FSS analysis : * Match fields at interfaces to derive matrix equation
 * Invert matrix to solve unknown modal coeff

Conclusion

1. Concentric ring element is the best
2. Thick ring theory is a must for ka-ku band.
3. Prediction confirmed by measurements
4. FSS design must taken into consideration of honeycomb support
5. Ten FSS designs for ATDRSS applications
6. Stringent tolerance: 1 mil in geometry & 5% in dielectric constant
7. Currently, planar FSS can be built, implies offset reflector
8. Nobody wants to try curved FSS

Technical Report GF92-3

FSS Analysis with Thick Multiple Rings

S. W. Lee and Y. M. Wang
October 1992

Electromagnetic Laboratory, University of Illinois
1406 W Green, Urbana, IL 61801
Tel (217)-333.0278, Fax (217)-333.5962

Abstract

A frequency selective surface (FSS) with concentric metal ring elements are analyzed by a mode matching technique. The currents on the metal rings are represented by modal functions of a coaxial waveguide. Both the circumferential and radial field variations are accounted for. As a result, the present analysis applies to thin as well as thick rings.

Several FSS configurations are designed for the ATDRSS application, which requires the separation of three frequency bands: S, Ku, and Ka bands. A typical configuration consists of a thin layer of periodic concentric metal rings printed on a 10 to 20 mil substrate. The substrate is supported by a three-layer honeycomb structure for mechanical strength. All five layers are used in the present analysis. Our calculated results are in good agreement with measurements. Conclusions about using FSS for the ATDRSS and similar projects are given below.

(i) Among various FSS elements (dipole, tripole, cross, rectangular or circular aperture), the circular ring element stands out as the best in terms of control of pass-stop bands, and stability with respect to incident angle/polarization. Another advantage of rings is that rings of different radii can be concentrically arranged for multi-band operations.

(ii) A theory and a computer code 'cring.f' have been developed under the present project. The code can be used to analyze, design, and optimize ring FSS. A dozen of good FSS designs generated by cring.f are given. Some of them have been verified experimentally. Those designs can serve as templates for future applications.

(iii) FSS designed for Ka-band operation requires very stringent tolerances, namely, the geometrical dimension be accurate within 1 mil, and the dielectric constant be precise and homogeneous within 5%. If those tolerances are not met, FSS performance deteriorated rapidly.

(iv) Because of the tolerance problem, FSS in the Ka-band can be built with confidence only in a planar form, but not in a doubly curved form that is required for a symmetrical reflector antenna. As a result, the use of FSS in an ATDRSS-type reflector is restricted to off-set configurations. Of course, the tolerance problem will be eased as mechanical and material

controls improve. Future use of FSS in a ATDRSS type system, even for a curved sub-reflector, is promising.

This report consists of three parts. The first two are view graphics used in the project review meetings in January and October, 1992. The last one contains the mathematical analysis of the FSS with thick ring width.

Introduction

Analysis of frequency selective surface (FSS) is rapidly becoming a mature subject in the electromagnetic theory [1-2]. Invariably, FSS is modeled by an infinitely large periodic structure. The reflected and transmitted fields in space are represented by discrete Floquet modes. The analysis problem then becomes the determination of the Floquet modal coefficients by matrix equations.

There are many different metal elements can be used and have been used to form a periodic FSS. Examples are rectangular plate, circular plate, cross, Jerusalem cross, dipole, tri-pole, rectangular rings, and circular rings. In the past years, the circular ring element has emerged as the best element for applications because of its

- * good pass band and good band characteristics,
- * relatively stable performance with respect to incident angles and polarization, and
- * concentric ring configuration that allows multiple band operation.

In the last year project, we used the ring elements to design a set of four FSS for the ATDRSS application [3]. That design was done with a computer code named 'ring.f'.

In ring.f computer code, there are two assumptions on the structure of the FSS. First, the width of the metal rings are assumed thin in terms of electrical wavelength. As a result, the current on the ring has no radial component and no radial variation [4]. The second assumption is that the metal ring sheet is rested on a single dielectric substrate.

Both assumptions turn out too restrictive for the ATDRSS application. To order to better control FSS performance, it is necessary to use rings with wide width, say 0.4 wavelength width. Furthermore, in actual reflector application, FSS is glued to a supporting honeycomb structure. It has been found by a study a NASA Lewis that support structure has profound effect on the FSS performance, and it must be taken into consideration in the analysis.

A new computer code named 'cring.f' is developed in the current project. The current on the metal rings are represented by the coaxial waveguide modes, which have both circumferential

as well as radial variation and field components. In cring.f, there is no restriction on the number of substrate layers. Thus it can be used to model the composite structure of FSS and its honeycomb support. A description of the analysis that cring.f is based on is presented in this report. New designs for ATDRSS application are given in [5].

Reference

- [1] C. C. Chen, "Scattering by a two-dimensional periodic array of conducting plates", IEEE Trans. Antennas Propagat., Vol. AP-18, pp.660-665, 1970.
- [2] S. W. Lee, " Scattering by dielectric loaded screen", IEEE Trans. Antennas Propagat., Vol. AP-19, pp.656-665, 1971.
- [3] E. A. Parker and J. C. Vardaxoglou, " Influence of single and multiple-layer dielectric substrates on the band spacing available from a concentric ring frequency selective surface", International Journal of Electronics, Vol.61, pp.291-297, 1986.
- [4] M.L.Zimmerman and S.W.Lee, "Integrated reflector antenna design and analysis", EM Lab. Rept MZ1-91, University of Illinois, Urbana, IL 61801, July 1991.
- [5] S.W.Lee, M. Christensen and Sean Ni, " Multi-ring FSS analysis using coaxial waveguide modes", EM Lab. Rept GF92-2, University of Illinois, Urbana, IL 61801, October 5 1992 (this report is included in this volume).

Chapter 1. Mathematical Analysis of FSS

In this chapter, the formulations for calculating the transmission and reflection from an infinitely large periodic frequency selective surface (FSS) are derived. The FSS is made of capacitive multiple metal rings. The computer code used in the later chapters is based on the formulations presented in this chapter.

1.1. Field Representation

The geometry of the rings is shown in Figure 1.1. In the mathematical analysis, let us assume that the metal ring is not perfectly conducting, but with a finite surface resistivity R_c (e.g., $R_c = 100$ ohm per square). In the current version of the code, R_c is set to zero. As will be shown in the analysis, the addition of finite R_c is a relatively minor step. We can add the finite R_c capability to “cring” with a small effort.

The configuration in Figure 1.1 is horizontally stratified. A typical region defined by $z_1 < z < z_2$, the field is derived from two potentials

$$\text{TE: } \mathbf{E} = -\nabla \times (\hat{z}\psi). \quad (1.1.1)$$

$$E_x = -\frac{\partial \psi}{\partial y} \quad H_x = \frac{1}{jk_0 Z_0 \mu} \frac{\partial^2 \psi}{\partial x \partial z}$$

$$E_y = \frac{\partial \psi}{\partial x} \quad H_y = \frac{1}{jk_0 Z_0 \mu} \frac{\partial^2 \psi}{\partial y \partial z}$$

$$E_z = 0 \quad H_z = \frac{1}{jk_0 Z_0 \mu} \left(\frac{\partial^2}{\partial z^2} + k_0^2 \epsilon \mu \right) \psi$$

$$\text{TM: } \mathbf{H} = \frac{1}{Z_0} \nabla \times (\hat{z}\bar{\psi}) \quad (1.1.2)$$

$$E_x = \frac{1}{jk_0 \epsilon} \frac{\partial^2 \bar{\psi}}{\partial x \partial z} \quad H_x = \frac{1}{Z_0} \frac{\partial \bar{\psi}}{\partial y}$$

$$E_y = \frac{1}{jk_0\epsilon} \frac{\partial^2 \bar{\psi}}{\partial y \partial z}$$

$$H_y = \frac{-1}{Z_0} \frac{\partial \bar{\psi}}{\partial x}$$

$$E_z = \frac{1}{jk_0\epsilon} \left(\frac{\partial^2}{\partial z^2} + k_0^2 \mu \epsilon \right) \bar{\psi}$$

$$H_z = 0$$

where $k_0 = \omega(\mu_0\epsilon_0)^{1/2}$, $Z_0 = (\mu_0/\epsilon_0)^{1/2}$, and (ϵ, μ) are the relative dielectric constant, permeability in the region of interest.

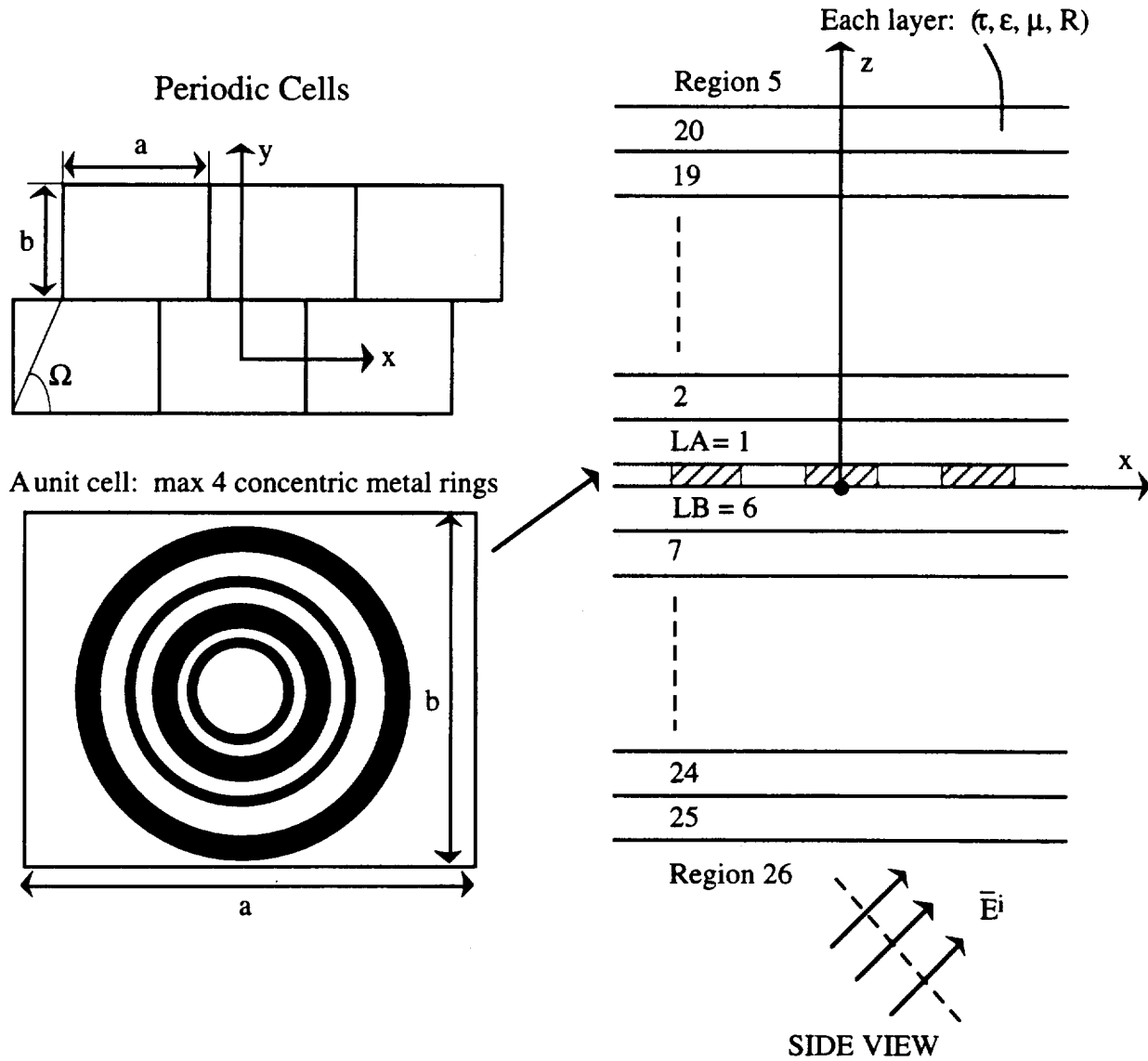


Figure 1.1. A resistive FSS illuminated by an incident plane wave.

MODE MATCHING FOR PERFECT CONDUCTING SCREEN

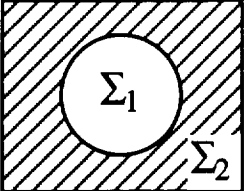
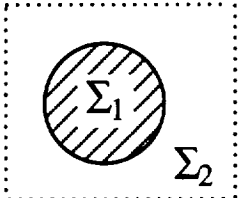
Inductive	Capacitive
	
$\vec{E}_t(0-) = \vec{E}_t(0+), \Sigma_1 + \Sigma_2$ $\vec{E}_t(0-) = \begin{cases} \vec{E}_t(0) & , \Sigma_1 \\ 0 & , \Sigma_2 \end{cases}$ $\vec{H}_t(0-) = \vec{H}_t(0+) , \Sigma_1$	<p>Same</p> $\vec{J}_s(\text{outside}) = \begin{cases} \vec{J}_s(0) & , \Sigma_1 \\ 0 & , \Sigma_2 \end{cases}$ $\vec{E}_{\tan}(0-) = 0 , \Sigma_1$

Figure 1.2. Mode matching equations for a perfectly conducting screen.

MODE MATCHING FOR RESISTIVE SCREEN

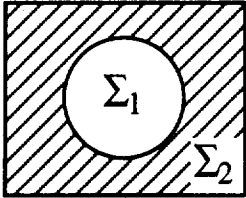
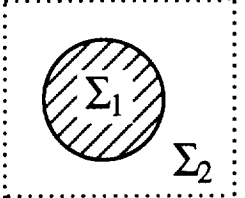
Inductive	Capacitive
	
$\vec{E}_t(0-) = \vec{E}_t(0+), \Sigma_1 + \Sigma_2$ $\vec{E}_t(0-) = \begin{cases} \vec{E}_t(0) & , \Sigma_1 \\ R_c J_s(\text{outside}) & , \Sigma_2 \end{cases}$ $\vec{H}_{\text{tan}}(0-) = \vec{H}_{\text{tan}}(0) , \Sigma_1$	<p style="text-align: center;">Same</p> $\vec{J}_s(\text{outside}) = \begin{cases} \vec{J}_s(0) & , \Sigma_1 \\ 0 & , \Sigma_2 \end{cases}$ $\vec{E}_t(0-) = R_c J_s(0) , \Sigma_1$

Figure 1.3. Mode matching equations for a resistive screen.

Due to the periodic nature of the problem, the total fields in all regions, except in the resistive layer, can be represented by Floquet space harmonics. Explicitly, they are given by

Transmitted region

$$\psi = \sum_{pq} T_{pq} Q_{pq}(x, y) \exp(-j\gamma_{pq}^{(5)} z) \quad (1.1.3a)$$

Dielectric layers

$$\psi = \sum_{pq} Q_{pq}(x, y) [A_{pq}^{(n)} \exp(-j\gamma_{pq}^{(n)} z) + B_{pq}^{(n)} \exp(+j\gamma_{pq}^{(n)} z)] \quad (1.1.3b)$$

Incident region

$$\psi = \sum_{pq} Q_{pq}(x, y) [I_{pq} \exp(-j\gamma_{pq}^{(26)} z) + R_{pq} \exp(+j\gamma_{pq}^{(26)} z)] \quad (1.1.3c)$$

Here the summation indices (p, q) take the values

$$p, q = 0, \pm 1, \pm 2, \dots$$

The factor Q_{pq} describes the transverse variation of the (p, q)th space harmonics:

$$Q_{pq}(x, y) = \exp[-j(u_{po}x + x_{pq}y)] \quad (1.1.5)$$

where

$$u_{po} = (2p\pi/a) + k_0 \sqrt{\mu_{26}\epsilon_{26}} \sin \theta_0 \cos \phi_0 \quad (1.1.6)$$

$$v_{pq} = (-2p\pi/a \tan \Omega) + (2q\pi/b) + k_0 \sqrt{\mu_{26}\epsilon_{26}} \sin \theta_0 \cos \phi_0 \quad (1.1.7)$$

The propagation constants in (2.3) are defined by

$$\gamma_{pq}^{(n)} = [k_0^2 \mu_n \epsilon_n - (u_{po}^2 + v_{pq}^2)]^{1/2}, \quad n = 1, 2, \dots, 10 \quad (1.1.8a)$$

where the square roots are taken such that

$$\operatorname{Re} \gamma_{pq}^{(n)} \geq 0, \quad \operatorname{Im} \gamma_{pq}^{(n)} \leq 0 \quad (1.1.8b)$$

For given incident field (I_{pq}, \bar{I}_{pq}) , the unknown modal coefficients $\{T_{pq}, A_{pq}^{(n)}, \dots, R_{pq}\}$ are to be determined. In addition to the TE modes described in (1.1.3), TM modes exist in the various other regions. They are derivable from $\bar{\psi}$ in accordance with (1.1.2). We represent $\bar{\psi}$ in the same manner as in (1.1.3) except that the constants $\{T_{pq}, A_{pq}^{(n)}, \dots, R_{pq}\}$ are replaced by $\{\bar{T}_{pq}, A_{pq}^{(n)}, \dots, R_{pq}\}$.

1.2. Fields at the Interface

We use the same field representations given in Section 2, 79-Rept. The tangential fields just below the R-sheet are (Appendix C)

$$\begin{aligned} \mathbf{E}_t(z=0-) = \sum_{pq} \sum_j w_{pq} Q_{pq}(x, y) \{ & (\hat{\alpha}_{pq} [(\rho_{pq}^{(1)} + \rho_{pq}^{(3)}) I_{pq} + (\rho_{pq}^{(2)} + \rho_{pq}^{(4)}) R_{pq}] \\ & + (\gamma_{pq}^{(6)}/k_0 \epsilon_6) \hat{\beta}_{pq} [(\bar{\rho}_{pq}^{(1)} - \bar{\rho}_{pq}^{(3)}) \bar{I}_{pq} + (\bar{\rho}_{pq}^{(2)} - \bar{\rho}_{pq}^{(4)}) \bar{R}_{pq}] \} \end{aligned} \quad (1.2.1)$$

$$\begin{aligned} \mathbf{H}_t(z=0-) = \sum_{pq} \sum_j w_{pq} Q_{pq}(x, y) \{ & (\gamma_{pq}^{(6)}/k_0 Z_0 \mu_6) \hat{\beta}_{pq} [(\rho_{pq}^{(1)} - \rho_{pq}^{(3)}) I_{pq} \\ & + (\rho_{pq}^{(2)} - \rho_{pq}^{(4)}) R_{pq}] + (-1/Z_0) \hat{\alpha}_{pq} [(\bar{\rho}_{pq}^{(1)} + \bar{\rho}_{pq}^{(3)}) \bar{I}_{pq} \\ & + (\bar{\rho}_{pq}^{(2)} + \bar{\rho}_{pq}^{(4)}) \bar{R}_{pq}] \} \end{aligned} \quad (1.2.2)$$

where

$$\hat{\alpha}_{pq} = w_{pq}^{-1} (\hat{x} v_{pq} - \hat{y} u_{pq}) = -\hat{z} \times \hat{\beta}_{pq} \quad (1.2.3a)$$

$$\hat{\beta}_{pq} = w_{pq}^{-1} (\hat{x} u_{pq} + \hat{y} v_{pq}) = \hat{z} \times \hat{\alpha}_{pq} \quad (1.2.3b)$$

$$w_{pq} = \sqrt{u_{po}^2 + v_{pq}^2} \quad (1.2.3c)$$

$$\phi_{pq} = \tan^{-1} (v_{pq}/u_{po}) \quad (1.2.3d)$$

$$p = 0, \pm 1, \pm 2, \dots, \pm P \quad (1.2.4a)$$

$$q = 0, \pm 1, \pm 2, \dots, \pm Q \quad (1.2.4b)$$

From (1.2.4) we note that the total number of Floquet space harmonics used in our computation is

$$NF = 2 (2P + 1) (2Q + 1) \quad (1.2.4c)$$

The tangential fields just above the R-sheet are

$$\begin{aligned} \mathbf{E}_t(z = 0+) = \sum_{pq} \sum_j w_{pq} Q_{pq}(x, y) \{ \hat{\alpha}_{pq} (\rho_{pq}^{(5)} + \rho_{pq}^{(6)}) T_{pq} \\ + (\gamma_{pq}^{(1)}/k_0 \epsilon_1) \hat{\beta}_{pq} (\bar{\rho}_{pq}^{(5)} - \bar{\rho}_{pq}^{(6)}) \bar{T}_{pq} \} \end{aligned} \quad (1.2.5)$$

$$\begin{aligned} \mathbf{H}_t(z = 0+) = \sum_{pq} \sum_j w_{pq} Q_{pq}(x, y) \{ (\gamma_{pq}^{(1)}/k_0 Z_0 \mu_1) \hat{\beta}_{pq} (\rho_{pq}^{(5)} - \rho_{pq}^{(6)}) T_{pq} \\ + (-1/Z_0) \hat{\alpha}_{pq} (\bar{\rho}_{pq}^{(5)} + \bar{\rho}_{pq}^{(6)}) \bar{T}_{pq} \} \end{aligned} \quad (1.2.6)$$

Next, let us consider the representation of the unknown surface current on the resistive Σ_1 .

Note that, regardless of the value of R_c , the current \mathbf{J}_s satisfies the same boundary condition that

$$\text{Normal component of } \mathbf{J}_s = 0 \quad (1.2.7)$$

at the rim of the circular plate. In the special case in which $R_c = 0$ (perfectly conducting plate), \mathbf{J}_s is given by the well-known expression

$$\mathbf{J}_s(z=0) = \frac{2}{Z_0} \hat{\mathbf{z}} \times \mathbf{E}_{\text{ind}}(z=0) \quad (1.2.8)$$

where

$$\begin{aligned} \mathbf{E}_{\text{ind}}(z=0) = & \text{Tangential electric field in the circular aperture of a} \\ & \text{complementary (inducting) screen when } R_c = 0 \\ = & \sum_{mn} \sum \left\{ (C_{mn}^V + D_{mn}^V) \mathbf{U}_{mn}^V + (C_{mn}^H + D_{mn}^H) \mathbf{U}_{mn}^H \right. \\ & \left. + \left(\frac{\bar{\Gamma}_{mn}}{k_0 \epsilon_c} \right) (\bar{C}_{mn}^V - \bar{D}_{mn}^V) \mathbf{V}_{mn}^V + \left(\frac{\bar{\Gamma}_{mn}}{k_0 \epsilon_c} \right) (\bar{C}_{mn}^H - \bar{D}_{mn}^H) \mathbf{V}_{mn}^H \right\} \end{aligned} \quad (1.2.9)$$

The representation in (1.2.8) is based on the Babinet principle that

$$Z_0 \mathbf{E}_{\text{ind}}(z=0) \rightarrow \mathbf{H}_{\text{cap}}(z=0+) \text{ or } \mathbf{H}_{\text{cap}}(z=0-)$$

and the fact that

$$\mathbf{J}_s(z=0) = \hat{\mathbf{z}} \times [\mathbf{H}_{\text{cap}}(0+) - \mathbf{H}_{\text{cap}}(0-)]$$

Because of (1.2.7), the same representation (1.2.8) for the conducting case can still be used for the present resistive case.

The summation in (1.2.9) represents the superposition of fields on four rings. Let us concentrate on the field on a typical ring. As explained in Appendix A, the assumption of narrow ring width allows us to use a simplified modal field representation, namely,

$$\begin{aligned} \mathbf{U}_m^{V,H} &= \hat{\rho} \frac{1}{\rho} \left[\frac{\Delta_m 60}{\ln(d/c)} \right]^{1/2} \begin{bmatrix} \sin m\phi \\ -\cos m\phi \end{bmatrix} \\ \mathbf{V}_m^{V,H} &= 0 \end{aligned}$$

In another code “ring2c,” we used the exact coaxial waveguide modes to represent the field on the rings. For narrow rings, there is virtually no difference in their solutions.

Our problem at hand is to determine NF transmission coefficients $\{T_{pq}, \bar{T}_{pq}\}$ and NG reflection coefficients $\{R_{pq}, \bar{R}_{pq}\}$, for a given set of incidence coefficients $\{I_{pq}, \bar{I}_{pq}\}$. In the present formulation, we determine aperture-field coefficients $\{C_{mn} + D_{mn}, \bar{C}_{mn} - \bar{D}_{mn}\}$ as an intermediate step.

1.3. Field Matching at $z = 0$

There are three boundary conditions to be satisfied. The first one is

$$\mathbf{E}_{\tan}(z = 0-) = \mathbf{E}(z = 0+), \quad \text{in } \Sigma_1 + \Sigma_2 \quad (1.3.1)$$

where

Σ_1 = resistive circular plate

Σ_2 = remaining portion in a unit cell.

We multiple both sides of (1.3.1) by the operator

$$\int_{-a/2}^{a/2} dx \int_{-b/2}^{b/2} dy \quad \exp j(u_{po}x + v_{pq}y) \quad (1.3.2)$$

We obtain

$$T_{pq} = \frac{\rho_{pq}^{(2)} + \rho_{pq}^{(4)}}{\rho_{pq}^{(5)} + \rho_{pq}^{(6)}} R_{pq} + \frac{\rho_{pq}^{(1)} + \rho_{pq}^{(3)}}{\rho_{pq}^{(5)} + \rho_{pq}^{(6)}} I_{pq} \quad (1.3.3)$$

$$\bar{T}_{pq} = \left[\frac{\bar{\rho}_{pq}^{(2)} - \bar{\rho}_{pq}^{(4)}}{\bar{\rho}_{pq}^{(5)} - \bar{\rho}_{pq}^{(6)}} \bar{R}_{pq} + \frac{\bar{\rho}_{pq}^{(1)} - \bar{\rho}_{pq}^{(3)}}{\bar{\rho}_{pq}^{(5)} - \bar{\rho}_{pq}^{(6)}} \bar{I}_{pq} \right] \begin{bmatrix} \epsilon_1 \gamma_{pq}^{(6)} \\ \epsilon_6 \gamma_{pq}^{(1)} \end{bmatrix} \quad (1.3.4)$$

which relate the transmission coefficients to the reflection coefficients.

The second boundary condition is

$$\mathbf{J}_s(\text{outside}) = \begin{cases} \mathbf{J}_s(0) & , \quad \text{in } \Sigma_1 \\ 0 & , \quad \text{in } \Sigma_2 \end{cases} \quad (1.3.5)$$

Here $\mathbf{J}_s(0)$ is the induced current on the resistive circular plate and is given in (1.2.7). The current $\mathbf{J}_s(\text{outside})$ is that calculated from the discontinuity of the tangential \mathbf{H} -field outside the resistive plate, namely,

$$\mathbf{J}_s(\text{outside}) = \hat{\mathbf{z}} \times [\mathbf{H}_t(0+) - \mathbf{H}_t(0-)], \quad \text{in } \Sigma_1 + \Sigma_2 \quad (1.3.6)$$

We will now consider the enforcement of (1.3.5) in detail. Substituting (1.2.2) and (1.2.6) into (1.3.6) gives

$$\begin{aligned} \mathbf{J}_s(\text{outside}) = & \left(\frac{2}{Z_0} \right) \sum_{pq} j w_{pq} Q_{pq}(x, y) \left\{ \hat{\alpha}_{pq} F_{pq}^{(3)} [(\rho_{pq}^{(1)} + \rho_{pq}^{(3)}) I_{pq} + (\rho_{pq}^{(2)} + \rho_{pq}^{(4)}) R_{pq}] \right. \\ & \left. + \hat{\alpha}_{pq} F_{pq}^{(4)} I_{pq} + \hat{\beta}_{pq} \bar{F}_{pq}^{(3)} [(\bar{\rho}_{pq}^{(1)} - \bar{\rho}_{pq}^{(3)}) \bar{I}_{pq} + (\bar{\rho}_{pq}^{(2)} - \bar{\rho}_{pq}^{(4)}) \bar{R}_{pq}] + \hat{\beta}_{pq} \bar{F}_{pq}^{(4)} \bar{I}_{pq} \right\} \end{aligned} \quad (1.3.7)$$

where

$$\begin{aligned} F_{pq}^{(3)} &= \left(\frac{-1}{2} \right) \left(\frac{\gamma_{pq}^{(1)}}{k_0 \mu_1} \right) \frac{\rho_{pq}^{(5)} - \rho_{pq}^{(6)}}{\rho_{pq}^{(5)} + \rho_{pq}^{(6)}} + \frac{1}{2} \left(\frac{\gamma_{pq}^{(6)}}{k_0 \mu_6} \right) \frac{\rho_{pq}^{(2)} - \rho_{pq}^{(4)}}{\rho_{pq}^{(2)} + \rho_{pq}^{(4)}} \\ &= \frac{1}{2} [\chi_{pq}^{(2)} - \chi_{pq}^{(5)}] \end{aligned} \quad (1.3.8)$$

$$F_{pq}^{(4)} = \frac{\gamma_{pq}^{(6)}}{2k_0\mu_6} \left[(\rho_{pq}^{(1)} - \rho_{pq}^{(3)}) - (\rho_{pq}^{(1)} + \rho_{pq}^{(3)}) \frac{\rho_{pq}^{(2)} - \rho_{pq}^{(4)}}{\rho_{pq}^{(2)} + \rho_{pq}^{(4)}} \right] \quad (1.3.9)$$

$$= \frac{1}{2} \frac{1}{w_{pq}} \chi_{pq}^{(1)}$$

$$\bar{F}_{pq}^{(3)} = \frac{1}{2} \frac{\bar{\rho}_{pq}^{(2)} + \bar{\rho}_{pq}^{(4)}}{\bar{\rho}_{pq}^{(2)} - \bar{\rho}_{pq}^{(4)}} - \frac{1}{2} \left(\frac{\epsilon_1 \gamma_{pq}^{(6)}}{\epsilon_6 \gamma_{pq}^{(1)}} \right) \frac{\bar{\rho}_{pq}^{(5)} + \bar{\rho}_{pq}^{(6)}}{\bar{\rho}_{pq}^{(5)} - \bar{\rho}_{pq}^{(6)}} \quad (1.3.10)$$

$$= \frac{1}{2} \left(\frac{\gamma_{pq}^{(6)}}{k_0 \epsilon_6} \right) [\bar{\chi}_{pq}^{(2)} - \bar{\chi}_{pq}^{(5)}]$$

$$\bar{F}_{pq}^{(4)} = \frac{1}{2} \left[(\bar{\rho}_{pq}^{(1)} + \bar{\rho}_{pq}^{(3)}) - (\bar{\rho}_{pq}^{(1)} - \bar{\rho}_{pq}^{(3)}) \frac{\bar{\rho}_{pq}^{(2)} + \bar{\rho}_{pq}^{(4)}}{\bar{\rho}_{pq}^{(2)} - \bar{\rho}_{pq}^{(4)}} \right] \quad (1.3.11)$$

$$= \frac{1}{2} \frac{1}{w_{pq}} \chi_{pq}^{(1)}$$

In deriving (1.3.7), we have made use of (1.3.3) and (1.3.4). We multiply both sides of (1.3.5) by

$$\int_{-a/2}^{a/2} dx \int_{-b/2}^{b/2} dy [\exp j(u_{po}x + v_{pq}y)] [w_{pq}] \begin{bmatrix} \hat{\alpha}_{pq} & \cdot \\ \hat{\beta}_{pq} & \cdot \end{bmatrix} \quad (1.3.12)$$

We obtain

$$\begin{aligned} & j \text{ ab } w_{pq}^2 \left\{ [(\rho_{pq}^{(1)} + \rho_{pq}^{(3)}) I_{pq} + (\rho_{pq}^{(2)} + \rho_{pq}^{(4)}) R_{pq}] F_{pq}^{(3)} + I_{pq} F_{pq}^{(4)} \right\} \\ & = \sum_{mn} \left[-X_{pqmn}^{(3)V} (C_{mn}^V + D_{mn}^V) - X_{pqmn}^{(3)H} (C_{mn}^H + D_{mn}^H) \right. \\ & \quad \left. - X_{pqmn}^{(4)V} (\bar{C}_{mn}^V - \bar{D}_{mn}^V) - X_{pqmn}^{(4)H} (\bar{C}_{mn}^H - \bar{D}_{mn}^H) \right] \end{aligned} \quad (1.3.13)$$

$$\begin{aligned}
& j \text{ ab } w_{pq}^2 \left\{ \left[(\bar{\rho}_{pq}^{(1)} - \bar{\rho}_{pq}^{(3)}) \bar{I}_{pq} + (\bar{\rho}_{pq}^{(2)} - \bar{\rho}_{pq}^{(4)}) \bar{R}_{pq} \right] \bar{F}_{pq}^{(3)} + \bar{I}_{pq} F_{pq}^{(4)} \right\} \\
& = \Sigma \Sigma \left[X_{pqmn}^{(1)V} (C_{mn}^V + D_{mn}^V) + X_{pqmn}^{(1)H} (C_{mn}^H + D_{mn}^H) \right] \quad (1.3.14)
\end{aligned}$$

where

$$\begin{bmatrix} X_{pqmn}^{(1)V} \\ X_{pqmn}^{(1)H} \end{bmatrix} = -j w_{pq} \sigma_{pqmn}^{(1)} \begin{bmatrix} \cos m \phi_{pq} \\ \sin m \phi_{pq} \end{bmatrix}$$

$$\begin{bmatrix} X_{pqmn}^{(3)V} \\ X_{pqmn}^{(3)H} \end{bmatrix} = -j w_{pq} \sigma_{pqmn}^{(3)} \begin{bmatrix} \sin m \phi_{pq} \\ -\cos m \phi_{pq} \end{bmatrix}$$

$$\begin{bmatrix} X_{pqmn}^{(4)V} \\ X_{pqmn}^{(4)H} \end{bmatrix} = -j w_{pq} \left(\frac{\bar{\Gamma}_{mn}}{k_0 \epsilon_c} \right) \sigma_{pqmn}^{(4)} \begin{bmatrix} \sin m \phi_{pq} \\ \cos m \phi_{pq} \end{bmatrix}$$

$$\left. \begin{matrix} \sigma_{pqmn}^{(1)} \\ \sigma_{pqmn}^{(3)} \end{matrix} \right\} \text{ given in Appendix B}$$

$$\sigma_{pqmn}^{(4)} = 0$$

In deriving (1.3.13) and (1.3.14), we have made use of the fact that

$$\hat{z} \times \mathbf{A} \cdot \hat{\boldsymbol{\alpha}}_{pq} = -\mathbf{A} \cdot \hat{\boldsymbol{\beta}}_{pq} \quad (1.3.15a)$$

$$\hat{z} \times \mathbf{A} \cdot \hat{\boldsymbol{\beta}}_{pq} = \mathbf{A} \cdot \hat{\boldsymbol{\alpha}}_{pq} \quad (1.3.15b)$$

From (1.3.13) and (1.3.14) we can solve for $\{R_{pq}, \bar{R}_{pq}\}$ in terms of $\{C_{mn}^V, D_{mn}^V, \dots\}$. The results are

$$R_{pq} = -\frac{\rho_{pq}^{(1)} + \rho_{pq}^{(3)}}{\rho_{pq}^{(2)} + \rho_{pq}^{(4)}} I_{pq} - \frac{F_{pq}^{(4)}}{F_{pq}^{(3)} (\rho_{pq}^{(2)} + \rho_{pq}^{(4)})} I_{pq} \quad (1.3.16)$$

$$+ \frac{(-1/F_{pq}^{(3)})}{j\omega w_{pq}^2 (\rho_{pq}^{(2)} + \rho_{pq}^{(4)})} = \sum_{mn} \sum \left\{ X_{pqmn}^{(3)V} (C_{mn}^V + D_{mn}^V) + X_{pqmn}^{(4)V} (\bar{C}_{mn}^V - \bar{D}_{mn}^V) \right. \\ \left. + X_{pqmn}^{(3)H} (C_{mn}^H + D_{mn}^H) + X_{pqmn}^{(4)H} (\bar{C}_{mn}^H - \bar{D}_{mn}^H) \right\}$$

$$\bar{R}_{pq} = -\frac{\bar{\rho}_{pq}^{(1)} - \bar{\rho}_{pq}^{(3)}}{\bar{\rho}_{pq}^{(2)} - \bar{\rho}_{pq}^{(4)}} \bar{I}_{pq} - \frac{\bar{F}_{pq}^{(4)}}{\bar{F}_{pq}^{(3)} (\bar{\rho}_{pq}^{(2)} - \bar{\rho}_{pq}^{(4)})} \bar{I}_{pq} \quad (1.3.17)$$

$$+ \frac{(-1/\bar{F}_{pq}^{(3)})}{j\omega w_{pq}^2 (\bar{\rho}_{pq}^{(2)} - \bar{\rho}_{pq}^{(4)})} = \sum_{mn} \sum \left\{ X_{pqmn}^{(1)V} (C_{mn}^V + D_{mn}^V) + X_{pqmn}^{(1)H} (C_{mn}^H + D_{mn}^H) \right\}$$

So far we have expressed the transmission and reflection coefficients in terms of unknown current coefficients

$$\{ C_{mn}^V, D_{mn}^V, C_{mn}^H, D_{mn}^H, \bar{C}_{mn}^V, \bar{D}_{mn}^V, \bar{C}_{mn}^H, \bar{D}_{mn}^H \} \quad (1.3.18)$$

Those expressions are independent of the resistivity R_c .

The third and the last boundary condition to be enforced is

$$\mathbf{E}_t(z=0-) = R_c \mathbf{J}_s(0), \quad \text{in } \Sigma_1 \quad (1.3.19)$$

where \mathbf{E}_t is given in (1.2.1), and \mathbf{J}_s in (1.2.8). Multiply both sides of (1.3.19) by

$$\int_0^d \rho d\rho \int_0^{2\pi} d\phi \begin{bmatrix} \hat{\mathbf{z}} \times \mathbf{U}_{mn}^{V,H} \\ \hat{\mathbf{z}} \times \mathbf{V}_{mn}^{V,H} \end{bmatrix} \quad (1.3.20)$$

we obtain

$$\sum_{pq} \sum \left\{ \begin{bmatrix} -X_{pq/lw}^{(3)V} \\ -X_{pq/lw}^{(3)H} \end{bmatrix} R'_{pq} + \left(\frac{\gamma_{pq}^{(6)}}{k_0 \epsilon_6} \right) \begin{bmatrix} X_{pq/lw}^{(1)V} \\ X_{pq/lw}^{(1)H} \end{bmatrix} \bar{R}'_{pq} \right\} \quad (1.3.21)$$

$$= (-j)(-1)^{l-1} \eta Z_0 \begin{bmatrix} C_{lw}^V + D_{lw}^V \\ C_{lw}^H + D_{lw}^H \end{bmatrix}$$

$$\sum_{pq} \sum \left\{ \begin{bmatrix} -X_{pq/lw}^{(4)V} \\ -X_{pq/lw}^{(4)H} \end{bmatrix} R'_{pq} \right\} = (-j)(-1)^{l-1} \eta Z_0 + \left(\frac{\bar{\Gamma}_{lw}}{k_0 \epsilon_c} \right)^2 \begin{bmatrix} \bar{C}_{lw}^V - \bar{D}_{lw}^V \\ \bar{C}_{lw}^H - \bar{D}_{lw}^H \end{bmatrix} \quad (1.3.22)$$

where

$$R'_{pq} = (\rho_{pq}^{(1)} + \rho_{pq}^{(3)}) I_{pq} + (\rho_{pq}^{(2)} + \rho_{pq}^{(4)}) R_{pq}$$

$$\bar{R}'_{pq} = (\bar{\rho}_{pq}^{(1)} - \bar{\rho}_{pq}^{(3)}) \bar{I}_{pq} + (\bar{\rho}_{pq}^{(2)} - \bar{\rho}_{pq}^{(4)}) \bar{R}_{pq}$$

Substituting (1.3.16) and (1.3.17) into (1.3.21) and (1.3.22), we obtain the desired matrix equation.

$$\bar{\bar{X}}' C' = G' \quad (1.3.23)$$

Here

$$\bar{\bar{X}}' = \begin{bmatrix} t_{lmn}^{(1)V} & t^{(1)H} & \bar{t}^{(1)V} & \bar{t}^{(1)H} \\ t^{(3)V} & t^{(3)H} & \bar{t}^{(3)V} & \bar{t}^{(3)H} \\ t^{(5)V} & t^{(5)H} & \bar{t}^{(5)V} & \bar{t}^{(5)H} \\ t^{(7)V} & t^{(7)H} & \bar{t}^{(7)V} & \bar{t}^{(7)H} \end{bmatrix}$$

$$C' = \begin{bmatrix} C_{mn}^V + D_{mn}^V \\ C_{mn}^H + D_{mn}^H \\ \bar{C}_{mn}^V - \bar{D}_{mn}^V \\ \bar{C}_{mn}^H - \bar{D}_{mn}^H \end{bmatrix} \quad \bar{\bar{G}}' = \begin{bmatrix} g_{lw}^{(1)} \\ g_{lw}^{(2)} \\ g_{lw}^{(3)} \\ g_{lw}^{(4)} \end{bmatrix}$$

The explicit expressions of $\bar{\bar{X}}'$ and $\bar{\bar{G}}'$ are given below.

$$\begin{aligned} \begin{bmatrix} t_{lwmn}^{(1)V,H} \\ t_{lwmn}^{(3)V,H} \end{bmatrix} &= \frac{1}{ab} \sum_{pq} \left\{ \left(\frac{j}{w_{pq}} \right) \frac{1}{F_{pq}^{(3)}} X_{pqmn}^{(3)V,H} \sigma_{pqmn}^{(3)} \begin{bmatrix} \sin m \phi_{pq} \\ -\cos m \phi_{pq} \end{bmatrix} \right. \\ &\quad \left. + \left(\frac{\gamma_{pq}^{(6)}}{k_0 \epsilon_6} \right) \left(\frac{j}{w_{pq}} \right) \frac{1}{\bar{F}_{pq}^{(3)}} X_{pqmn}^{(1)V,H} \sigma_{pqmn}^{(1)} \begin{bmatrix} \cos m \phi_{pq} \\ \sin m \phi_{pq} \end{bmatrix} \right\} \\ &\quad + \delta_l^m \delta_w^n (-1)^{l-1} \eta Z_0 \end{aligned} \quad (1.3.24a)$$

$$\begin{bmatrix} \bar{t}_{lwmn}^{(1)V,H} \\ \bar{t}_{lwmn}^{(3)V,H} \end{bmatrix} = \text{Same as } \begin{bmatrix} t^{(1)} \\ t^{(3)} \end{bmatrix} \text{ except } \left\{ \begin{array}{l} X^{(3)} \rightarrow X^{(4)} \\ X^{(1)} \rightarrow 0 \\ \text{no diagonal term} \end{array} \right\} \quad (1.3.24b)$$

$$\begin{bmatrix} t_{lwmn}^{(5)V,H} \\ t_{lwmn}^{(7)V,H} \end{bmatrix} = \text{Same as } \begin{bmatrix} \bar{t}^{(5)} \\ \bar{t}^{(7)} \end{bmatrix} \text{ except } \left\{ \begin{array}{l} X^{(4)} \rightarrow X^{(3)} \\ \text{no diagonal term} \end{array} \right\} \quad (1.3.24c)$$

$$\begin{aligned}
\begin{bmatrix} \bar{t}_{lwmn}^{(5)V,H} \\ \bar{t}_{lwmn}^{(7)V,H} \end{bmatrix} &= \frac{1}{ab} \sum_{pq} \left\{ \left(\frac{j}{w_{pq}} \right) \frac{1}{F_{pq}^{(3)}} X_{pqmn}^{(4)V,H} \sigma_{pq/w}^{(4)} \begin{bmatrix} \sin m \phi_{pq} \\ \cos m \phi_{pq} \end{bmatrix} \right\} \\
&+ \delta_l^m \delta_w^n (-1)^{l-1} \eta Z_0 (\bar{\Gamma}_{lw}/k_0 \epsilon_c)
\end{aligned} \tag{1.3.24d}$$

$$\begin{aligned}
\begin{bmatrix} g_{lw}^{(1)} \\ g_{lw}^{(2)} \end{bmatrix} &= \sum_{pq} \left\{ \begin{bmatrix} \sin m \phi_{pq} \\ -\cos m \phi_{pq} \end{bmatrix} w_{pq} \sigma_{pq/w}^{(3)} (F_{pq}^{(4)} / F_{pq}^{(3)}) I_{pq} \right. \\
&\left. + \begin{bmatrix} \cos m \phi_{pq} \\ \sin m \phi_{pq} \end{bmatrix} w_{pq} \sigma_{pq/w}^{(1)} (-\bar{F}_{pq}^{(4)} / \bar{F}_{pq}^{(3)}) (\gamma_{pq}^{(6)} / k_0 \epsilon_6) \bar{I}_{pq} \right\}
\end{aligned}$$

$$\begin{bmatrix} g_{lw}^{(3)} \\ g_{lw}^{(4)} \end{bmatrix} = \sum_{pq} \left\{ \begin{bmatrix} \sin m \phi_{pq} \\ \cos m \phi_{pq} \end{bmatrix} w_{pq} \sigma_{pq/w}^{(4)} (F_{pq}^{(4)} / F_{pq}^{(3)}) I_{pq} \right\}$$

In summary, the final matrix equation is in (1.3.23) for the unknown coefficients $\{C'\}$. Once $\{C'\}$ are solved, the reflection coefficients are calculated from (1.3.16) and (1.3.17), and the transmission coefficients from (1.3.3) and (1.3.4).

Appendix A: Modes on a Narrow Ring

To determine the modal field on a metal ring, we may consider its complementary problem, the modal field on a coaxial waveguide, because these two fields are related by the Babinet principle. Consider a coaxial waveguide shown in Figure A.1. Its normal modes can be found in a standard textbook (e.g., N. Marcuvitz, *Waveguide Handbook*, New York: McGraw-Hill, 1949, pp. 72-80). They are given in terms of Bessel functions and are rather complicated. Under the condition of narrow gap that

$$\frac{d-c}{c} \ll 1 \quad (\text{A.1})$$

we can use a set of simple and approximated modes to be deduced below.

Consider the field in the neighborhood of Q in the coaxial waveguide. Under the condition (A.1), it can be well approximated by that in a slot waveguide on the right-hand side of Figure A.1. The fields in the latter are expressible in terms of two vector potentials, namely,

$$\text{TE modes:} \quad \psi = A_{mn} \begin{bmatrix} \cos \frac{2m\pi}{2\pi d} x' \\ \sin \frac{2m\pi}{2\pi d} x' \end{bmatrix} \cos \frac{n\pi}{\delta} \left(y' + \frac{\delta}{2} \right) e^{\pm j\Gamma_{mn}z} \quad (\text{A.2a})$$

$$\text{TM modes:} \quad \bar{\psi} = \bar{A}_{mn} \begin{bmatrix} \cos \frac{2m\pi}{2\pi d} x' \\ \sin \frac{2m\pi}{2\pi d} x' \end{bmatrix} \sin \frac{n\pi}{\delta} \left(y' + \frac{\delta}{2} \right) e^{\pm j\Gamma_{mn}z} \quad (\text{A.2b})$$

where

$$\Gamma_{mn} = \sqrt{k_0^2 - \left(\frac{m}{d} \right)^2 - \left(\frac{n\pi}{\delta} \right)^2}$$

The boundary condition for the slot waveguide is that

$$(\text{Field at AB}) = (\text{Field at A'B'}) \quad (\text{A.3})$$

Figure A.1. The field in a coaxial waveguide with a narrow gap can be approximated by that in a slot waveguide.

which leads to the admission of both cosine and sine functions in (A.2). Making use of the replacement

$$x' \rightarrow d \phi \quad (\text{A.4a})$$

$$y' \rightarrow \rho - 0.5 (d + c) \quad (\text{A.4b})$$

we obtain the approximated modes in a narrow coaxial waveguide, namely,

$$\psi \approx A_{mn} \begin{bmatrix} \cos m \phi \\ \sin m \phi \end{bmatrix} \left\{ \cos \frac{n\pi}{\delta} (\rho - c) \right\} e^{\pm j \Gamma_{mn} z} \quad (\text{A.5a})$$

$$\bar{\psi} \approx \bar{A}_{mn} \begin{bmatrix} \cos m \phi \\ \sin m \phi \end{bmatrix} \left\{ \sin \frac{n\pi}{\delta} (\rho - c) \right\} e^{\pm j \Gamma_{mn} z} \quad (\text{A.5b})$$

Because of the fact that $d \rightarrow 0$, we make a further approximation by using only

$$n = 0 \quad (\text{A.6})$$

modes in (A.5), we obtain

$$\text{TE modes:} \quad \psi \approx \sum_{m=0}^{\infty} \frac{1}{m} \begin{bmatrix} \cos m \phi \\ \sin m \phi \end{bmatrix} [C_m e^{-j \Gamma_m z} + D_m e^{+j \Gamma_m z}] \quad (\text{A.7a})$$

$$\text{TM modes:} \quad \bar{\psi} \approx 0 \quad (\text{A.7b})$$

where

$$\Gamma_m = \sqrt{k_0^2 - \left(\frac{m}{d}\right)^2} \quad (\text{A.7c})$$

The non-zero field components can be calculated with the formulas

$$E_\rho = -\frac{1}{\rho} \frac{\partial \psi}{\partial \phi} \quad (\text{A.8a})$$

$$H_\phi = \frac{1}{j k_0 Z_0} \frac{1}{\rho} \frac{\partial^2 \psi}{\partial \phi \partial Z} \quad (\text{A.8b})$$

Returning to Figure A.1 let us write down a field representation at $z = 0$ for the coaxial waveguide:

$$\mathbf{E}_t(0) = \sum \{ (C_m^V + D_m^V) \mathbf{U}_m^V + (C_m^H + D_m^H) \mathbf{U}_m^H \} \quad (\text{A.9a})$$

$$\mathbf{H}_t(0) = \frac{1}{Z_0} \sum \left(\frac{\Gamma_m}{k_0} \right) \{ (C_m^V - D_m^V) (\hat{z} \times \mathbf{U}_m^V) + (C_m^H - D_m^H) (\hat{z} \times \mathbf{U}_m^H) \} \quad (\text{A.9b})$$

where

$$\mathbf{U}_m^{V,H} = \hat{\rho} \frac{1}{\rho} \left[\frac{\Delta_m Z_0}{2\pi \ln(d/c)} \right]^{1/2} \begin{bmatrix} \sin m \phi \\ -\cos m \phi \end{bmatrix}, \begin{matrix} m = 1, 2, 3, \dots \\ m = 0, 1, 2, \dots \end{matrix} \quad (\text{A.10})$$

where $Z_0 = 120 \pi$ and $\Delta_m = 1$ if $m = 0$ and $\Delta_m = 2$ if $m \neq 0$. The $m = 0$ mode is the well-known TEM mode in a coaxial waveguide. Note that $\mathbf{U}_m^{V,H}$ has been normalized such that

$$\iint_{\text{slot}} \mathbf{U}_m^{V,H} \cdot \mathbf{U}_n^{V,H} \rho d\rho d\phi = \begin{cases} Z_0, & \text{if } m = n \\ 0, & \text{if } m \neq n \end{cases} \quad (\text{A.11})$$

is satisfied.

Appendix B: Coupling Coefficients

To change (1.3.5) into a matrix equation, we apply the operation (1.3.12) to both sides of the equation. The resultant equation is given in (1.3.13) and (1.3.14). In this appendix, we give the details of deriving the coefficients $\{X_{pqmn}\}$.

Applying (1.3.12) to the right-hand side of (1.3.5), the integral is reduced to 4 integrals over the 4 metal rings, namely,

$$\int_{\text{over cell axb}} = \sum_{4 \text{ rings}} \int_{\text{over a ring}}$$

In the following, let us concentrate on a typical ring with outer and inner radii (d,c):

$$\begin{bmatrix} X_{pqm}^{(1)V,H} \\ X_{pqm}^{(3)V,H} \end{bmatrix} = \iint_{\text{slot}} \rho d\rho d\phi e^{j(u_{po}x + v_{pq}y)} w_{pq} \begin{bmatrix} \hat{\alpha}_{pq} \\ \hat{\beta}_{pq} \end{bmatrix} \cdot U_m^{V,H} \quad (\text{B.1})$$

where $U_m^{V,H}$ are given (A.10), and

$$\hat{\alpha}_{pq} = w_{pq}^{-1} (\hat{x} v_{pq} - \hat{y} u_{po}) = -\hat{z} \times \hat{\beta}_{pq} \quad (\text{B.2a})$$

$$\hat{\beta}_{pq} = w_{pq}^{-1} (\hat{x} u_{po} + \hat{y} v_{pq}) = \hat{z} \times \hat{\alpha}_{pq} \quad (\text{B.2b})$$

The final results after evaluating (B.1) are

$$\begin{bmatrix} X_{pqm}^{(1)V} \\ X_{pqm}^{(1)H} \end{bmatrix} = -j w_{pq} \sigma_{pqm}^{(1)} \begin{bmatrix} \cos m \phi_{pq} \\ \sin m \phi_{pq} \end{bmatrix} \quad (\text{B.3})$$

$$\begin{bmatrix} X_{pqm}^{(3)V} \\ X_{pqm}^{(3)H} \end{bmatrix} = -j w_{pq} \sigma_{pqm}^{(3)} \begin{bmatrix} \sin m \phi_{pq} \\ -\cos m \phi_{pq} \end{bmatrix} \quad (B.4)$$

where

$$\phi_{pq} = \tan^{-1} \left(\frac{v_{pq}}{u_{po}} \right)$$

$$\sigma_{pqm}^{(1)} = \left[\frac{\Delta_m Z_0}{2\pi \ln \left(\frac{d}{c} \right)} \right]^{1/2} (-2m \pi) j^m w_{pq}^{-1} \int_{w_{pq}c}^{w_{pq}d} \frac{J_m(t)}{t} dt \quad (B.5)$$

$$\sigma_{pqm}^{(3)} = \left[\frac{\Delta_m Z_0}{2\pi \ln \left(\frac{d}{c} \right)} \right]^{1/2} (2\pi) j^m w_{pq}^{-1} [J_m(w_{pq}d) - J_m(w_{pq}c)] \quad (B.6)$$

The derivation of (B.5) is given below. From (B.1) we have

$$\begin{bmatrix} X_{pqm}^{(1)V} \\ X_{pqm}^{(1)H} \end{bmatrix} = C \int d\rho \int d\phi e^{j w_{pq}\rho \cos(\phi - \phi_{pq})} \begin{bmatrix} \sin m \phi \\ -\cos m \phi \end{bmatrix} \cdot (-1) w_{pq} \sin(\phi - \phi_{pq}) \quad (B.7)$$

where

$$C = \left(\frac{\Delta_m Z_0}{2\pi \cdot (\ln d - \ln c)} \right)^{1/2}$$

Using the identity in (B.7)

$$\sin m \phi = \cos m \phi_{pq} \cdot \sin m(\phi - \phi_{pq}) + \sin m \phi_{pq} \cdot \cos m(\phi - \phi_{pq})$$

$$\cos m \phi = \cos m \phi_{pq} \cdot \cos m(\phi - \phi_{pq}) - \sin m \phi_{pq} \cdot \sin m(\phi - \phi_{pq})$$

we obtain

$$\begin{bmatrix} X_{pqm}^{(1)V} \\ X_{pqm}^{(1)H} \end{bmatrix} = C \int_c^d d\rho \int_0^\pi d\phi' (-w_{pq}) \begin{bmatrix} \cos m \phi_{pq} \\ \sin m \phi_{pq} \end{bmatrix} \cdot [\cos(m-1) \phi' - \cos(m+1) \phi'] e^{j w_{pq}\rho \cos \phi'} \quad (B.8)$$

where

$$\phi' = \phi - \phi_{pq}$$

The integral with respect to ϕ' can be written in terms of Bessel functions, namely,

$$\begin{aligned} \begin{bmatrix} X_{pqm}^{(1)V} \\ X_{pqm}^{(1)H} \end{bmatrix} &= -C w_{pq} \begin{pmatrix} \cos m \phi_{pq} \\ \sin m \phi_{pq} \end{pmatrix} \pi(j)^{m-1} \cdot \int_c^d d\rho [J_{m-1}(w_{pq} \rho) + J_{m+1}(w_{pq} \rho)] \\ &= -C (2 m \pi) j^{(m-1)} \begin{pmatrix} \cos m \phi_{pq} \\ \sin m \phi_{pq} \end{pmatrix} \cdot \int_{w_{pq}c}^{w_{pq}d} \frac{J_m(t)}{t} dt \end{aligned}$$

which is identical to (B.3) and (B.5).

Appendix C: Field Expression in (1.2.1)

The field just below the R-sheet is the field at $z = 0^-$ in region 6 (Figure 1.1). The modal coefficient in region 6 is $\{A_{pq}^{(6)}, B_{pq}^{(6)}\}$. By matching the fields at the dielectric interfaces between layers 6 to 26, we obtain

$$\begin{aligned} A_{pq}^{(6)} &= \rho_{pq}^{(1)} I_{pq} + \rho_{pq}^{(2)} R_{pq} \\ B_{pq}^{(6)} &= \rho_{pq}^{(3)} I_{pq} + \rho_{pq}^{(4)} R_{pq} \\ \bar{A}_{pq}^{(6)} &= \bar{\rho}_{pq}^{(1)} \bar{I}_{pq} + \bar{\rho}_{pq}^{(2)} \bar{R}_{pq} \\ \bar{B}_{pq}^{(6)} &= \bar{\rho}_{pq}^{(3)} \bar{I}_{pq} + \bar{\rho}_{pq}^{(4)} \bar{R}_{pq} \end{aligned} \quad (C.1)$$

To define the coefficients $\{\rho_{pq}^{(1)}, \bar{\rho}_{pq}^{(1)}, \dots\}$, let us introduce the 2×2 matrices, for $n = 1, 2, \dots, 26$,

$$F_{pq}^{(n)}(z) = \begin{bmatrix} e^{-j\gamma_{pq}^{(n)}z} & e^{+j\gamma_{pq}^{(n)}z} \\ \gamma_{pq}^{(n)} e^{-j\gamma_{pq}^{(n)}z} & -\gamma_{pq}^{(n)} e^{+j\gamma_{pq}^{(n)}z} \end{bmatrix} \quad (C.2a)$$

$$\bar{F}_{pq}^{(n)}(z) = \begin{bmatrix} e^{-j\gamma_{pq}^{(n)}z} & e^{+j\gamma_{pq}^{(n)}z} \\ \frac{1}{\epsilon_n} \gamma_{pq}^{(n)} e^{-j\gamma_{pq}^{(n)}z} & -\frac{1}{\epsilon_n} \gamma_{pq}^{(n)} e^{+j\gamma_{pq}^{(n)}z} \end{bmatrix} \quad (C.2b)$$

Then the coefficients in (C.2) are given by

$$\begin{bmatrix} \rho_{pq}^{(1)} & \rho_{pq}^{(2)} \\ \rho_{pq}^{(3)} & \rho_{pq}^{(4)} \end{bmatrix} = \prod_{n=6}^{25} [F_{pq}^{(n)}(l_n)]^{-1} F_{pq}^{(n+1)}(l_n) \quad (C.3)$$

The same equation holds for $\{\bar{\rho}_{pq}^{(1)}, \bar{\rho}_{pq}^{(2)}, \dots\}$ except that $F_{pq}^{(n)}$ is replaced by $\bar{F}_{pq}^{(n)}$.

The field in upper region 1 can be expressed in terms of that in upper region 5, namely,

$$A_{pq}^{(1)} = \rho_{pq}^{(5)} T_{pq} \exp[+j\gamma_{pq}^{(1)} \tau_c] \quad (C.4a)$$

$$B_{pq}^{(1)} = \rho_{pq}^{(6)} T_{pq} \exp[-j\gamma_{pq}^{(1)} \tau_c] \quad (C.4b)$$

$$\bar{A}_{pq}^{(1)} = \bar{\rho}_{pq}^{(5)} \bar{T}_{pq} \exp[+j\gamma_{pq}^{(1)} \tau_c] \quad (C.4c)$$

$$\bar{B}_{pq}^{(1)} = \bar{\rho}_{pq}^{(6)} \bar{T}_{pq} \exp[-j\gamma_{pq}^{(1)} \tau_c] \quad (C.4d)$$

where

τ_c = metal thickness = zero in the present capacitive FSS

$$\rho_{pq}^{(5)} = \rho_{pq}^{(7)} \exp[-j\gamma_{pq}^{(1)} \tau_c] \quad (C.5a)$$

$$\rho_{pq}^{(6)} = \rho_{pq}^{(9)} \exp[+j\gamma_{pq}^{(1)} \tau_c] \quad (C.5b)$$

$$\begin{bmatrix} \rho_{pq}^{(7)} & \rho_{pq}^{(8)} \\ \rho_{pq}^{(9)} & \rho_{pq}^{(10)} \end{bmatrix} = \prod_n [F_{pq}^{(n)}(l_n)]^{-1} F_{pq}^{(n+1)}(l_n) \quad (C.5c)$$

The same equation (C.5) holds for $\{\bar{\rho}_{pq}^{(5)}, \bar{\rho}_{pq}^{(6)}, \dots\}$ except that $F_{pq}^{(n)}$ is replaced by $\bar{F}_{pq}^{(n)}$. Note that $\{\rho_{pq}^{(8)}, \rho_{pq}^{(10)}, \bar{\rho}_{pq}^{(8)}, \bar{\rho}_{pq}^{(10)}\}$ do not enter into the field calculation. The reason that the exponential factors are introduced into (C.5), is to facilitate the field matching at $z = \tau_c$ later.

The matrices in (C.3) and (C.5c) can be written in a more explicit form, namely,

$$[F_{pq}^{(n)}(l_n)]^{-1} F_{pq}^{(n+1)}(l_n) = \frac{1}{2} \begin{bmatrix} (1 + a_{pq}^{(n)}) e^{-jc_{pq}^{(n)}} & (1 - a_{pq}^{(n)}) e^{+jb_{pq}^{(n)}} \\ (1 - a_{pq}^{(n)}) e^{-jb_{pq}^{(n)}} & (1 + a_{pq}^{(n)}) e^{+jc_{pq}^{(n)}} \end{bmatrix} \quad (C.6a)$$

where

$$a_{pq}^{(n)} = \gamma_{pq}^{(n+1)} / \gamma_{pq}^{(n)} \quad (C.6b)$$

$$b_{pq}^{(n)} = [\gamma_{pq}^{(n+1)} + \gamma_{pq}^{(n)}] l_n \quad (C.6c)$$

$$c_{pq}^{(n)} = [\gamma_{pq}^{(n+1)} - \gamma_{pq}^{(n)}] l_n \quad (C.6d)$$

$$n = 1, 2, 3, 4, \text{ and } 6, 7, 8, 9. \quad (C.6e)$$

To calculate $[\bar{F}_{pq}^{(n)}(l_n)]^{-1} \bar{F}_{pq}^{(n+1)}(l_n)$, only the factor $a_{pq}^{(n)}$ in (C.6a) is replaced by

$$\bar{a}_{pq}^{(n)} = a_{pq}^{(n)} (\epsilon_n / \epsilon_{n+1}) \quad (C.7)$$

